

SHIMANE UNIVERSITY

Interdisciplinary Graduate School of Science and Engineering

**New development of EBSD data analysis for crystallographic
study on microstructure formation of martensitic steel**

A dissertation submitted for the degree of Doctor of Engineering

Department of Materials Creation and Circulation Technology

by

PHAM Hoang Anh

January 20, 2014

Abstract

Martensite is the most technological importance in steel, since it can exhibit both high strength and toughness. The martensite of carbon and low alloy steels often has a lath morphology which is a hierarchical combination of martensite crystals in form of thin laths. Although many aspects of crystallography of lath martensite have been clarified, particular questions on the theme of microstructure formation in lath martensite by far have not been investigated due to lacking of an effective analytical method.

Recently, electron backscatter diffraction (EBSD) technique has been demonstrating itself as the most prominent method for study on morphology and crystallography of steel. The method allows crystallographic orientation measurement for a large observation area. For crystallographic analysis on martensite, essential crystallographic information is austenite orientation and austenite/martensite orientation relationship (OR). Unfortunately, neither the austenite orientation nor the OR is readily obtained from EBSD data for martensite of low-alloyed steels. A manual method, which relies on (001) martensite pole figure with assuming a rational OR for estimation of austenite orientation, is often used by many researchers for indexing the martensite variants. Since the morphology of lath martensite is very complicated, the manual indexing method is time-consuming, even for a highly experienced researcher.

The present study aims to expand current knowledge of microstructure formation in martensitic steel with an extended view point from prior-austenite microstructure to fine morphology of lath martensite. It was focused on fundamental problems of microstructure formation such as the formation of prior-austenite microstructure, the austenite/martensite orientation relationship and the misorientation between martensite variants with varying of chemical composition or transformation condition, the effect of local strain on nucleation and growth of martensite variants. Using EBSD as main experimental tool, this study is also aimed to develop a new analytical method for effective analyses of EBSD data by involving an advanced computational approach. The following questions are investigated in each chapter:

Chapter 1 provides a review on crystallography and morphology of lath martensite. The status of EBSD application in the research topic is summarized and discussed. The view point is also focused on recent knowledge of microstructure formation in martensitic steel and the relationship between microstructure and properties.

Chapter 2 describes the materials and experimental techniques used in the present study.

Chapter 3 presents the development of a computational method for EBSD data analyses. An improvement of existing orientation fitting method was made in order to increase its efficiency and precision. The advantages of using the new method for fitting austenite orientation and OR, auto indexing of martensite variants and visual plotting martensite morphology are discussed.

Chapter 4 deals with reconstruction and characterization of prior-austenite microstructure in high carbon steels. In this chapter, the concept of “prior-austenite microstructure” is proposed. A new method for precise reconstruction of austenite microstructure from EBSD data of martensite is developed. The method is applied

successfully for reconstruction of austenite microstructure in several high carbon steels. A specific morphology of twin-related neighbor grains in prior-austenite microstructure of high carbon steels is firstly observed and characterized. The mechanism of prior-austenite microstructure formation is proposed and discussed.

In chapter 5, a statistical investigation of austenite/martensite orientation relationship (OR) with variation of steels' chemical composition is conducted. For given steel, the ORs measured for different prior-austenite grains are likely identical with the error of 0.5° . The obtained precision of present method is comparable with that of advanced TEM method. The effect of C as interstitial impurity or Ni and Mn as substitutional impurity on orientation relationship and misorientation between martensite variants is characterized and discussed. The result is important for deeper understanding the crystallography of martensite, since it reveals the relationship between martensite morphology, OR and chemical composition.

Chapter 6 presents a molecular dynamics calculation of boundary energy between martensite variants. The new models for calculation of boundary energy of twist and tilt boundaries are proposed. The boundary energies are calculated for all possible pairs of martensite variants. The role of boundary energy on microstructure formation of lath martensite is discussed.

In chapter 7, a new approach for study on the effect of local strain on nucleation and growth of fine martensite morphology is taken. The model steel with excessive amount of TiC inclusions is successfully used for this purpose. A new method for mapping local strain in austenite is proposed. The local strain map shows local raise of austenite rotation near TiC inclusions. Nucleation and growth of new morphology sub-units such as packet, block and sub-block are observed in the area surrounding micron-sized TiC particles. The effect of local strain around micron-sized TiC particles on formation of fine martensite morphology is characterized and discussed.

Finally, chapter 8 gives concluding remarks of the present study.

Contents

Chapter 1

Back ground	1
1.1. Crystallography and morphology of lath martensite	1
1.2. The relationship between microstructure and properties	5
1.3. EBSD study of lath martensite	7
1.3.1. Recent status of EBSD application in the research topic	7
1.3.2. Computational approach.....	8
1.4. The nature of microstructure formation in martensitic steels.....	12
1.5. The objective of this study	14
Reference	15

Chapter 2

Materials and experimental techniques	20
2.1. Materials	20
2.2. Experimental techniques.....	24
2.2.1. Optical and scanning electron microscopy	24
2.2.2. Electron backscatter diffraction (EBSD).....	24
Reference	27

Chapter 3

Development of a computational method for EBSD data analyses	28
3.1. Introduction	28
3.2. Fitting austenite orientation and orientation relationship from martensite.....	29
3.2.1. Calculation method.....	29
3.2.2. Fitting austenite orientation and orientation relationship separately	30
3.2.3. Using the characteristics of $(001)_\alpha$ pole figure.....	31
3.2.4. Simplifying the calculation of misorientation between two close orientations	32
3.2.5. Using two criteria for fitting.....	33
3.3. Evaluation of the new fitting program.....	33
3.3.1. Experimental.....	33
3.3.2. Coarse fitting and fine fitting	34
3.3.3. Effect of scanning step on fitting results	35

3.3.4. Fitting for different parts of one austenite grain and for different austenite grains.....	36
3.4. Automatic indexing of martensite variants and visual plotting of morphological features.....	38
3.4.1. Automatic indexing of martensite variants.....	38
3.4.2. Visual plotting of morphological features	39
3.4.3. Misorientation map.....	39
3.4.4. Example.....	40
3.5. Conclusion.....	42
Reference.....	42

Chapter 4

The nature of prior-austenite microstructure.....	45
4.1. Introduction	45
4.2. Experimental.....	45
4.3. Reconstruction method	46
4.3.1. Main steps of austenite reconstruction method	46
4.3.2. Main features of the reconstruction method	49
4.4. Reconstruction result and discussion.....	52
4.4.1. Prior-austenite microstructure in high-carbon steels	52
4.4.2. Prior-austenite microstructure in Japanese sword	60
4.5. Conclusion.....	65
Reference.....	66

Chapter 5

The orientation relationship between austenite and lath martensite.....	69
5.1. Introduction	69
5.2. Experimental.....	70
5.2.1. Calculation of orientation relationship	70
5.2.2. Calculation of misorientation between martensite variants.....	71
5.3. Result and discussion	74
5.3.1. Effect of carbon	74
5.3.2. Effect of other alloying elements.....	81
5.4. Conclusions	86
References	87

Chapter 6

Molecular dynamics calculation of boundary energies in lath martensite	88
6.1. Introduction	88
6.2. Calculation method.....	89
6.2.1. Model construction	89
6.2.2. Calculation of boundary energy	92
6.3. Result and discussion	94
6.4. Conclusion.....	97
Reference	97

Chapter 7

Effect of TiC inclusions on fine morphology of lath martensite	98
7.1. Introduction	98
7.2. Experimental.....	99
7.3. Result and discussion	101
7.4. Conclusion.....	105
Reference	106

Chapter 8

Conclusion	108
Acknowledgment	112

Chapter 1

Back ground

1.1. Crystallography and morphology of lath martensite

In ferrous alloys, the martensitic transformation occurs during quenching of austenite with the cooling rate exceeding a critical value. Phenomenological theory describes the lattice strain needed to transform face-centered cubic austenite (fcc γ) to body-centered cubic martensite (bcc α') as a combination of Bain strain \mathbf{B} with a rigid body rotation \mathbf{R} [1-12]. The Bain strain was first proposed by Bain in 1924 [14], which is given in matrix form as below:

$$\mathbf{B} = \begin{pmatrix} \varepsilon_0 & 0 & 0 \\ 0 & \varepsilon_0 & 0 \\ 0 & 0 & \varepsilon'_0 \end{pmatrix}$$

$$\varepsilon_0 = \frac{\sqrt{2}a_{\alpha'} - a_{\gamma}}{a_{\gamma}}, \quad \varepsilon'_0 = \frac{a_{\alpha'} - a_{\gamma}}{a_{\gamma}}$$

where $a_{\alpha'}$ and a_{γ} are the lattice parameters of martensite and austenite respectively.

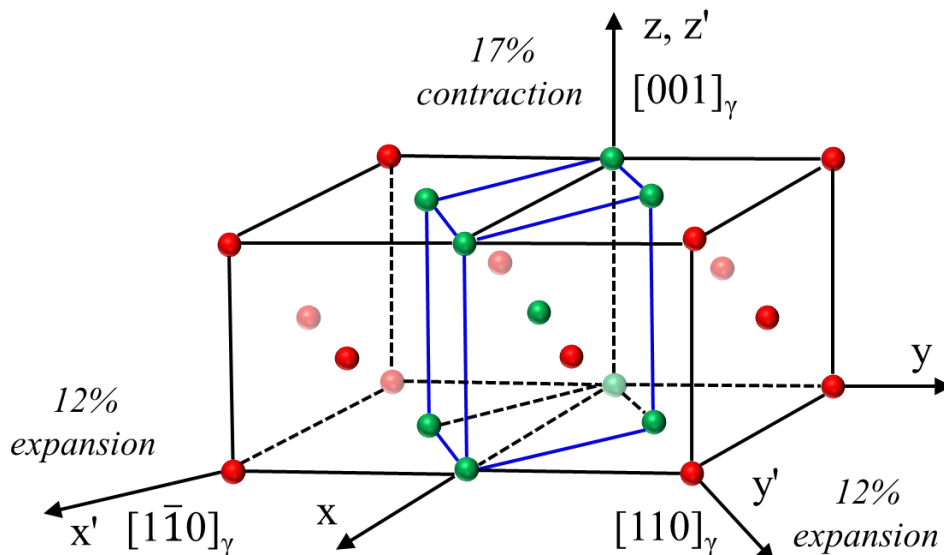


Figure 1.1. Bain correspondence showing a body-centered tetragonal (bct) unit cell of austenite received from two adjacent face-centered cubic (fcc) unit cells by coloring some of the lattice points in green. The tetragonal distortions along x', y', z' axes are expression of Bain strain required in order to receive a bcc martensite unit cell from that bct austenite unit cell.

This strain causes a compression of about 17% along the $[001]_{\gamma}$ corresponding to the z-axis of the martensite cell, and a uniform expansion of about 12% in the $(001)_{\gamma}$ plane. Since there are three choices of $[001]_{\gamma}$ compression axis, the number of Bain variants of martensite corresponding to one austenite orientation is only three (Fig.1.1). As shown in Fig.1.1 the Bain strain also requires a strict γ/α' orientation relationship: $[001]_{\gamma} // [001]_{\alpha'}$, $[1\bar{1}0]_{\gamma} // [100]_{\alpha'}$, $[110]_{\gamma} // [010]_{\alpha'}$, which has not been observed experimentally for ferrous alloys.

The phenomenological theory solved this problem by combining the Bain strain with an appropriate rigid-body rotation to fit the orientation relationship [2,5]. Furthermore, two independent invariant lattice shears were introduced to predict the habit plane and total shape strain magnitude [2,4,6]. Although the Bain correspondence solely cannot describe full characteristics of martensitic transformation in steels, it is well used in phenomenological theory to express the lattice distortion from fcc to bcc because of its simple form with a clear geometrical representation [2-15].

Various morphologies of martensite are observed in ferrous alloys depending on their chemical composition. In present terminology, they are called as lath, butterfly, lenticular and thin plate martensites [16-18]. Lath martensite is the most technologically important microstructure in heat treatable steels, since it can exhibit both high strength and toughness [11,21,67-73]. Lath martensite serves as the basic microstructure in most of advanced steels, such as cryogenic nickel steels, heat resistant chromium steels, hydrogen resistant steels, maraging steels and ultra-high strength steels, etc. [11,67-73]. Because of its technological importance, lath martensite has been intensively studied over a half of century. The researchers do not only focus their interest on crystallography and morphology of lath martensite, but they also concern the theoretical aspects of its transformation [1-12]. The relationship between microstructure and materials properties is also of the greatest interest [67-76].

The lath form of martensite is typically reported for low-carbon ($<0.5\text{mass}\%$) and low alloyed steels [11,20-26]. However, recently some researchers have reported the evidence of dominant lath martensite microstructure in medium and high carbon steels with extension for carbon content up to approximately 0.9 mass% [107-109]. Lath martensite is distinguished from other martensites by its highly dislocated internal structure and the absence of retained austenite [11,13,20,32]. The laths are long and thin plate with 0.2-0.5 μm width. Under optical microscope, the single lath is unresolvable and the microstructure appears as coarse massive phase constituent without observable retained austenite. For this reason, it had been called as “massive martensite” in the earlier crystallographic studies [16-17].

In 70's and 80's of the past century, transmission electron microscopy (TEM) was extensively used for studied of lath martensite. Under TEM observation, the sub-structure and crystallography of martensite lath was well characterized [4,6,16-18]. It had been pointed out that the lath of martensite grows in the long direction which is nearly parallel to $[111]_{\gamma}$ and the $[557]_{\gamma}$ habit plane between martensite lath and austenite is widely accepted [6,11-13,16-20]. The internal dislocation structure within a lath was described as dense dislocation tangles with $a/2[11\bar{1}]_{\alpha'}$ screw dislocations dominant [6,13,32]. The dislocation density is reported for carbon steels as around $0.5\text{-}2.2 \times 10^5 \text{ m}^{-2}$ [32]. The internal twin structure of lath martensite in high carbon steel or high nickel steels was also reported [13,18,92]. However, the adjacent martensite laths have tendency to align themselves parallel to one long direction to form a coarser microstructural unit.

There was a discrepancy between the reported results on the morphology or the combination of martensite laths. Some researchers reported about twin-related neighbor

laths [18,92], while others claimed about the low-angle misorientation between the adjacent laths [16-17]. The limitation of TEM methods for wide area characterization of microstructure is the main reason for this discrepancy in the results of these studies. In 90's, the researchers started employing electron backscatter diffraction (EBSD) technique for study of lath martensite [19-30,35-60]. This method is also called orientation imaging microscopy, which allowed scanning acquisition of local orientation in a scanning electron microscope (SEM) [33-35]. EBSD provides a power analytical tool for crystallographic and morphological study of lath martensite. The details of lath martensite morphology in the scale of prior-austenite grain have been significantly clarified through recent works that used EBSD technique [19-30].

At present, the interpretation of lath martensite morphology by Morito et al. [20-31] and their classification of martensite variants are widely accepted. According to their interpretation, lath martensite morphology is a hierarchical combination of martensite crystals in form of thin laths. All of martensite laths (α') keep a specific orientation relationship (OR) with prior austenite (γ), which is recognized as near Kurdjumov-Sachs (K-S) type [20]. The original K-S orientation relationship which is so far widely used for lath martensite, is expressed as $(111)_\gamma // (011)_{\alpha'}$ and $[\bar{1}01]_\gamma // [\bar{1}\bar{1}\bar{1}]_{\alpha'}$ [77]. Because of 24 symmetric expressions of an orientation in cubic system, one austenite orientation can transform into 24 different martensite orientations which are called 24 martensite variants of the orientation relationship. For K-S orientation relationship the 24 variants of martensite are notated as V1 to V24 with detail of orientation relationship given in Table 1.1 [20]. The standard projection of $(001)_{\alpha'}$ martensite is represented in Fig.1.2.

Table 1.1. Notation of 24 variants of martensite in K-S orientation relationship with austenite [20].

Variant No.	Plane parallel	Direction parallel [γ] // [α']	Variant No.	Plane parallel	Direction parallel [γ] // [α']
V1	$(111)_\gamma // (011)_{\alpha'}$	$[\bar{1}01] // [\bar{1}\bar{1}\bar{1}]$	V13	$(\bar{1}\bar{1}\bar{1})_\gamma // (011)_{\alpha'}$	$[0\bar{1}\bar{1}] // [\bar{1}\bar{1}\bar{1}]$
V2		$[\bar{1}01] // [\bar{1}1\bar{1}]$	V14		$[0\bar{1}\bar{1}] // [\bar{1}1\bar{1}]$
V3		$[01\bar{1}] // [\bar{1}\bar{1}\bar{1}]$	V15		$[\bar{1}0\bar{1}] // [\bar{1}\bar{1}\bar{1}]$
V4		$[01\bar{1}] // [\bar{1}1\bar{1}]$	V16		$[\bar{1}0\bar{1}] // [\bar{1}1\bar{1}]$
V5		$[1\bar{1}0] // [\bar{1}\bar{1}\bar{1}]$	V17		$[110] // [\bar{1}\bar{1}\bar{1}]$
V6		$[1\bar{1}0] // [\bar{1}1\bar{1}]$	V18		$[110] // [\bar{1}1\bar{1}]$
V7	$(1\bar{1}\bar{1})_\gamma // (011)_{\alpha'}$	$[10\bar{1}] // [\bar{1}\bar{1}\bar{1}]$	V19	$(11\bar{1})_\gamma // (011)_{\alpha'}$	$[\bar{1}\bar{1}0] // [\bar{1}\bar{1}\bar{1}]$
V8		$[10\bar{1}] // [\bar{1}1\bar{1}]$	V20		$[\bar{1}\bar{1}0] // [\bar{1}1\bar{1}]$
V9		$[\bar{1}\bar{1}0] // [\bar{1}\bar{1}\bar{1}]$	V21		$[0\bar{1}\bar{1}] // [\bar{1}\bar{1}\bar{1}]$
V10		$[\bar{1}\bar{1}0] // [\bar{1}1\bar{1}]$	V22		$[0\bar{1}\bar{1}] // [\bar{1}1\bar{1}]$
V11		$[011] // [\bar{1}\bar{1}\bar{1}]$	V23		$[101] // [\bar{1}\bar{1}\bar{1}]$
V12		$[011] // [\bar{1}1\bar{1}]$	V24		$[101] // [\bar{1}1\bar{1}]$

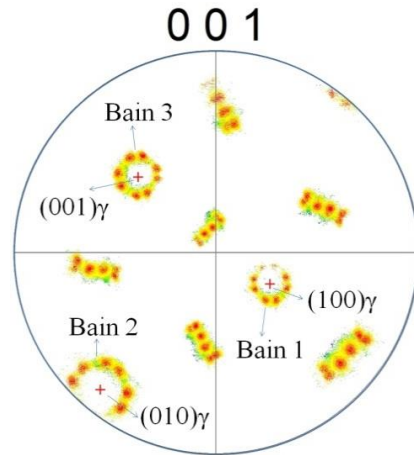


Figure 1.2. A typical (001) pole figure of lath martensite variants inherited from one prior-austenite orientation (The martensite orientations are colored by their misorientation from exact orientation relationship with austenite).

In this pole figure the 24 martensite variants within one prior austenite grain shows a ring-like distribution of $(001)_{\alpha'}$ martensite orientations around each pole of $(001)_{\gamma}$, which is referred as a Bain group. In another word, the 24 martensite variants are divided into 3 groups of 8 variants which have identical value of misorientation angle with a Bain variant. This feature of (001) martensite pole figure can be understood from the phenomenological theory prediction of lattice distortion via Bain strain and rigid-body rotation. The Bain strain produces 3 variants corresponding to three choices of $(001)_{\gamma}$ compression axis, while the rigid-body rotation introduces more flexibility to orientation relationship and hence for each Bain variant the 8 appropriate martensite variants appear as ring-like features around each of $(001)_{\gamma}$ pole. Within a Bain group, the 8 martensite variants have an equal misorientation from the corresponding Bain variant which is smaller than 12° for all reported orientation relationships. From the (001) pole figure, it is clearly that the misorientation between $(001)_{\alpha'}$ planes of any two martensite variants in different Bain groups is larger than 45° . That is the $(001)_{\alpha'}$ of martensite variants in various Bain groups are separated by high-angle misorientation. Therefore, the Bain groups are often used in discussions on the relationship between microstructure and properties of martensitic steels [19,21-23].

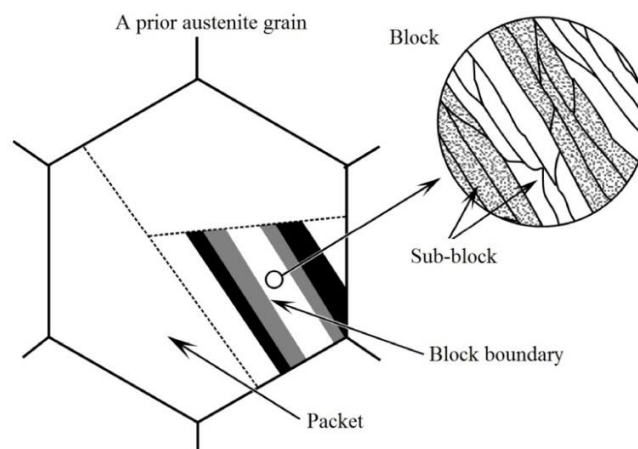


Figure 1.3. Schematic illustration of lath martensite in low carbon steel [20].

In morphological study of lath martensite, the observed combinations of variants in lath martensite were named as sub-block, block and packet (Fig.1.3). Sub-block is a group of single variant laths with small alternatively changing misorientation from 1 to 5° between each other [20]. In low-carbon or low-alloyed steels the block contains two kinds of sub-blocks, which are specific pairs of variants such as V1-V4, V2-V5 and V3-V6 [20-24], with small-angle boundary. For high-carbon and many alloy steels the block is single variant with a size smaller than that of regular block in low-carbon steels. The packet is a group of 6 variants which share the same parallel close-packed plane relationship with austenite (Table 1.1., Fig.1.4).

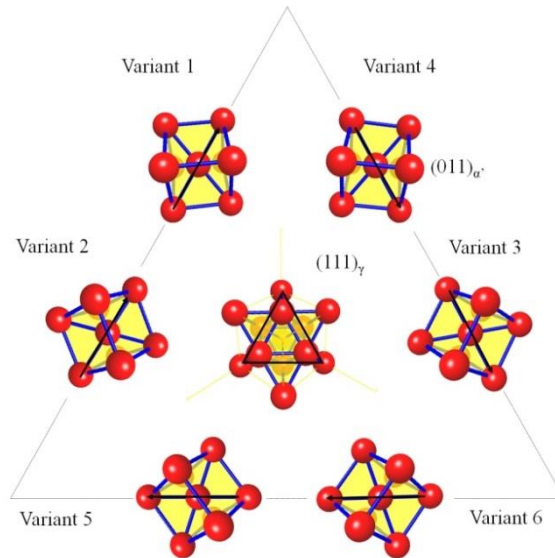


Figure 1.4. Illustration of six K-S variants sharing the same parallel close-packed plane relationship with austenite.

1.2. The relationship between microstructure and properties

High strength and toughness of lath martensite can be explained by its fine microstructure. The fine laths and their combination result a fine-grained material. The relationship between grain size and mechanical properties of steel can be expressed in form of Hall-Petch equation [66,113]. The Hall-Petch equation is explained by grain-boundary strengthening mechanism, where the grain boundaries act as barrier for further dislocation slip. The disorder of grain boundary and high misorientation between slip planes in adjacent grains impeded dislocation movement across grain boundary and hence increase the yield strength [113]. Since the block boundary in lath martensite is essentially high angle, it seems logical to think that the block size of lath martensite is the effective grain size for Hall-Petch expression of yield strength. However, there is by far a large discrepancy between the results reported by different researcher, who study this issue [19-23,67-76].

Morris and his coworkers [19,21] have studied the relationship between microstructure of lath martensite and its mechanical properties. They proposed a semi-quantitative way to define the effective grain sizes for different mechanical properties of martensitic steels. According to their reported results, the effective grain for transgranular cleavage and plastic deformation are not necessary the same. Refinement of the block size leads to improvement of resistant to cleavage fracture but it is ineffective in increasing strength [19,21]. The crystallographic coherent between martensite and austenite which leads to a specific misorientation between adjacent

martensite variants, was used to explained this tendency. According to their interpretation, the boundaries between block of different Bain groups have large misorientation between $\{100\}_{\alpha'}$ cleavage planes, while they may have small misorientation between $\{110\}_{\alpha'}$ slip planes [19]. These boundaries are effective for prevention of cleavage on $(001)_{\alpha'}$ plane, and the group of martensite variants which belongs to the same Bain group can be used as effective grain size for cleavage resistance. The size of this Bain group is comparable with the block size but not essentially the same, since there are 12 types of blocks versus 3 Bain groups with one prior-austenite grain. Furthermore, Morris et al. deduced from the $(011)_{\alpha'}$ pole figure that 80% of block boundaries in lath martensite has small misorientation between $\{110\}_{\alpha'}$ slip planes [19]. It means that most of block boundaries is transparent to dislocation gliding on $\{011\}_{\alpha'}$ slip plane. Hence, refinement of block size should not affect significantly yield strength of lath martensite [19,21].

However, Morito studying on the effect of block size on strength of lath martensite has shown that the yield strength of lath martensite is proportional to the inversion of block size following well with the Hall-Petch relationship [23,27]. Shibata studying on the effect of block boundary on behavior of lath martensite during a micro-bending test reported that the block boundary significantly restricts the motion of dislocations. He concluded that the block boundary is the most effective grain boundary for strength in lath martensite [106]. Morris explained the disagreement between his results with that of Morito and Shibata by referring to a work by Ohmura et al. [90,112], where the presence of thin film carbide at the boundary of low temperature tempered lath martensite in carbon steel was observed by TEM. In his explanation, crystallographically the block boundary is ineffective to prevent slip on $\{011\}_{\alpha'}$ plane, but the presence of thin film carbide makes this boundary becomes obstacle for dislocation movement [21]. However, in Ohmura's work, the thin film carbide is only observed in the sample of high carbon steel after 5.4ks tempering at 573K temperature [90]. The authors did not clarify the type of boundary where the formation of thin film carbide could take place, while Morito carried his study for freshly as-quenched martensite in Fe-0.2mass%C, in which the precipitation of thin film carbide has not been observed. Moreover, the sample used in Shibata study is Fe-23mass%Ni with a litter amount of C (<0.01 mass%), in which the thin film of carbide at the block boundary hardly exists.

The study of Morito also revealed that the packet size is controlled mainly by the prior austenite grain size, while additional of Mn has no effect on the mean value of packet size. The block size is control by both prior austenite grain size and additional of alloying elements. On the other side, many studies [22-23,105] have confirmed that the width of martensite lath is not affected by alloying elements or variation of prior austenite grain size. Although, the role of block boundaries on yield strengthening of lath martensite is not clear, since discrepancy of reported results does exist, the block is very important element in microstructure of lath martensite, which size corresponds to the transgranular fracture resistance and the yield strength of lath martensite.

Understanding the crystallography and morphology of lath martensite, many aspects of this specific microstructure can be explained. Effective heat treatment or thermo-mechanical treatment routs can be planned in order to control the block size for better performance of martensitic steels. The block size can be refine directly by refining the prior-austenite grain size for all steels [22-23,55,111], or indirectly by cyclic heat treatment of some high or medium alloyed steels in order to produce microstructure of interlocked thin blocks from different Bain group [30,74].

1.3. EBSD study of martensitic steel

Recently, electron backscatter diffraction (EBSD) technique has been demonstrating itself as the most prominent method for study on morphology and crystallography of steel [19-65]. The method provides quantitative microstructural information of crystalline materials for a large observation area up to several millimeters square [50]. The local grain orientation, grain size and grain boundary characteristics, texture and phase identity are available for analyses. With nominal angular resolution limit of 0.5° and spatial resolution up to 5 nm [58], EBSD is a promising technique to fill the gap between optical microscopy and TEM for multi-scale characterization of complex microstructure [58]. The application of EBSD for microstructure characterization has increased sharply from the past two decades due to the wide availability of SEM, the ease of experimental procedure and the improvement of data acquisition speed [39,58, 65].

1.3.1. Recent status of EBSD application in the research topic

From the beginning of 2000 years, EBSD have been widely applied for martensitic steel as an alternative of TEM in study of crystallography and morphology at scale of prior austenite grain [19-27, 39-65]. Although EBSD is unable to resolve a single lath of martensite, the group of laths can be revealed and characterized as a single unit with small variation of local orientation, which is termed as sub-block [20]. With help of EBSD, many characteristics of lath martensite microstructure such as subdivision of morphology, distribution of martensite variants, variant selection, etc. were clarified in details [20].

The morphology and crystallography of lath martensite in carbon steels and low alloyed steels have been clearly classified in study of Morito et al [20,24]. According to their interpretation of lath martensite morphology, one austenite grain is divided into many packets which are combination of very thin martensite lath of as much as possible 6 martensite variants sharing the same close-packed plane relationship with austenite. For example in Table1, the six variants V1-V6, which share the same parallel plane relationship with austenite $(111)_\gamma // (011)_{\alpha'}$, can appear within one packet. The adjacent laths are grouped together with alternative misorientation across lath boundary to form a coarser sub-volume unit, which is called as sub-block. The sub-block often has width in order of one micrometer, which is well resolved by EBSD method.

The sub-block can be accepted as the smallest crystallographically independent sub-volume of lath martensite, which can be revealed in normal EBSD mode. However, it is not always a morphologically independent unit. For low carbon and low alloyed steels, the two sub-blocks with small misorientation about 7° along $[011]_{\alpha'}$ are grouped together to form a block with clearly high angle boundary [20,24].

In an EBSD orientation map the block of this type is a mosaic pattern of two alternatively interleaved sub-blocks (Fig.1.5). The boundary between blocks is clearly observable with a high angle misorientation, while the sub-block boundary is often discontinuous with low-angle misorientation (Fig.1.5). On the other hand, the blocks of high carbon or high alloyed steels are usually single variant. In first case, the packet contains 3 types of interleaved blocks which belong to 3 different Bain variants. In latter case, the packet contains up to 6 types of single variant blocks with mainly high angle boundaries. For single block morphology, the low angle misorientation $7^\circ/[011]_{\alpha'}$ is rarely observed, instead a near twin misorientation $70.5^\circ/[011]_{\alpha'}$ between the blocks dominates [13,19].

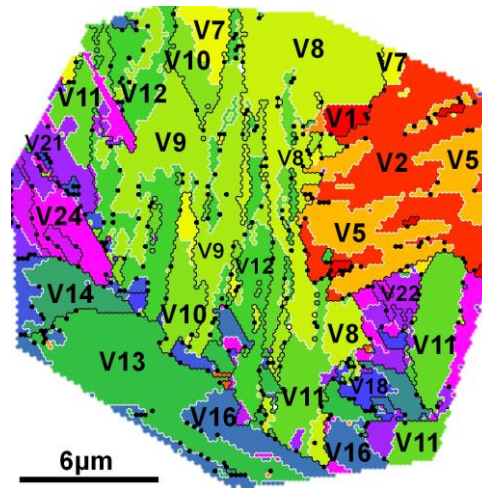


Figure 1.5. *Sub-block map showing 24 variants of martensite inherited from one prior-austenite grain (the black and white lines showing boundaries with high-angle $\geq 15^\circ$ and low-angle $< 15^\circ$ respectively).*

It is also clear that the transformation of other form of martensite and bainite have the same cooperative nature as of lath martensite, e.g. a certain orientation relationship is held between austenite and martensite or bainite. The treatment proposed by Morito for lath martensite is also applied for microstructure characterization of bainite and other forms of martensite [21,82,93,95]. The EBSD technique is actively employed for crystallographic studies on such materials. The variant selection of martensite is studied by Morito [88], and Miyamoto et al.[94,96]. The similar problem for bainite is described by Furuhashi et al. [93,95]. The effect of thermal mechanical processing on morphology of lath martensite was studied in the works of Morris [24,74] and Miyamoto et al. [96]. The relationship between martensite morphology and cleave fracture was investigated by Morris et al. [19,28,30], while the effect of austenite grain size (block size) on tensile strength was studied in the works of Morito et al. [22-23]. The effect of alloying elements on martensite morphology of various steels was also investigated [20,24-26,94,96].

1.3.2. Computational approach

In general, EBSD provides only information of martensite orientations, while for crystallographic analysis on martensite, other essential information is austenite orientation and austenite/martensite OR. Unfortunately, neither the austenite orientation nor the OR is readily obtained from EBSD data for martensite of low-alloyed steels. A manual method, which relies on comparing (001) martensite pole figure with standard (001) pole figure of Kurdjumov-Sachs (K-S) [77] or Nishiyama-Wasserman (N-W) [78-79] orientation relationships, is often used by many researchers for indexing the martensite variants [20-26]. The method is rather a qualitative method which is useful for determination of martensite variants and other features of morphology such as packet, block, and sub-block types. The results are used for description of martensite morphology or pairing of adjacent martensite variants within a prior austenite grain [20-26]. Several quantitative measurements are available, among them the measurement of packet size, block and sub-block widths are often performed [20,24]. Since the morphology of lath martensite described above is very complicated, the manual indexing method is time-consuming, even for a highly experienced researcher.

In order to improve the efficiency of data analysis for EBSD technique, computation approach has been recently involved by some authors for calculation of OR

and/or austenite orientation [82,97]. The computation approach is very promising since the transformation of martensite is cooperative with a stable orientation relationship held between parent and product phases for a wide range of steel compositions. Some authors [82] are interested in precise calculation of OR and austenite orientation from one austenite grain, while the others deal with reconstruction of austenite orientations or austenite grain maps for a number of grains [97-102]. In the first consideration, the precise OR and austenite orientation are important for various crystallographic and morphological studies of martensite microstructure, which are mentioned above. In the later consideration, the austenite orientations or grains shape are of interest for study on the effect of thermo-mechanical processing on prior austenite microstructure.

a) Indexing martensite variants

Although the martensite variants can be manually indexed, the process itself is time consuming with some essential limitations. Firstly a model of OR should be used, which are often chosen alternatively between K-S or N-W types. Those rational ORs have not been confirmed either in experimental investigation [80-85] or in theoretical calculation [6,9,11-13]. However, this approximation is acceptable for qualitative indexing of martensite variants, since the deviation between the real OR and those rational ORs is within a few degrees. Secondly, the manual method is not suitable for indexing simultaneously a large number of martensite variants, which can be up to 24 within one prior austenite grain. The main reason is the difficulty for choosing manually different colors to represent all martensite variants without confusing. In manual indexing method, the martensite variants or blocks are often represented for an individual packet, which contains up to six martensite variants or three types of blocks. Lastly, many quantitative analyses are not available without austenite orientation and OR.

Miyamoto et al. [82] were among the first researchers, who reported about the method for calculation of average OR from EBSD data without information of retained austenite. His calculation is based on numerical optimization of average deviation between experimental and calculated martensite variants. The obtained result was interested, since one can calculate both the average OR and austenite orientation from EBSD data without the need of retained austenite. Later, his method has been used for quantitative analyses of martensite and bainite on variant distribution, variant selection and also reconstruction of prior austenite orientation maps [94-96,100-101]. Although Miyamoto claimed his method as an “accurate measurement” of OR, this term might be improperly used. The “accuracy” of a measurement means the degree of closeness of measurement of actual quantity to its “true” value [103], whereas the “true” value of OR has not been confirmed in his study. On the other hand, the “precision” expresses the degree to which repeated measurements under unchanged conditions show the same results [103]. It is likely that the proper term “precise measurement” should be used instead of “accurate measurement” to refer to his method.

Although Miyamoto [82] did not describe in details his calculation method, the disadvantages of his reported method are several. Firstly, in his description both the OR and the austenite orientation are concerned as variables for numerical fitting. This approach would cause much of calculation time as discussed later in chapter 3. Secondly, the method for calculation of deviation between experimental and fitted martensite variants was described for general case, which did not count the specific features of (001) martensite pole figure for saving calculation work. Thirdly, the single criterion for minimization of average deviation sometimes can cause significant error in calculation of austenite orientation, if the data are not inherited from a single austenite

orientation. It is well known that the austenite grain usually contains twins, whose inherited martensite orientations are often erroneously selected from EBSD data as those inherited from a single austenite orientation for analysis. The single criterion of minimum average misorientation is incapable for filtering the data which contain more than one austenite orientation in such case. Lastly, the calculated OR and martensite variants were not used for automatic indexing of martensite or other graphic representations of martensite morphology, which are similar to those reported by manual method. The solutions for improvement of numerical approach to automatic indexing of martensite variants will be discussed in details in the chapter 3 of the present study.

b) Prior austenite reconstruction

Since EBSD allows orientation measurement in a large scale, the information for a number of prior austenite grains can be collected. Thanks to this benefit, the crystallographic study of lath martensite is not limited to a prior austenite grain, but its scale can be extended to coverage a big number of prior austenite grains. In order to study the effect of thermo-mechanical processing on prior austenite microstructure, several authors have tried different approaches to reconstruct the prior-austenite grain orientation and/or grain shape from EBSD data of martensite or bainite [97-102].

The first approach can be named as “neighbor to neighbor reconstruction”, which defines austenite orientation or austenite grain by comparing orientations between neighbor martensite grains or “domain” [97-99]. The EBSD data was pre-processed by using “grain detection” feature in commercial EBSD analysis programs. The domain contains adjacent pixels of EBSD data with neighbor to neighbor misorientation smaller than a given tolerance angle, usually ranges from 3-5°. The orientation of one domain is represented as the averaged orientation of all the pixels within this domain.

Cayron et al. [98] had done a first trial to reconstruct austenite grain map from martensite by using a groupoid structural analysis with supposing of a rational orientation relationship either K-S or N-W. A groupoid structure, which describes the transformation operators between 24 martensite variants, was built for a chosen OR (K-S or N-W). The transformation operators between adjacent martensite domains were compared with those values obtained from the chosen OR within a small tolerance angle to determine whether they belongs to the same prior austenite grain. The process is iterated until all of ferrite domains are inspected. This method is capable of reconstruction austenite grain map without the need of knowing austenite grain orientation. The method proposed by Crayon in some extents is capable for reconstruction of the austenite grain map from martensite domain orientations. However, its application is limited because of some reasons. Firstly, the OR used should be strictly rational (either K-S or N-W types), while the observed ORs by present author and other researchers are irrational [80-85]. Secondly, the austenite orientations are remained unknown, which implies that the obtained information needed for further analysis of crystallography or morphology is rather limited.

Using a similar neighbor to neighbor approach, Blaineau and Germain et al. [98,102] had extends the method proposed by Humbert et al. [97] which treats the bcc-hcp transformation, to the fcc-bcc transformation for reconstruction of austenite orientation. In their method, the prior austenite orientation was reversely calculated from martensite domain orientation, while the OR was fixed. A small tolerance angle was used for finding the most potential austenite orientation which is related to neighboring martensite domains. A larger tolerance angle was used for expanding the austenite orientation to adjacent martensite domains if their orientations are related to

the parent orientation by the given OR. There was the case, that a martensite domain was related to at least two austenite orientations. That domain was called as “ambiguous domain” [102]. The reason of “ambiguous domain” was that two austenite orientations have a certain possibility to have a common martensite variant [102]. In extreme case, for K-S OR, two twin-related austenite orientations can have 6 common martensite variants. The ambiguous location in austenite orientation map should be corrected manually using additional information in martensite microstructure [102].

The method proposed by Blaineau and Germain has advantage on that of Cayron [98], since it can successfully reconstructed austenite orientation maps. However, in their method it is expected that the precision of reconstructed austenite orientation should not so high, since the austenite orientation was directly calculated from averaged orientation of only one martensite domain. The method also reduces the spatial resolution of original EBSD data by using coarsened data of martensite domains.

Miyamoto et al. extended their numerical fitting method as above mentioned [82] to reconstruction of prior austenite orientation map from martensite/bainite for both ausformed and non-ausformed specimens [100-101]. Their method includes in subdivision of EBSD data using small square grid and fitting austenite orientation from martensite orientations within each square. The method was capable to reconstruct local austenite orientation with some approximation comparable with the grid size. Since several martensite variants in each square were used for calculation of austenite orientation, this method should has precision better than that of the neighbor to neighbor methods. However, this method is incapable for precise reconstruction of austenite grain boundary, since for a square that includes prior austenite grain boundary or twin boundary, the martensite variants belongs to more than one austenite orientation are included. Fitting austenite orientation from such data results a rough approximation with only one austenite orientation deduced.

Although the method can be fully automated, it is clearly that, the precision of reconstructed austenite orientation should strongly depend on the prior austenite grain size and the morphology of martensite. The method is also time consuming compared with the neighbor to neighbor methods, since it requires fitting of austenite orientation from all of scanning pixels included in each square. The calculation time might be in great concern while applying this method to a large observation area. In order to reconstruct local austenite orientation map, the main problem with whom this method should deal is that, the size of square grid should be as small as possible in order to increase spatial resolution of reconstructed austenite orientation, whereas it should be as large as possible to ensure high precision of the solution. Hence, the grid size should be carefully chosen with regard to the prior austenite grain size and martensite microstructure. In any case, the presence of martensite orientations related to another austenite orientation at grain boundary, will reduce the precision of the calculation. Because of its specifications, the method proposed by Miyamoto et al. worked in some extend, on reconstruction of austenite orientation map for bainite or martensite of medium and high carbon steels with fine block size which ensures the use of small square grid [96,100-101]. However, it might be insufficient for low carbon steel martensite, which exhibits coarser block morphology. Application of the method might be also limited to the materials with relatively large prior austenite grain size.

Since there has not been an ideal method for reconstruction of austenite orientation maps from martensite, a method for precise reconstruction of prior austenite microstructure will be discussed in the chapters 3 and 4. It should be mentioned that the term “prior-austenite microstructure” has not been proposed previously by any author. This term was firstly used by present author to indicate the reconstructed microstructure

of austenite from a selected area of product phase, which comprises averaged austenite grain orientations, grain shape and grain boundary characteristics. The details of reconstruction method and analyses on prior austenite microstructure of several high carbon steels will be included in chapter 4.

1.4. The nature of microstructure formation in martensitic steels

By far the phenomenological theory has successfully predicted many features of crystallography and morphology of lath martensite [1-12]. It is likely that the block morphology is the most important sub-structural unit of lath martensite microstructure, since it is concerned as effective grain for strength and toughness [19-25,28-30]. Several authors have tried to explain the observed structure of block in low carbon steel, which was described in 1.1, by employing different models of phenomenological theory for martensitic transformation [19-24,29].

Morris et al. [19,21] employed the conventional theory developed by Khatchaturyan [5] to explain the interleaved structure of block. Their calculation of transformation strain shown, that the two specific martensite variants V1-V4 share the same lattice strain, but the rotation components are mutually canceled out [19]. The equal mixture of these variants in blocks has a net strain closed to a simple tetragonal strain. If the blocks of three Bain variants present in equal fractions in a packet, the net transformation strain is almost simple dilatation, which is most easily accommodated [19].

Iwashita et al. modified the Khatchaturyan's model by adding two independent plastic deformations corresponding to the two slip system $[101](\bar{1}01)_{\alpha'}$ and $[\bar{1}01](101)_{\alpha'}$ [29]. This model is a particular case of double shear version proposed by Kelly [6], who investigated all the rational lattice invariant shear systems that are established slip (or twinning) systems in either the bcc martensite or the fcc austenite. Iwashita et al. also concluded that V1 and V4 have the same lattice strain but their magnitudes of plastic deformation are different. The variation in magnitude of plastic deformation within a block leads to the interleaving of V1 and V4, though the equal fraction of those variants is optional. However, they did not do any calculation on total shape strain or strain energy for a further discussion on the benefit of such structure of the block. The models of Morris and Iwashita in some extent can describe the interleaved structure of blocks in low carbon steel, whereas they cannot explain the morphology of single variant blocks in high carbon steel.

Morito et al. explained that the difference in appearance of blocks between low and high carbon steels is due to the mechanism of strain accommodation [20]. According to his argument, in low carbon steel with high martensite start temperature (M_s), the austenite has high ability to accommodate the transformation strain from adjacent martensite by plastic deformation, since it is relatively soft due to dilution of carbon and high temperature condition. In high carbon steels, the M_s temperature is lower and austenite is harder by enrichment of solute carbon, so the transformation strain is difficult to transfer to austenite. It should be accommodated by self-accommodation mechanism by activation of all 6 blocks of small size with different shear components [20]. The calculation of shape strain for various combination of martensite variant by Morito et al. [20] using the model proposed by Kelly [6] shown that the shape strain is actually minimum when all of 6 martensite variants are equally present within a packet. However, the morphology of interleaved block in low carbon steel could not be explained through this calculation, by relying solely on total shape strain.

By introducing additional degrees of freedom though independent shears or plastic deformations, the phenomenological theory successfully predicts many aspects in crystallography of lath martensite such as the habit plane, the orientation relationship between austenite and martensite, the long direction of martensite lath and the dislocation structure. The specific interleaved structure of block was also explained for the simplified model. However, the real block morphology of lath martensite is complicated, which is varied with chemical composition and transformation conditions including transformation temperature and quenching rate [20-28]. These parameters as well as the constraint conditions in polygrain medium are not counted in phenomenological theory. Thus, many efforts are required in order to understand the nature of microstructure formation in martensitic steels.

The effects of various factors on morphology of lath martensite were investigated by many authors in order to understand the nature of its microstructure formation [22,27,55,72-76,93-96]. Most of the reported studies were focused on morphological characterization [72-76], variant pairing or variant selection under various conditions [93-96]. The effect of prior austenite grain size on martensite morphology was also investigated [22,55], but the prior austenite microstructure itself has not been studied. Recently, some studies on three dimensional (3D) morphology of lath martensite by combination of serial sectioning and EBSD have been reported [46,53,44,104]. The 3D morphology is very interesting for understanding microstructure formation in materials science. While the method for serial sectioning is in development to improve reliability and precision, an efficient method is required for microstructure characterization of massive EBSD data acquired from the section series.

Particular questions on the theme of microstructure formation in lath martensite by far have not been investigated due to lacking of an effective analytical method. Those questions includes the formation of austenite microstructure, the orientation relationship between austenite and martensite with varying of chemical composition or transformation condition, the effect of local stress on martensite nucleation, the misorientation between martensite variants and its relationship with other features of lath martensite. The questions are in scope of the current study and the details will be discussed in the following chapters.

1.5. The objective of this study

The present study aims to expand current knowledge of microstructure formation of martensitic steel with an extended view point from prior austenite microstructure to fine morphology of lath martensite. It was focused on fundamental problems of microstructure formation such as the formation of prior-austenite microstructure, the austenite/martensite orientation relationship and the misorientation between martensite variants with varying of chemical composition or transformation condition, the effect of local stress on martensite nucleation. Using EBSD as main experimental tool, this study is also aimed to develop a new analytical method for effective analyses of EBSD data by involving an advanced computational approach.

The content of this thesis is arranged as follows:

Chapter 2 describes the materials and experimental techniques used in this study. The choice of materials, design of composition and heat treatment were presented in details. The characteristics of experimental techniques and setting parameters of equipment for various experiments are described.

Chapter 3 presents the development of a computational tool for EBSD data analyses. An improvement of existing orientation fitting method was made in order to increase its efficiency and precision. The advantages of using this tool for fitting austenite orientation and OR from martensite, auto indexing of martensite variants and precise reconstruction of prior austenite microstructure were discussed.

Chapter 4 deals with the reconstruction and characterization of prior austenite microstructure in high carbon steels. Some specific features of the microstructure were characterized for the first time. The mechanism of prior austenite microstructure formation was proposed.

In chapter 5 a statistical investigation of austenite/martensite orientation relationship with variation of chemical composition and heat treatment condition was conducted. The OR is described by two small deviations between close-packed planes θ_1 and between close-packed directions θ_2 of the two phases. The effect of composition on these deviations and misorientation between martensite variants were in focus.

Chapter 6 presents a molecular dynamics calculation of boundary energy between martensite variants. The models for calculation of boundary energy of twist and tilt boundaries were proposed. The boundary energies were calculated for all possible pairs of martensite variants. The role of boundary energy on microstructure formation of lath martensite was discussed.

In chapter 7, a model steel with TiC inclusions was used for study on the effect of micron-sized titanium carbide (TiC) on fine morphology of lath martensite. The obtained result is important in order to understand the role of local stress on formation of martensite variants. A new method for mapping the local strain in prior-austenite is proposed.

Chapter 8 presents the overall conclusions of this study.

Reference

- 1) A.G Crocker, B.A Bilby: Acta Metall. **9**, No.7 (1961) 678-688.
- 2) N.D.H Ross, A.G Crocker: Acta Metall.**18**, No.4 (1970) 405-418.
- 3) J.A. Klostermann: Less-Common Metals **28**, No.1 (1972) 75-94.
- 4) C.M. Wayman:Less-Common Metals **28**, No.1 (1972) 97-105.
- 5) A. G. Khachaturyan: J. Wiley, New York (1983) pp. 574.
- 6) P.M.Kelly: Mater. Trans. **33**, No.3 (1992) 235-242.
- 7) A.L. Roytburd:J. Phys. (Fr.) **III**, No.5 (1995) 21-30.
- 8) Y. Wang, A.G. Khachaturyan: Acta Mater. **45**, No.2 (1997) 759-773.
- 9) H. K. D. H. Bhadeshia:J. Phys. (Fr.) **IV**, No.7 (1997) 367-376.
- 10) G.B Olson: Mater. Sci. Eng.A **273–275**, No.15 (1999) 11-20.
- 11) H.K.D.H. Bhadeshia, R. Honeycombe: Elsevier (2006) pp. 360.
- 12) P.M. Kelly: Mater. Sci. Eng.A **438-440** (2006) 43-47.
- 13) P. M. Kelly and J. Nutting: Proc Roy. Soc.A **259** (1960) 45-58.
- 14) E. C. Bain:Trans. AIME **70** (1924) 25-46.
- 15) J. S. Bowles, C. M. Wayman: Metall. Trans. **3**, No.5 (1972) 1113-1121.
- 16) G. Krauss, A. R. Marder: Metall. Trans.**2**, No.9 (1971) 2343-2357.
- 17) F.Schoen, J. Nilles; W. Owen: Metall. Trans.**2**, No.9 (1971) 2489-2494.
- 18) M. Umemoto, E. Yoshitake, I. Tamura: Mater. Sci.**18** (1983) 2893-2904.
- 19) J. W. Morris, Jr., C. S. Lee and Z. Guo: ISIJ Int.**43** (2003) 410-419.
- 20) S. Morito, H. Tanaka, R. Konishi, T. Furuhashi, T. Maki: Acta Mater.**51** (2003) 1789-1799.
- 21) Z. Guo, C.S. Lee, J.W. Morris Jr.: Acta Mater.**52** (2004) 5511-5518.
- 22) S. Morito, H. Saito, T. Ogawa, T. Furuhashi, T. Maki: ISIJ Int.**45** (2005) 91-94.
- 23) S. Morito, H. Yoshida, T. Maki, X. Huang: Mater. Sci. Eng.A **438–440** (2006) 237-240.
- 24) S. Morito, X. Huang, T. Furuhashi, T. Maki, N. Hansen: Acta Mater.**54** (2006) 5323-5331.
- 25) H. Kitahara, R. Ueji, N. Tsuji and Y. Minamino: Acta Mater.**54**, No.5 (2006) 1279-1288.
- 26) S. Morito, Y. Adachi, T. Ohba: Mater. Trans. 50, No.8 (2009) 1919-1923.
- 27) S. Morito, R. Igarashi, K. Kamiya, T. Ohba, T. Maki: Mater. Sci. Forum 638 - 642 (2010)1459-1463.

- 28) J.W. Morris: ISIJ Int. **51** (2011) 1569-1575.
- 29) K. Iwashita, Y. Murata, Y. Tsukada, T. Koyama: Phi. Mag. **91**, No.35 (2011) 4495-4513.
- 30) J.W. Morris Jr, C. Kinney, K. Pytlewski and Y. Adachi: Sci. Technol. Adv. Mater. **14** No.1 (2013) 208-216.
- 31) P.M. Kelly, A. Jostsons and R.G. Blake: Acta Metall. Mater. **38** (1990) 1075-1081.
- 32) S. Morito, J. Nishikawa, T. Maki: ISIJ Int. **43** (2003) 1475-1477.
- 33) J. A. Venables, C. J. Harland: Phil. Mag. **27** (1973) 1193-1200.
- 34) J. A. Venables, R. Bin-Jaya: Phil. Mag. **35**, No.5 (1977) 1317-1332.
- 35) S.I. Wright, J.W. Zhao, B.L. Adams: Text. Microstr. **13** (1991) 123-131.
- 36) J. Hjelen, R. Orsund, E. Hoel, P. Runde, T. Furu, E. Nes: Text. Microstr. **20** (1993) 29-40.
- 37) B.L. Adams, S.I. Wright, K. Kunze: Metall. Trans.A **24** (1993) 819-831.
- 38) R.A. Schwarzer: Micron **28**, No.3 (1997) 249-265
- 39) Jon Alkorta: Ultramicroscopy **131** (2013) 33-38.
- 40) A.F. Gourgues, H.M. Flower, T.C. Lindley: Mater. Sci. Tech. **16** (2000) 26-40.
- 41) D.W. Suh, J.H. Kang, K.H. Oh, H.C. Lee: Scripta Mater. **46** (2002) 375-378.
- 42) F.J Humphreys: Scripta Mater. (2004)
- 43) D. Dingley : Microsc. **213** (2004) 214-224.
- 44) H. Kitahara, R. Ueji, M. Ueda, N. Tsuji, Y. Minamino: Mater. Charac. **54** (2005) 378- 386.
- 45) A. Shibata, S. Morito, T. Furuhashi, T. Maki: Scripta Mater. **53** (2005) 597-602.
- 46) D.J. Rowenhorst, A. Gupta, C.R. Feng, G. Spanos: Scripta Mater. **55** (2006) 11-16.
- 47) T. Furuhashi, H. Kawata, S. Morito, T. Maki: Mater. Sci. Eng.A **431** (2006) 228-236.
- 48) A. F. Gourgues-Lorenzon: Int. Mater. Rev. **52**, No.2 (2007), 65-128.
- 49) M. Karlsen, J. Hjelen, Grong,, G. Rrvik, R. Chiron, U. Schubert, E. Nilsen: Mater. Sci. Tech. 24, No.1 (2007) 64-72.
- 50) Zhou, Weilie; Wang, Zhong Lin (ed.): Springer (2007) pp. 522.
- 51) B. Sonderegger, S. Mitsche, H. Cerjak: Mater. Charac. **58** (2007) 874-882.
- 52) N. Nakada, T. Tsuchiyama, S. Takaki, S. Hashizume: ISIJ Int. **47**, No.10 (2007) 1527-1532.
- 53) S. Zaefferer, S.I. Wright, D. Raabe : Metall. And Mater. Trans.A **39** (2008) 374-389.
- 54) S. Zaefferer, P. Romano, F. Friedel: Microsc. **230** (2008) 499-508.

- 55) T. Furuhashi, K. Kikumoto, H. Saito, T. Sekine, T. Ogawa, S. Morito, T. Maki: *ISIJ Int.* **48** (2008) 1038–1045.
- 56) A. F. Gourgues-Lorenzon: *Microsc.* **233**, No.3 (2009) 460–473.
- 57) V. Randle: *Mater. Sci.* **44**, No.16 (2009) 4211–4218.
- 58) A.J. Schwartz, M. Kumar, B.L. Adams, D. Field (ed.): Springer (2009) pp. 403.
- 59) V. Randle: *Mater. Charac.* **60**, No.9 (2009) 913–922.
- 60) F. Barcelo, Y. Carlan, J.L. Béchade, B. Fournier: *Phase Trans.* **82** (2009) 808–820
- 61) P. Haušild, V. Davydov, J. Dražokoupil, M. Landa, P. Pilvin: *Mater. Design*
- 62) D. R. Steinmetz, S. Zaeferrer: *Mater. Sci. Tech.* 26, No.6 (2010) 640–645.
- 63) M. Kamaya: *Ultramicroscopy* **111**, No.8 (2011) 1189–1199.
- 64) I. Lischewski, G. Gottstein: *Acta Mater.* **59**, No.4 (2011) 1530–1541.
- 65) Y. Chen, J. Hjelen, S.S. Gireesh, H.J. Roven: *Microsc.* **245**, No.2 (2012) 111–118.
- 66) N. Hansen: *Scripta Mater.* **51**, No.8 (2004) 801–806.
- 67) G. Krauss: *Mater. Sci. Eng.A* **273–275** (1999) 40–57.
- 68) G. B. Olson: *Science* **277**, No.5330 (1997) 1237–1242.
- 69) J.W. Morris, Jr., Z. Guo, C. R. Krenn and Y. H. Kim: *ISIJ Int.* **41** (2001) 599–611.
- 70) T. Ohmura, T. Hara, K. Tsuzaki: *Mater. Res.* **18**, No. 6 (2003) 1465–1470.
- 71) J.W. Morris, Jr.: *ISIJ Int.* **48**, No.8 (2008) 1063–1070.
- 72) B. Hutchinson, J. Hagström, O. Karlsson, D. Lindell, M. Tornberg, F. Lindberg, M. Thuvander: *Acta Mater.* **59** (2011) 5845–5858.
- 73) P. Shanthraj, M.A. Zikry: *Mech. of Mater.* **58** (2013) 110–122.
- 74) H. J. Kim, Y. H. Kim and J. W. Morris, Jr.: *ISIJ Int.* **38** (1998) 1277–1285.
- 75) X.F. Zhang, P. Han, H. Terasaki, M. Sato, Y. Komizo: *Mater. Sci. Tech.* **28**, No.3 (2012) 241–248.
- 76) A.J. Kaijalainen, P.P. Suikkanen, T.J. Linnell, L.P. Karjalainen, J.I. Kömi, D.A. Porter: *Alloys Comp.* **577**, Supp.1 (2013) 642–648
- 77) G.V. Kurdjumov and G. Sachs: *Z. Physik* **64** (1930) 324–326.
- 78) Z. Nishiyama: *Sci. Rep. Tohoku Univ.* **23** (1934) 637–664.
- 79) G. Wassermann: *Mitt K-W-I Eisenforsch* **17** (1935) 149–158.
- 80) A.B. Greninger, A.R. Troiano: *Metals Trans.* **185** (1949) 590–598.
- 81) W.Z. Zhang, G.C. Weatherly: *Scripta Mater.* **37**, No.10 (1997) 1569–1574.
- 82) G. Miyamoto, N. Takayama and T. Furuhashi: *Scripta Mater.* **60** (2009) 1113–1116.
- 83) V. Ocelík, I. Furár and J.Th.M. De Hosson: *Acta Mater.* **58** (2010) 6763–6772.
- 84) Y. Meng, X.F. Gu, W.Z. Zhang: *Acta Mater.* **58** (2010) 2364–2375.

- 85) C.P. Luo, J. Liu: Mater. Sci. Eng.A **438–440** (2006) 149-152.
- 86) M. Cohen: Mater. Trans. **33**, No.3 (1992) 178-183.
- 87) A. Borgenstam: Mater. Sci. Eng.A **273–275** (1999) 425–429.
- 88) S. Morito, Y. Edamatsu, K. Ichinotani, T. Ohba, T. Hayashi, Y. Adachi, T. Furuwara, G. Miyamoto and N. Takayama: Alloys Compd. **577**, Suppl. 1 (2013) 587-592.
- 89) S. Zhang, S. Morito and Y. Komizo: ISIJ Int. **52** (2012) 510-515.
- 90) T. Ohmura, T. Hara, K. Tsuzaki: Scripta Mater.**49**, No.12 (2003) 1157-1162.
- 91) R. Jones, V. Randle, G. Owen: Mater. Sci. Eng.A **496**, No.1-2 (2008) 256-261.
- 92) Y. Liu, Y. Li, Y. Tan, B. Huang: Iron and Steel Res. Int.**13**, No.3 (2006) 40-46.
- 93) T. Furuwara, H. Kawata, S. Morito, G. Miyamoto, T. Maki: Metall. Mater. Trans.A **39**, No.5 (2008) 1003-1013.
- 94) A. Stormvinter, G. Miyamoto, T. Furuwara, P. Hedström, A. Borgenstam: Acta Mater.**60**, No.20 (2012) 7265-7274.
- 95) N. Takayama, G. Miyamoto, T. Furuwara: Acta Mater.**60** (2012) 2387-2396.
- 96) T. Chiba, G. Miyamoto, T. Furuwara: ISIJ Int.**53** (2013) 915-919.
- 97) M. Humbert, N. Gey: Appl. Cryst.**35** (2002) 401-405.
- 98) C. Cayron, B. Artaud, L. Briottet: Mater Charact.**57** (2006) 386-401.
- 99) P. Blaineau, L. Germain, M. Humbert, N. Gey: Solid State Phen.**160** (2010) 203-210.
- 100) G. Miyamoto, N. Iwata, N. Takayama, T. Furuwara: Acta Mater.**58** (2010) 6393–6403.
- 101) G. Miyamoto, N. Iwata, N. Takayama, T. Furuwara: ISIJ Int.**51** (2011) 1174–1178.
- 102) L. Germain, N. Gey, R. Mercier, P. Blaineau, M. Humbert: Acta Mater.**60**, No.11 (2012) 4551-4562.
- 103) J.R. Taylor: Univ. Sci. Books (1997) pp.327.
- 104) M.A. Groeber, B.K. Haley, M.D. Uchic, D.M. Dimiduk, S. Ghosh: Mater. Charac.**57**, No.4–5 (2006) 259-273.
- 105) S. Morito, T. Ohba, T. Maki: Mater. Sci. Forum **558-559** (2007) 933-938.
- 106) A. Shibata, T. Nagoshi, M. Sone, S. Morito, Y. Higo: Mater Sci. Eng.A **527**, No.29-30 (2010) 7538-7544.
- 107) A.K. Das, T. Ohba, S. Morito, M. Yaso: Mater. Sci. Forum **654-656** (2010) 138-141.
- 108) G. Takami, T. Ohba, S. Morito, A.K. Das: Mater. Sci. Forum **654-656** (2010) 134-137.
- 109) M. Yaso, Y. Minagi, T. Takaiwa, K. Kubota, T. Kanaizumi, T. Ohba, S. Morito, T. Hayashi: Mater. Sci. Forum **738-739** (2013) 222-227.

- 110) A. Yamanaka, T. Takaki, Y. Tomita: Mat. Sci. Eng.A **491**, No.1-2 (2008) 378-384.
- 111) R. A. Grange: Metall. Trans. **2** (1971) 65-78.
- 112) T. Ohmura, A. M. Minor, E. A. Stach and J. W. Morris, Jr.: Mater. Res.**19** (2004) 3626-3632.
- 113) W.D. Callister, D.G. Rethwisch: Wiley & Sons (2012) pp. 910.

Chapter 2

Materials and experimental techniques

2.1. Materials

A wide range of martensitic steels was investigated for various experimental purposes in this study. The first group includes plain carbon steels with the carbon content varying from 0.1 to 0.8 mass%. These steels were used for study on the effect of carbon on orientation relationship and morphology of lath martensite (chapter 5). The effect of carbon on formation of prior austenite microstructure was also investigated (chapter 4). The second group contains high-carbon steels in form of short knives, which were prepared by traditional method for making Japanese sword. For this group, the effect of successive fold-forging operations of traditional sword preparing method on prior austenite microstructure and final martensite microstructure was investigated (chapter 4). The third group is a series of low-alloy steels with additions of Mn or Ni up to 3 mass%. The effect of additional alloying elements on orientation relationship and morphology of lath martensite was studied (chapter 5). The last steel with addition of Ti was designed for studying the effect of local strain on formation of martensite variant (chapter 7).

a) Carbon steels

The chemical compositions of plain carbon steels used in this study are given in the table 2.1. The unit for expression of chemical composition of all the steels in present study is mass%. The steels were named by their mean mass percent of carbon as C10, C40, C40 and C80. Initial microstructure of C10, C40 and C60 is ferrite + pearlite, with the fraction of ferrite decrease as the carbon content increases. C80 has a full pearlitic microstructure with fine cementite lamellae.

Table 2.1. *Chemical composition of plain carbon steels (mass%).*

Steel	C	Si	Mn	P	S	Fe
C10	0.09	0.01	0.01	0.001	0.002	Bal.
C40	0.38	0.006	0.01	0.001	0.004	Bal.
C60	0.61	0.03	0.01	0.003	0.005	Bal.
C80	0.78	0.03	0.03	0.005	0.005	Bal.

The steels were heat treated in order to obtain lath martensite microstructure. The heating temperature was chosen according to the Ac₃ temperature of individual steel. Samples from C60 and C80 were heated at 1073K in a tube furnace under Ar gas flow for 0.6ks followed by water quench (WQ). For C40 steel, 2mm thin specimens were heated in a salt bath at 1073K and 1123K for 0.6ks followed by iced brine quench (IBQ). Since the C10 steel is a pure low carbon steel, it was impossible to receive full lath martensite microstructure of this steel through conventional heat treatment route. For this reason, a rapid quenching treatment was applied for this steel in order to receive full

lath martensite microstructure. The heat treatment of C10 steel, which was also applied for the series of low-alloy steels, is described in the later section denoted those steels.

b) High-carbon steels for preparing Japanese sword

To study the effect of traditional method for preparing Japanese sword on the formation of prior austenite and final martensite microstructures, two high-carbon steels prepared in form of two short knives and a modern Japanese sword with unknown composition were used. The effect of processing on crystallography of martensite and OR between austenite and martensite was also investigated.

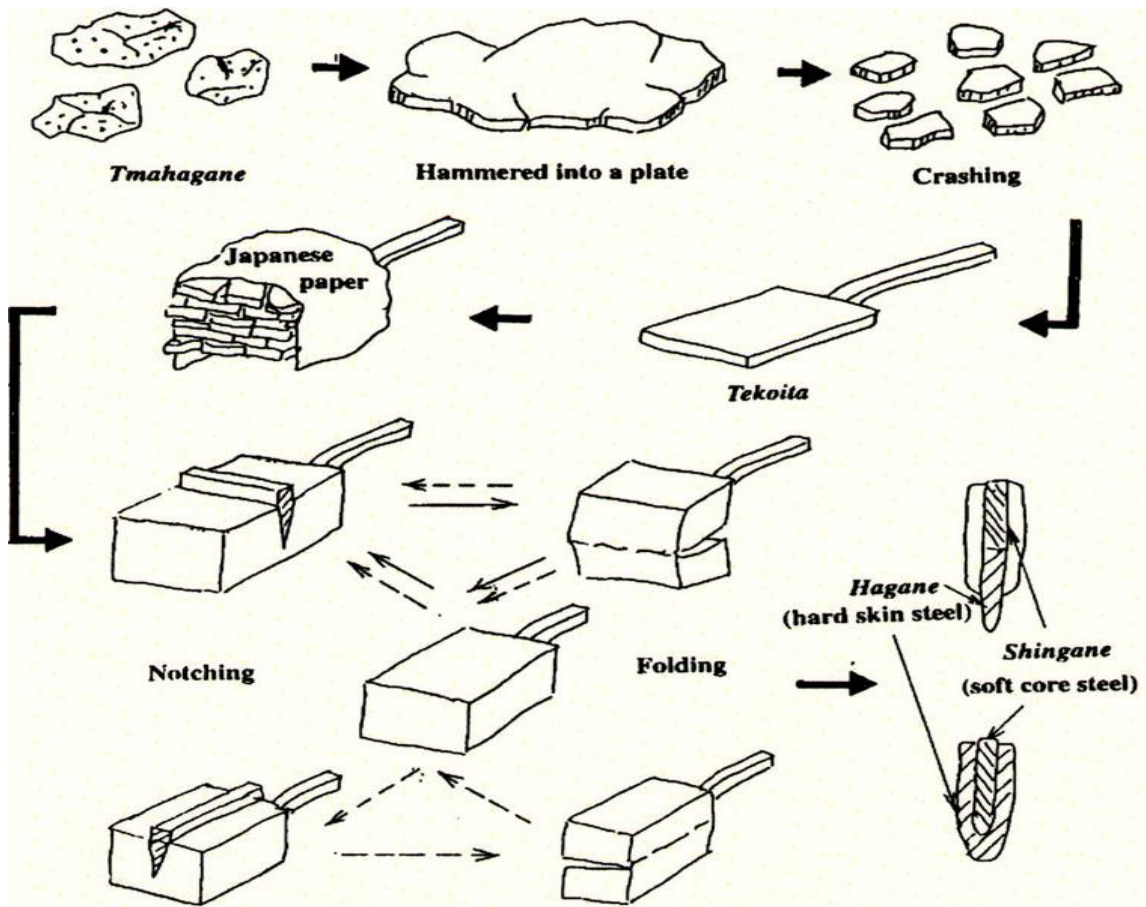


Figure 2.1. Traditional method for preparing Japanese sword [1].

Schematic description of traditional method for preparing Japanese sword is shown in Fig.2.1 [1]. Traditionally, the raw material for preparing Japanese sword is a kind of sponge steel called tamahagane, which is made by a tataru process [1-2]. This steel is high-carbon steel with 1-1.4 mass% C [1-2]. The tamahagane chips are sorted by carbon content and forge-welded into a block. This block is then undergone 12-15 fold-forging cycles in order to reduce the carbon content to a desired level [1-3]. The fold-forging operations are conducted in austenite state, at high temperature around 1573K [1-3]. This process aims for compositional homogeneity with fine and even distribution of non-metallic inclusions. After 12 cycles, the average carbon content was reduced to 0.6-0.7 mass% [1-4]. The microstructure is pearlite (P) and grain boundary ferrite (F).

Most of non-metallic inclusions were removed, while the others were broken-up and spheroidized [2]. A duplex construction of the sword was made by enclosing a low-carbon steel core by the high-carbon cover. The blade was partially shaped by a sequence of local heating to 1373K and hammering [1-2]. After shaping, the sword was coated by a clay mixture. This coating is thin at the cutting edge, but thick at the ridge. The final heating temperature is about 1073K [1-2]. As a result of selective quenching, the sharp edge was hardened with lath martensite, while the ridge due to slower cooling rate transformed to a mixture of pearlite + ferrite. The core is ferrite with small amount of pearlite [1-2].

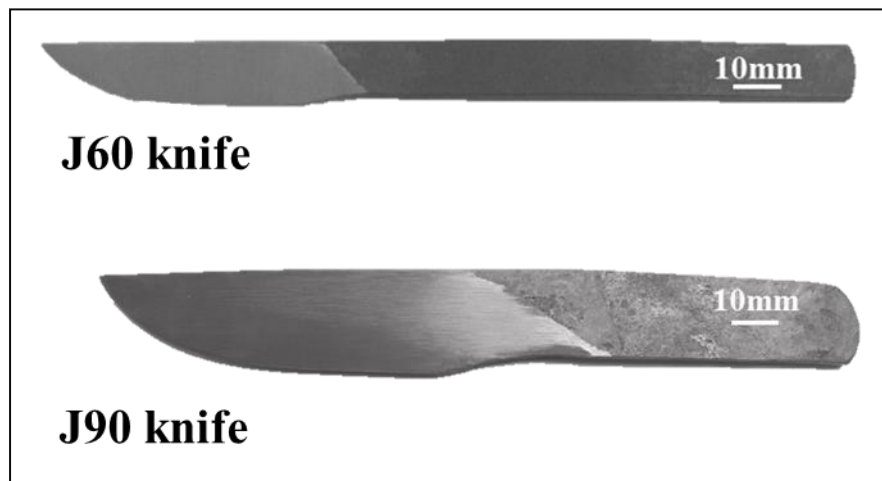


Figure 2.2. Two short knives prepared by traditional sword making method.

Table 2.2. The final composition of two short knives (mass%).

Steel	Final composition, mass%					
	C	Si	Mn	P	S	Fe
J60	0.62	0.01	0	-	-	Bal.
J90	0.86	0.15	0.22	0.005	0.001	Bal.

The carbon steels are J60 and J90 with original carbon content of 0.76 and 0.98 mass%, respectively. These steels were used for preparing two short knives by a traditional method, which has been used for making Japanese sword as described above. Both of steels were undergone about 12 successive fold-forging operations with formation of two short knives. Since the microstructure of lath martensite at the sharp edge is of interest, the duplex construction with insertion of low carbon steel core was not applied for those knives. After preparation, the knives have full lath martensite microstructure [5], and the carbon contents of J60 and were reduced to 0.62 and 0.86 mass% respectively (table 2.2).

c) Low alloy steels

A series of low alloy steels with addition of Mn or Ni were used for study on the effect of those elements on OR between austenite and martensite. The chemical compositions of the steels were given in table 2.3. These steels came in form of 1.5mm thin strips. The strips were heated to 1327K by electric resistance with 150s holding

time, followed by a rapid quenching under high pressure water-jet. This heat treatment was aimed to obtain a microstructure of full lath martensite with fine prior austenite grain size. The effect of quenching rate on OR is also considered for this series of experiments.

Table 2.3. *Chemical composition of low alloy steels.*

Steel	C	Si	Mn	P	S	Ni	Cr	Mo	Fe
C10	0.09	0.01	0.01	0.001	0.002	0.01	0.01	0.01	Bal.
C10Mn15	0.10	0.01	1.48	0.001	0.002	0.01	0.01	0.01	Bal.
C10Mn30	0.10	0.02	2.96	0.001	0.002	0.01	0.01	0.01	Bal.
C10Ni15	0.09	0.01	0.02	0.001	0.002	1.58	0.01	0.01	Bal.
C10Ni30	0.09	0.01	0.02	0.001	0.002	3.16	0.01	0.01	Bal.

d) TiC included steel

A steel with excessive of TiC inclusions was designed for study on the effect of internal stress on formation of fine martensite morphology. The steel was named by its mass% of titanium as Ti10 with chemical composition given in table 2.4.

Table 2.4. *Chemical composition of low alloy steels.*

Steel	C	Si	Mn	P	S	Ti	Fe
Ti10	0.23	0.01	2.92	0.006	0.002	1.00	Bal.

The steel has a near stoichiometric composition of TiC ($Ti/C = 3.986$) with slightly excessive amount of Ti. Thermo-Calc calculation shows that the amount of dissolved TiC and of solution carbon (mass%) in austenite of this steel in equilibrium condition at temperature range 1103K-1623K can be exponentially expressed through the temperature T (Kelvin) by the following equations:

$$\ln(\rho_{TiC}) = 7.471 \ln(T) - 56.031 \quad (2.1).$$

$$\ln(\rho_C) = 7.471 \ln(T) - 57.637 \quad (2.2).$$

where ρ_{TiC} and ρ_C are the solubility of TiC and C in austenite respectively.

For the chosen austenitizing temperature of 1573K, the amount of TiC and Carbon dissolved in austenite of this steel calculated by using Eq.2.1 and Eq.2.2 are 0.348 and 0.070 (mass%), respectively. Therefore the steel C10 without TiC was chosen as a reference with C concentration closed to the equilibrium concentration of C in this steel Ti10 at 1573K. The steel in form of a hot rolled bar was annealed at 1573K for 86ks in tube vacuum furnace and then slowly cooled down to 973K in Ar gas flow, kept at this temperature for 7.2ks followed by water cooling.

When high annealing was chosen for maximized dissolution of TiC into the austenite, the slow cool and rest at 973K was designed for precipitation of TiC. The A3 temperature determined from phase diagram of this steel, which was calculated by

Thermo-calc software with TCFE5.0 data base, is approximately 1073K. However, experimental result shown that the austenite is stable at 973K since after 7.2ks rested at this temperature followed by water quench there was not any evidence of ferrite transformation observed. It is likely that the Ar3 temperature is well bellowed equilibrium A3 temperature determined from phase diagram. Another reason is that the TCFE5.0 data may not be designed for the present steel with extra addition of Ti. Therefore, large scatter of calculated A3 temperature from its true value may be expected. The calculated A3 temperature was used as reference in choice of secondary holding temperature. After trial and error, the lowest second holding temperature was chosen as 973K, since high density of micron-sized TiC particle was observed in the heat treated specimen.

2.2. Experimental techniques

2.2.1. Optical and scanning electron microscopy (OM and SEM)

Optical microscopy is the oldest technique for microstructure observation [6]. In this study, the optical microscope NIKON-Eclipse LV150 was used for examination of initial and heat treated microstructures of specimens. The main purpose of using optical microscopy is primary examination of microstructure before SEM and EBSD experiments. For this purpose the technique is useful owing to simple sample preparation and fast operation. The sample for OM observation was prepared in accordance with standard procedure given in the common handbooks of sample preparation [6-7]. The sample was mechanical ground and polished with final polishing by 0.05 μm suspension silica solution. The etching agent used for all of specimens is 3% Nital solution. Scanning electron microscope was used for higher resolution observation of microstructure. All of the observations were conducted on a JEOL 7001FA field emission scanning microscope (FE-SEM). The sample was mechanically polished by the same procedure applied for OM [8]. The typical setting of SEM observation for secondary electron imaging (SEI) mode is 15kV voltage and 10mm working distance.

2.2.2. Electron backscatter diffraction (EBSD)

Automated EBSD is a powerful technique for local orientation measurement on a SEM. The automated EBSD system consists of three parts: the SEM, the acquisition hardware and the controlling software [9-10]. A high-speed DigiView CCD camera was installed inside the JEOL 7001FA for EBSD pattern acquisition. The software package EDAX/TSL OIM DC 5.2 was used for controlling digital beam scanning, storing and analyzing the data. Sample for EBSD experiment was mechanically polished by the same procedure applied for SEM [8]. A proper mechanical polishing can results a good surface, which is suitable for high quality of EBSD pattern for all sample steels except TiC included one. In that steel, the TiC particles built up on the polished surface of martensite matrix, since the very hard TiC particles have a much higher resistance to wear than that of the matrix (Fig. 2.3). Such finished surface is not appropriate for EBSD experiment, because the EBSD pattern taken from TiC particles has very low

quality. In that case, the TiC particles were mostly unable to be indexed, or they were indexed incorrectly as ferrite phase.

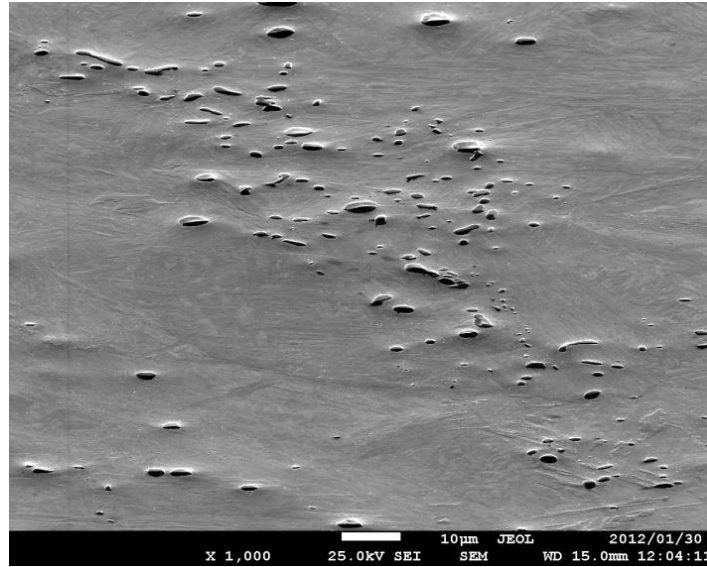
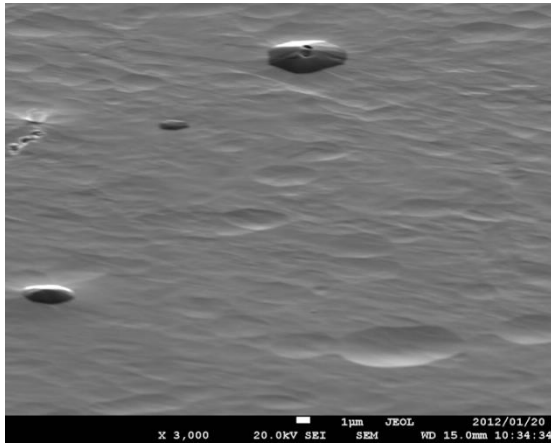
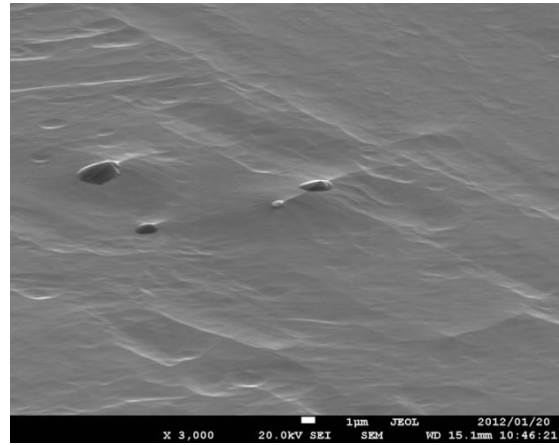


Figure 2.3. *Mechanical polished surface of Ti10 steel.*

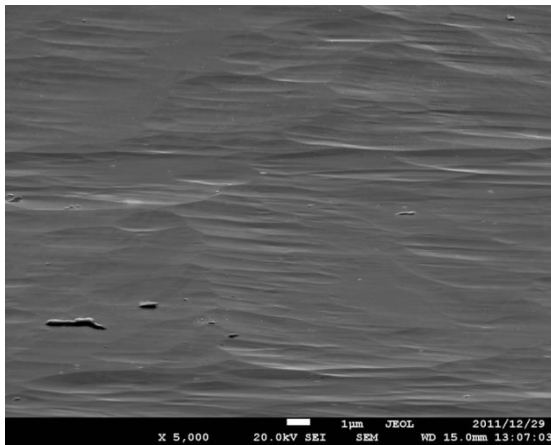
The only method for preparing a relatively smooth surface for Ti10 steel is ion polishing. The equipment used for this purpose was GATAN 691 PIPS - precise ion polishing system, which uses double beams of Ar^+ ion for sputtering the material from the specimen surface. Ordinarily, this system is built for precise polishing the surface of TEM thin foil specimen, so the EBSD specimen subjected to ion milling was cut in form of 3mm disk with the thickness about $300\mu\text{m}$ to fit the top mount attachment of the equipment. Since there has not been any report on the setting parameters of the machine for ion polishing of the specimen with TiC particle. A series of experiments was set up with the parameters taken from user manual of the equipment and several reported articles on ion milling for other materials [11-13]. The surface of specimen after each polishing procedure was checked in SEM with a tilt 70° relative to the incident electron beam. The results are shown in Fig.2.4. The main setting parameters of the PIPS were accelerating voltage (eV), milling angle (the angle between the incident beam and specimen surface) and milling time in ks. Those parameters are given under each SEM micrograph of the corresponding specimen (Fig.2.4).



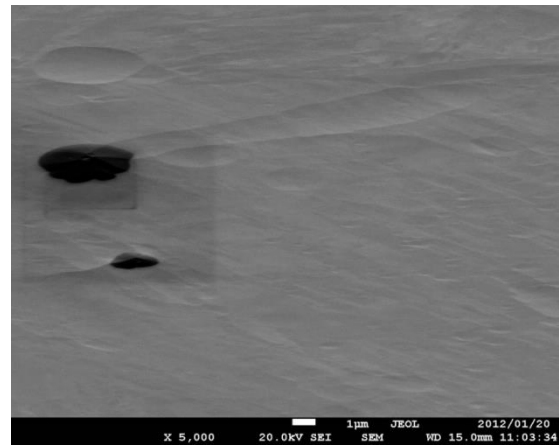
4keV-10°- 1.8ks



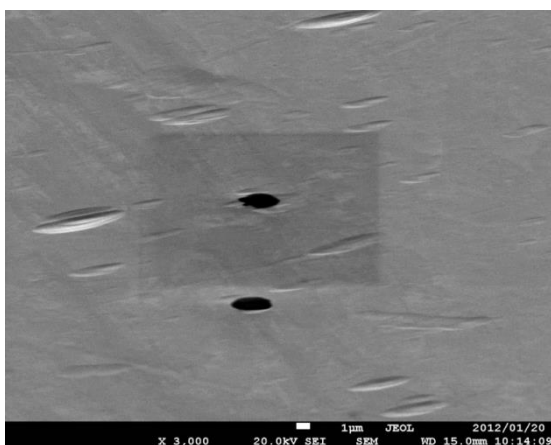
4kV-10°- 0.9ks



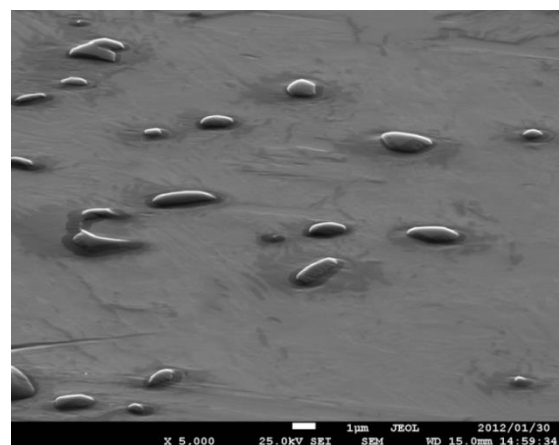
4kv-4°- 2.7ks



4kV-4°-1.8ks



4keV- 2°- 1.8ks



2keV - 2° - 1.8ks

Figure 2.4. SEM images of ion polished surfaces with various setting parameters

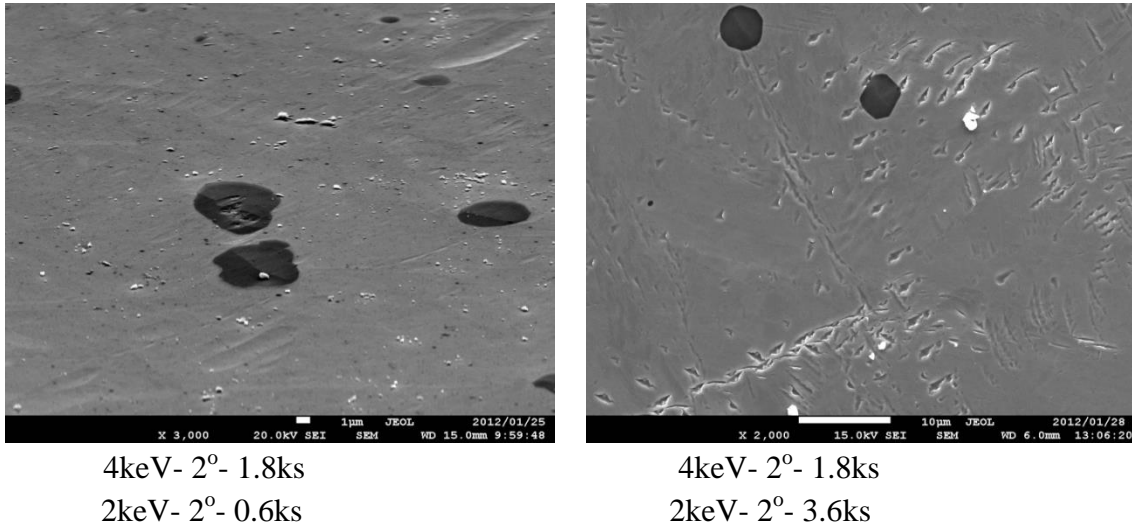


Figure 2.4. SEM images of ion polished surfaces with various setting parameters (continued).

A double ion milling procedure with 4keV, 2° for 1.8ks and subsequent 2keV, 2° for 0.6ks results the best surface quality for EBSD measurement of Ti10 steel. The TiC particles were able to be indexed and the interface boundaries between the particles and the matrix were clearly observed.

For EBSD experiment, the sample with properly finished surface was tilted 70° relative to the incident beam. The normal setting of the SEM is 25kV accelerating voltage, 13nA current probe and 15mm working distance and 100 nm scanning step at about x1000 magnification. For high resolution observation, those parameters were chosen as 15kV, 1.86nA, 15 mm and 40 nm at x10.000 magnification.

Reference

- 1) T. Inoue: Acta Mech. **214**, No.1-2 (2010) 17-30.
- 2) B. Dodd: Mech. Working Tech. **2** (1978) 75-84.
- 3) N. Sasaki, T. Momono: Tetsu-to-Hagané **93** (2007) 792-798.
- 4) G. Takami, T. Ohba, S. Morito, A.K. Das: Mater. Sci. Forum **654-656** (2010) 134-137.
- 5) A.K. Das, T. Ohba, S. Morito, M. Yaso: Mater. Sci. Forum **654-656** (2010) 138-141.
- 6) B.L. Bramfitt, A.O. Benscoter: ASM Int. (2001) pp. 354.
- 7) K. Geels: ASM Int. (2007) pp. 743.
- 8) P. Echlin: Springer (2009) pp. 330.
- 9) A.J. Schwartz, M. Kumar, B.L. Adams, D. Field (ed.): Springer (2009) pp. 403.
- 10) Zhou, Weilie; Wang, Zhong Lin (ed.): Springer (2007) pp. 522.
- 11) N. Mateescu, M. Ferry, W. Xu, J.M. Cairney: Mater. Chem. and Phys. **106**, No.1 (2007) 142-148.
- 12) D.A. Carpenter, R.L. Bridges: Microsc. Today **16** (2008) 28-31.
- 13) L. Koll, P. Tsipouridis, E.A. Werner: Microsc. **234** (2011) 206-219.

Chapter 3

Development of a computational method for EBSD data analyses

Some essential modifications were introduced to the ordinary fitting method to make it become a powerful method for thorough crystallographic and morphological analyses of lath martensite based on electron backscatter diffraction (EBSD) data. A large area of martensite which covers a whole prior austenite grain can be effectively analyzed. The austenite orientation and orientation relationship between martensite and austenite can be obtained by fitting from martensite orientations. The fitting procedure is fast with high precision up to 0.5 degrees for austenite orientation and 0.2 degrees for the orientation relationship. The output data are also modified for automatically indexing martensite variants and visual plotting of the results.

3.1. Introduction

Recently, EBSD method has been used intensively to study morphology and crystallography of martensite in steel [3-36]. The EBSD method allows a large area of martensite up to several millimeters square to be analyzed [1-2]. Many aspects of morphology can be obtained such as, packet size, block and sub-block sizes, and their distribution maps [19-34]. For analyzing martensite structures, essential crystallographic information is orientation relationship between parent austenite and transformed martensite. If transformed martensite contains enough amount of retained austenite, one can easily deduce the orientation relationship from EBSD data. However, one cannot readily obtain orientation relationship for martensite with little amount of retained austenite, such as martensite of low-carbon steels. In previously reported papers the orientation relationship is often supposed to be Kurdjumov-Sachs (K-S) type [38], though the results shown a certain deviation from the exact K-S [22-26, 39-44]. A numerical fitting method had been applied for orientation relationship analysis of martensite and bainite in steels by Miyamoto et al. [40] with dual fitting of both austenite orientation and orientation relationship by a single fitting criterion. The obtained orientation relationship is reported to be close to Greninger-Troiano (G-T) [37] type and locally varied within one prior austenite grain due to transformation strain [40]. Until now, the main disadvantage of fitting method to obtain orientation relationship from observed martensite orientation is that the process takes a lot of time for finding a solution from a relatively small EBSD data set (thousands of scan points). If taking calculation time into consideration, the method is only capable to obtain orientation relationship from a part of austenite grain, instead of the whole grain. When small parts of one prior austenite are used for fitting austenite orientation and orientation relationship, the scatter of obtained results can increase up to $\pm 1^\circ$, especially for austenite orientation. By introducing some essential modifications of calculation and fitting, we are now able to apply the fitting procedure for a large EBSD set (hundred thousands of scan points), which covers a whole prior austenite grain for a relatively

short running time. Thus the precision of fitting method is improved with a reliable and reproducible result. Moreover, by using the fitting method, we provide other advantages which allow automatically indexing martensite variants and visually plotting of various analytical results.

3.2. Fitting austenite orientation and orientation relationship from martensite

3.2.1. Calculation method

Generally the orientation of martensite variants can be generated from given austenite orientation and orientation relationship between austenite and martensite by Eq.(3.1). All of the orientations mentioned herein are in form of 3x3 matrices.

$$\mathbf{M}_{i_{\text{standard}}}^{\text{bcc}} = (\mathbf{OR}_1^{\text{fcc-bcc}} \mathbf{C}_i) \mathbf{A}^{\text{fcc}}, \quad i = 1 - 24 \quad (3.1).$$

Where, $\mathbf{M}_{i_{\text{standard}}}^{\text{bcc}}$: orientation of i^{th} standard martensite variants generated by given austenite orientation and orientation relationship; \mathbf{A}^{fcc} : orientation of austenite; \mathbf{C}_i : i^{th} conversion matrix of 24 symmetry operations for cubic system (Table 3.1); $\mathbf{OR}_1^{\text{fcc-bcc}}$: the 1st variant of orientation relationship in martensite frame.

Table 3.1 *Twenty four conversion matrices for cubic system.*

$$\begin{array}{cccccc} \mathbf{C}_1 = \begin{bmatrix} 1 & 0 & 0 \\ 0 & 1 & 0 \\ 0 & 0 & 1 \end{bmatrix} & \mathbf{C}_2 = \begin{bmatrix} 0 & 0 & -1 \\ 0 & -1 & 0 \\ -1 & 0 & 0 \end{bmatrix} & \mathbf{C}_3 = \begin{bmatrix} 0 & 0 & 1 \\ 1 & 0 & 0 \\ 0 & 1 & 0 \end{bmatrix} & \mathbf{C}_4 = \begin{bmatrix} 0 & -1 & 0 \\ -1 & 0 & 0 \\ 0 & 0 & -1 \end{bmatrix} & \mathbf{C}_5 = \begin{bmatrix} 0 & 1 & 0 \\ 0 & 0 & 1 \\ 1 & 0 & 0 \end{bmatrix} & \mathbf{C}_6 = \begin{bmatrix} -1 & 0 & 0 \\ 0 & 0 & -1 \\ 0 & -1 & 0 \end{bmatrix} \\ \mathbf{C}_7 = \begin{bmatrix} 0 & 0 & 1 \\ 0 & -1 & 0 \\ 1 & 0 & 0 \end{bmatrix} & \mathbf{C}_8 = \begin{bmatrix} -1 & 0 & 0 \\ 0 & 1 & 0 \\ 0 & 0 & -1 \end{bmatrix} & \mathbf{C}_9 = \begin{bmatrix} 1 & 0 & 0 \\ 0 & 0 & 1 \\ 0 & -1 & 0 \end{bmatrix} & \mathbf{C}_{10} = \begin{bmatrix} 0 & 1 & 0 \\ 0 & 0 & -1 \\ -1 & 0 & 0 \end{bmatrix} & \mathbf{C}_{11} = \begin{bmatrix} 0 & -1 & 0 \\ 1 & 0 & 0 \\ 0 & 0 & 1 \end{bmatrix} & \mathbf{C}_{12} = \begin{bmatrix} 0 & 0 & -1 \\ -1 & 0 & 0 \\ 0 & 1 & 0 \end{bmatrix} \\ \mathbf{C}_{13} = \begin{bmatrix} 0 & 1 & 0 \\ -1 & 0 & 0 \\ 0 & 0 & 1 \end{bmatrix} & \mathbf{C}_{14} = \begin{bmatrix} 0 & 0 & -1 \\ 1 & 0 & 0 \\ 0 & -1 & 0 \end{bmatrix} & \mathbf{C}_{15} = \begin{bmatrix} 0 & 0 & 1 \\ 0 & 1 & 0 \\ -1 & 0 & 0 \end{bmatrix} & \mathbf{C}_{16} = \begin{bmatrix} 1 & 0 & 0 \\ 0 & -1 & 0 \\ 0 & 0 & -1 \end{bmatrix} & \mathbf{C}_{17} = \begin{bmatrix} -1 & 0 & 0 \\ 0 & 0 & 1 \\ 0 & 1 & 0 \end{bmatrix} & \mathbf{C}_{18} = \begin{bmatrix} 0 & -1 & 0 \\ 0 & 0 & -1 \\ 1 & 0 & 0 \end{bmatrix} \\ \mathbf{C}_{19} = \begin{bmatrix} 1 & 0 & 0 \\ 0 & 0 & -1 \\ 0 & 1 & 0 \end{bmatrix} & \mathbf{C}_{20} = \begin{bmatrix} 0 & -1 & 0 \\ 0 & 0 & 1 \\ -1 & 0 & 0 \end{bmatrix} & \mathbf{C}_{21} = \begin{bmatrix} 0 & 1 & 0 \\ 1 & 0 & 0 \\ 0 & 0 & -1 \end{bmatrix} & \mathbf{C}_{22} = \begin{bmatrix} 0 & 0 & 1 \\ -1 & 0 & 0 \\ 0 & -1 & 0 \end{bmatrix} & \mathbf{C}_{23} = \begin{bmatrix} 0 & 0 & -1 \\ 0 & 1 & 0 \\ 1 & 0 & 0 \end{bmatrix} & \mathbf{C}_{24} = \begin{bmatrix} -1 & 0 & 0 \\ 0 & -1 & 0 \\ 0 & 0 & 1 \end{bmatrix} \end{array}$$

To find a solution for austenite orientation and orientation relationship from EBSD data of experimental martensite orientations, one should find a standard martensite variant $\mathbf{M}_{i_{\text{standard}}}^{\text{bcc}}$ which has the smallest misorientation $\Delta\theta_k$ from a given k^{th} experimental orientation $\mathbf{M}_{k_{\text{experiment}}}^{\text{bcc}}$ (Eq. (3.2))

$$\Delta\theta_k = \min\{\arccos([\text{tr}(\mathbf{M}_{i_{\text{standard}}}^{\text{bcc}} (\mathbf{M}_{k_{\text{experiment}}}^{\text{bcc}} \cdot \mathbf{C}_j)^{-1}) - 1]/2)\}, \quad \forall i, j = 1 - 24 \quad (3.2).$$

Where, $\text{tr}(\mathbf{M}_{i_{\text{standard}}}^{\text{bcc}} (\mathbf{M}_{k_{\text{experiment}}}^{\text{bcc}} \cdot \mathbf{C}_j)^{-1})$ is the trace of misorientation matrix $\mathbf{M}_{i_{\text{standard}}}^{\text{bcc}} (\mathbf{M}_{k_{\text{experiment}}}^{\text{bcc}} \cdot \mathbf{C}_j)^{-1}$. The solution can be found by minimization of average over all

experimental data $\Delta\theta_{\text{average}} = \sum_{k=1}^N \Delta\theta_k / N \rightarrow \min$, where N is the number of scan points.

Due to the symmetry, an arbitrary orientation in cubic system can be represented by any of 24 mathematically distinguished matrices. Hence, the total number of matrix operations, which is required to find the minimum misorientation angle $\Delta\theta_k$ for a given k^{th} experimental orientation $M_{k_{\text{experiment}}}^{\text{bcc}}$ in Eq.(3.2), is $24 \times 24 = 576$ operations.

Each orientation of cubic system in a three dimensional reference frame is characterized by three independent variables as minimum. To find both austenite orientation and orientation relationship simultaneously we have to deal with six independent variables x_i , $i = 1-6$. The numerical fitting approach was applied for finding the global minimum of $\Delta\theta_{\text{average}}$ with a given fitting interval d and fitting step s . All six variables are allowed to change independently from $x_i^0 - d$ to $x_i^0 + d$ with increasing step s , where x_i^0 are the initially given values of x_i . Obviously, the global minimum of $\Delta\theta_{\text{average}}$ within fitting interval $\pm d$ can be found with the error proportional to the fitting step s . By this algorithm, the total matrix operations which are required to find both austenite orientation and OR by using 6 variables are increased by $f^3 \times f^3 = f^6$ times, where $f = 2d/s$, is the number of fitting steps.

Generally the total number of matrix operation which required for fitting both austenite orientation and orientation relationship by the conventional fitting method as described above, for EBSD data set with N scan points is

$$f^3 \times f^3 \times 24 \times 24 \times N = 576 f^6 N \quad (3.3).$$

For a normal data set of 30,000 scan points with number of fitting steps $f = 10$, the total number of matrix operation is 1.72×10^{13} . The large required number of matrix operation explains why the fitting method for a normal or large EBSD data set takes a lot of operating time. If one would like to have the solution for a reasonable calculation time, the available data set should be quite small as several thousand of scan points. For a normal EBSD mode with $0.2 \mu\text{m}$ scanning step, at least 62,500 scan points are required to observe a whole prior austenite grain, which size is normally more than $2,500 \mu\text{m}^2$ for low-carbon steel. In our approach, we applied modifications to the conventional fitting method to improve its performance and reliability as described below.

3.2.2. Fitting austenite orientation and orientation relationship separately

The orientation relationship between lath martensite and austenite is reported to be varying from K-S, Nishiyama–Wassermann (N-W) or G-T by different researchers working on different sample steels [33-35,37-44]. However, all the reported orientation relationships are quite close to each other. For instant, the difference between K-S and N-W is only 5.26° . The misorientation between K-S and G-T is 2.40° , while misorientation between N-W and G-T is 2.86° . A TEM observation by Kelly et al. [48] showed that the orientation relationship in case of lath martensite is almost constant although the orientation relationships were extracted from very thin and heavily deformed retained austenite films and their neighbor martensite regions. Based on this fact, we consider that the orientation relationship is constant or almost constant with small variation for given steel with a known chemical composition.

Using this idea, we have been tried to fix the orientation relationship for fitting only austenite orientation to reduce the number of calculation operations. For the first trial we used K-S orientation relationship to fit austenite orientation. Note that the austenite orientation term used here means average orientation overall the prior austenite grain before martensitic transformation. After finding a solution of austenite orientation, the orientation relationship was fitted by fixing austenite orientation. The new fitted orientation relationship is found to be close to G-T for various steels with different chemical composition. For further fitting, the obtained orientation relationship will be used as the initial orientation relationship instead of K-S to fit austenite orientation, since the initial orientation relationship is closer to the fitted orientation relationship than the K-S. By using this approach the multiple to the operations which are required to find both austenite orientation and orientation relationship by numerical fitting is equal to $2xf^3$ instead of f^6 .

3.2.3. Using the characteristics of $(001)_{\alpha'}$ pole figure

The $(001)_{\alpha'}$ pole figure of experimental points (Fig.3.1) for typical EBSD data of martensite within one prior austenite grain shows a ring-like distribution of $(001)_{\alpha'}$ martensite orientations around each pole of $(001)_{\gamma}$ austenite orientation, which is referred as a Bain group [45-46]. Within a Bain group, there are 8 martensite variants and the misorientations between $(001)_{\alpha'}$ poles of 8 martensite variants and the corresponding $(001)_{\gamma}$ austenite pole are ideally the same and smaller than 15° for all reported orientation relationships. By classifying the experimental points of martensite into three Bain groups, we now have to deal with only 8 martensite variants in a Bain group instead of all 24 variants. Furthermore, the operation, which we have to deal with, is only between two vectors.

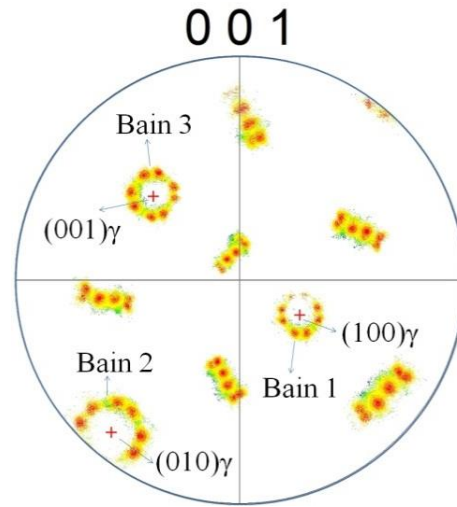


Figure 3.1 Typical (001) pole figure of lath martensite transformed from one prior austenite grain.

Assuming a martensite orientation is expressed in a matrix form as (\mathbf{m}_i) , $i=1-3$, where \mathbf{m}_i are three orthogonal unit vectors. In the same manner, the orientation of austenite is (\mathbf{a}_j) , $j=1-3$. As seen in the Fig. 1, the martensite orientation belongs to a given Bain group k ($k=1-3$) if and only if the minimum angle between \mathbf{m}_i and \mathbf{a}_j is equal to the minimum angle between \mathbf{m}_i and \mathbf{a}_k

$$\min\{\angle(\mathbf{m}_i, \mathbf{a}_j)\} = \min\{\angle(\mathbf{m}_i, \mathbf{a}_k)\}, \quad \forall i, j = 1-3 \quad (3.4).$$

The total vector operations required to find such of vector \mathbf{a}_k for a given martensite orientation (\mathbf{m}_i), is $3 \times 3 = 9$. Hence, it requires 9 vector operations to find the closest Bain group and 8 vector operations to find the candidates for the closest martensite variant in the Bain group. The total vector operations required for finding the closest martensite variant to a given experimental point are $9 + 8 = 17$ operations. If we consider three vector operations are equal to one matrix operation, the number of equivalent matrix operations is only 6 for each experimental point.

3.2.4. Simplifying the calculation of misorientation angle between two close orientations

From pole figure we have already noted that the misorientation between the experimental point and the nearest standard martensite variant is small and less than 15° . We also made an assumption that, if there is a combination of two cubic orientations O_1 ($Oxyz$) and O_2 ($Ox'y'z'$) with small misorientation providing that $\alpha_x = \min\{\alpha_x, \beta_x, \gamma_x\}$, where $\alpha_x = \angle(Ox, Ox')$, $\beta_x = \angle(Oy, Ox')$, $\gamma_x = \angle(Oz, Ox')$; by analogy $\alpha_y = \min\{\alpha_y, \beta_y, \gamma_y\}$, $\alpha_z = \min\{\alpha_z, \beta_z, \gamma_z\}$, then the misorientation angle calculated for the given combination is the smallest and can be accepted as the true misorientation angle between O_1 and O_2 .

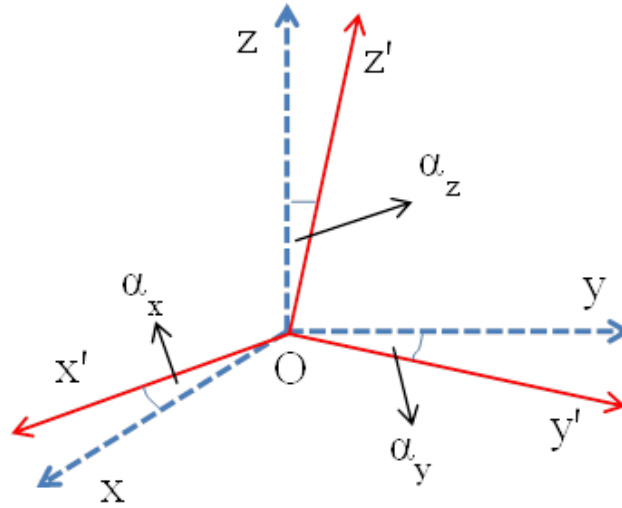


Figure 3.2. A symmetry of orientation O_2 ($Ox'y'z'$) in frame of orientation O_1 ($Oxyz$) giving the smallest misorientation between them.

Now we will approve this assumption. When the orientation O_1 is fixed as a reference coordinate system $Oxyz$, the trace of rotation matrix from O_2 to O_1 will be equal to $\cos(\alpha_x) + \cos(\alpha_y) + \cos(\alpha_z)$. The misorientation angle θ between O_1 and O_2 is

$$\cos \theta = (\cos \alpha_x + \cos \alpha_y + \cos \alpha_z - 1) / 2 \quad (3.5).$$

If misorientation between O_1 and O_2 is known to be smaller than 15° the minimum misorientation (Fig.2) can be deduced from the Eq.(3.5), providing that

$$\alpha_x = \min\{\alpha_x, \beta_x, \gamma_x\}, \alpha_y = \min\{\alpha_y, \beta_y, \gamma_y\}, \alpha_z = \min\{\alpha_z, \beta_z, \gamma_z\}.$$

Since $(\cos\alpha_x)^2 + (\cos\beta_x)^2 + (\cos\gamma_x)^2 = 1$ then $\cos\alpha_x \geq 1/\sqrt{3}$ or $\alpha_x < \arccos(1/\sqrt{3}) \approx 55^\circ$, by analogy α_y and $\alpha_z < 55^\circ$. Thus, $\cos\theta$ calculated from Eq.(3.5) will have maximum value or θ will be minimum misorientation angle.

By using this theorem we avoided using 24 conversion matrices C_i for finding the misorientation between O_1 and O_2 . Therefore we can use only one matrix operation instead of twenty four to find the true misorientation between the two close orientations. In addition to the above mentioned modifications, the total number of matrix operations required for fitting austenite orientation and orientation relationship is

$$2 \times f^3 \times 6 \times N = 12 f^3 N \quad (3.6).$$

For the same value of N and f given above, the total number of required matrix operations is 3.6×10^8 . With the modifications described in section 3.2.2–3.2.4, we were able to reduce the required matrix operations by 4.8×10^4 times.

3.2.5. Using two criteria for fitting

When using minimum average misorientation as the only criterion for fitting austenite orientation by our method, we often found an erroneous solution of austenite orientation. It is found that the erroneous solution well minimizes the average misorientation, but only a small number of experimental points are assigned to calculated martensite variants within a given tolerance of misorientation. Hence, we introduced an additional criterion that the number of experimental points assigned to martensite variants within a given tolerance angle should be maximum.

Thus the two criteria for fitting are:

- 1) minimum average misorientation – $\Delta\theta_{\text{average}}$;
- 2) maximum number of experimental points which can be assigned to martensite variants within a given tolerance angle – N_{fit} .

Ideally, the solution of austenite orientation may not simultaneously satisfy the smallest value of average misorientation $\Delta\theta_{\text{average}}$ and maximum number of fitted experimental points – N_{fit} . For numerical fitting, a combined criterion was made by dividing the average misorientation by the total number of fitted experimental points: $\Delta\theta_{\text{average}}/N_{\text{fit}}$. By using the combined criterion for the fitting, the solution now is reliable and reproducible during a repeated running cycle with any set of EBSD data.

3.3. Evaluation of the new fitting program

3.3.1. Experimental

The low alloy steel C10Mn30 was used for EBSD experiment. The thin specimen was heated to 1327K by electric resistance with 150s holding time, followed by a rapid quenching under high pressure water-jet. This heat treatment was aimed to obtain a microstructure of full lath martensite with average prior austenite grain size of $70\mu\text{m}$. The sample was cut for EBSD observation from a center part of the specimen and mechanically polished. The EBSD experiment was conducted on a JEOL JSM7001FA field emission gun scanning electron microscope equipped with TSL©EBSD data collection system. The scan was performed at 25kV accelerating voltage and 13nA probe current with scanning step of $0.2\mu\text{m}$ at x1000 magnification. Three prior austenite grains which were numbered as grain 1, grain 2 and grain 3, were analyzed by our improved fitting method. Five different parts of the grain 1 (see Fig.3.3), which are

notated from P1 to P5, were also used for fitting austenite orientation and orientation relationship (Table 3.3).

3.3.2. Coarse fitting and fine fitting

Based on the above described algorithm, a computer program for fitting austenite orientation and OR was written in Fortran 90, which can run on any personal computer (PC) with Windows operating system. For certain demands, the fitting procedure can be processed either in coarse mode or in fine mode. A coarse fitting mode includes only coarse fitting phase, while a fine fitting mode requires both coarse and fine fitting phases. The coarse fitting phase uses the trial austenite orientation and the general orientation relationship as input parameters. The fitting interval is from -3° to $+3^\circ$ and the fitting step is 1° ($f = 6$). Fine fitting phase uses the results of coarse fitting phase as the input. Fitting interval is from -1° to $+1^\circ$ and the fitting step is 0.2° ($f=10$). Figure 4 shows how the running time of coarse and fine fitting mode for finding both austenite orientation and orientation relationship depend on the data volume. The EBSD data of the grain 1, which has 153,000 scan points, was analyzed in both coarse and fine fitting mode. The difference between the obtained austenite orientations is 0.33° , while the orientation relationships are identical. The coarse mode can be applied for rapid fitting austenite orientation and orientation relationship since it is much faster than fine fitting with precision better than 0.5° . For presenting the best capability of the improved method, all further examples are calculated by using the fine mode. The calculation speed was estimated on a normal Windows PC equipped with an Intel® Core™ i5 - 3.33GHz processor and 4GB of memory.

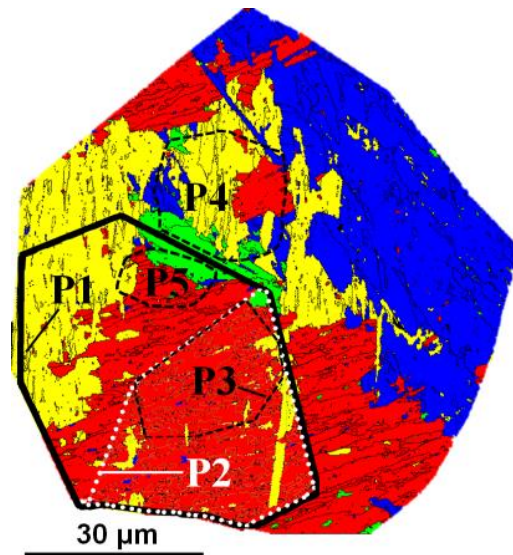


Figure 3.3. Grain 1 with its five parts (from P1 to P5) used for fitting austenite orientation and orientation relationship, the martensite variants are colored following parallel relationship between $(011)_{\alpha'}$ and four variants of $(111)_{\gamma}$ close-packed plane. The contour of P1 is denoted by solid black line, contour of P2 by dotted white line and contours of P3-P5 by dashed black line.

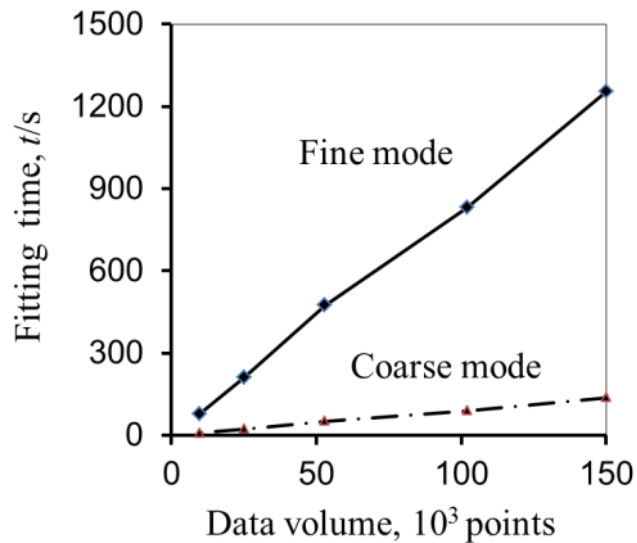


Figure 3.4. Fitting time for austenite orientation versus volume of data set.

3.3.3. Effect of scanning step on fitting results

For grain 1 (Fig.3.3), the EBSD data set with original scanning step $0.2\mu\text{m}$ was coarsened by using TSL OIM program which artificially doubled the scanning step per one coarsening cycle. After each coarsening cycle the data volume is decreased by 4 times, so the calculation time is respectively reduced by about 4 times. The details of coarsened data are given in Table 3.2. Up to three coarsening cycles the obtained results of austenite orientation for original data and coarsened data are ideally the same, whereas the tolerance of obtained orientation relationships is 0.1° (Table 2). It shows that using coarse data with scanning step up to $1.6\mu\text{m}$ is an effective way to reduce calculation time without the risk of losing the precision. By this measure, a large number of prior austenite grains or a very large grain can be effectively analyzed within reasonable time.

Table 3.2. Effect of coarsening EBSD data of grain 1 on fitting results.

Number of coarsening cycles		0	1	2	3	4
Scanning step, μm		0.2	0.4	0.8	1.6	3.2
Data volume, point		153,252	38,342	9,592	2,413	608
Calculation time, t/s		1287	351	103	21	6
Deviation from fitting of original data, $\theta/^\circ$	Austenite orientation	0.00	0.00	0.00	0.00	0.14
	Orientation relationship	0.00	0.07	0.07	0.09	0.15

3.3.4. Fitting for different parts of one austenite grain and for different austenite grains

EBSD data of five different parts of the grain 1, which contours are shown in Fig.3.3, were also used for analyses. In this figure, martensite variants are colored by their plane parallel relationship with austenite, namely $(011)_{\alpha'} // (111)_{\gamma}$ or close packed plane variant 1 (CP1) - red, $(011)_{\alpha'} // (1\bar{1}1)_{\gamma}$ or CP2 - yellow, $(011)_{\alpha'} // (\bar{1}11)_{\gamma}$ or CP3 - green and $(011)_{\alpha'} // (11\bar{1})_{\gamma}$ or CP4 - blue. All the five parts are cropped from original grain 1 with $0.2\mu\text{m}$ scanning step. Part 1 is cut from grain 1 so that it contains mainly 10 martensite variants of CP1, CP2 and CP3. Also the data volume of part 1 is about 0.3 fractions of the grain1's. Part 2 which is a half of part 1, contains 8 martensite variants of CP1 and CP2. Part 3 is cut from part 2 so that it covers 6 martensite variants of CP1 and CP2. Part 4 which has the same size as part 3, is cut from another region of grain 1 next to the part 1. Despite its small size, part 4 contains 17 martensite variants of four CP variants. Part 5 is cut from a very small region of part 1. This part covers 8 martensite variants of CP1 and CP3. The details of EBSD data of the five parts are given in Table 3.3 and Fig. 3.3.

Table 3.3. Details of EBSD data used for austenite orientation and orientation relationship fitting.

Name	Grain1	Part1	Part2	Part3	Part4	Part5	Grain2	Grain3
Notation	G1	P1	P2	P3	P4	P5	G2	G3
Data volume, point	153,000	53,694	25,557	9,885	9,820	3,638	167,043	152,352
Number of main martensite variants with fraction > 0.01	18	10	8	6	17	8	18	17

The deviations of fitting results obtained for each part from the results obtained by fitting the whole grain 1 were given in Fig.3.5. It shows that the deviation of fitted orientation relationship for each part changes in correlation with its data volume and the number of included martensite variants. For the smallest part which contains only 3,638 scan points, the difference is 0.48° . The tolerance of fitting orientation relationship is 0.2° for other parts of martensite which belong to the same prior austenite grain. The differences between orientation relationship obtained from fitting grain 1 and orientation relationships obtained from fitting grain 2 and grain 3 are within 0.2° .

The details of orientation relationship were presented by deviation between close-packed planes - θ_1 versus deviation between close-packed directions - θ_2 of austenite and martensite (Fig.3.6). The mean orientation relationship is characterized by $\theta_1 = 1.72^\circ$ and $\theta_2 = 2.63^\circ$. This orientation relationship is close to G-T type, which has $\theta_1 = 1.0^\circ$ and $\theta_2 = 2.50^\circ$. Average deviation over all orientation relationships obtained by fitting the EBSD data provided in Table 3 from the mean value is only 0.12° . Thus, for given steel the orientation relationship between martensite and austenite can be confirmed to be almost constant, with the tolerance of $\pm 0.2^\circ$ for all austenite grains.

In a previous work [40] for a 0.15mass%C - 1.5mass%Mn steel the orientation relationship between austenite and martensite ($15C^M$) was reported as $\theta_1 = 1.70^\circ$ and $\theta_2 = 3.0^\circ$, while the orientation relationship between austenite and bainite ($15C^B$) was θ_1

$=1.70^\circ$ and $\theta_2 = 2.6^\circ$ (Fig.3.6). In comparison with our result the deviation between θ_1 is very small, while the deviation between θ_2 is about 0.4° in case of austenite/martensite orientation relationship. Beside the reported fitting tolerance of about $\pm 0.3^\circ$, the deviation between orientation relationships obtained in previous and present works may be caused by the difference in chemical composition of studied steels [33-35,39-44].

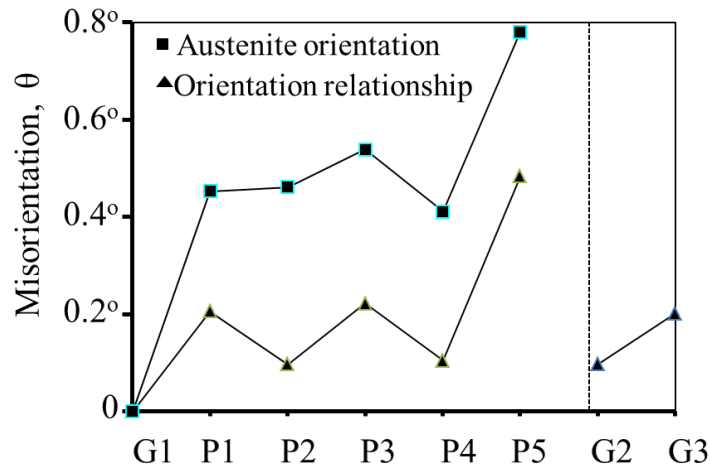


Figure 3.5. Deviation of orientation relationships and austenite orientations obtained by fitting separately five parts of grain1 as well as by fitting grain2 and grain3 from the results obtained by fitting grain1 as a whole.

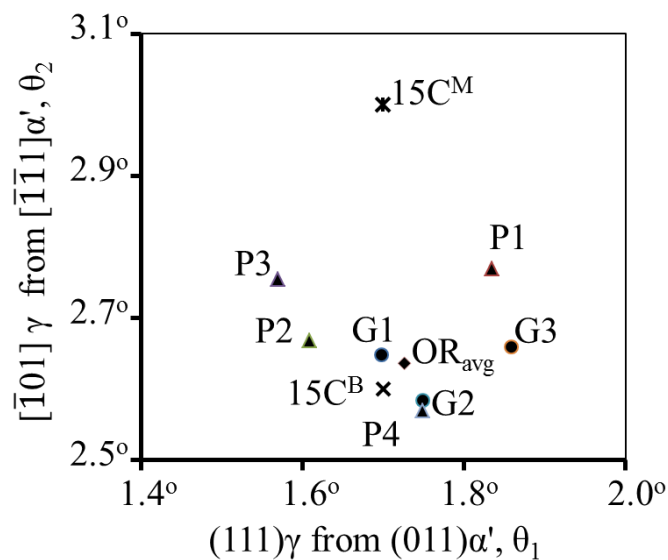


Figure 3.6 The obtained orientation relationships plotted in term of deviation between close-packed planes versus deviation between close-packed directions of austenite and martensite. Notations here correspond to that of Fig. 3 and Table 3. See text for 15C^B and 15C^M.

Deviation between austenite orientations obtained by fitting from part 1 to part 4 and the result obtained by fitting whole the grain is within 0.5° . For part 5 the deviation is

0.78° due to size effect of a very small part which contains only 3,638 scan points. It shows that a small part of one prior austenite grain, which covers about 0.1 fraction of the grain (as part 3 and 4) can be used for fitting austenite orientation giving the results with precision of $\pm 0.5^\circ$. Larger scatter of austenite orientation also implies that austenite orientations were locally changed due to transformation strain whereas the orientation relationship is almost unchanged.

3.4. Automatic indexing of martensite variants and visual plotting of morphological features

3.4.1. Automatic indexing of martensite variants

One who studies morphology of lath martensite often has problem with plotting the characteristic features of morphology such as packet, block, or variant (sub-block) maps, since these kinds of plots require manual indexing of martensite variants. An important advantage of this calculation is that after fitting austenite orientation and orientation relationship, we are able to analyze the data and modify the output file for automatically indexing martensite variants. After the treatment, various kinds of visual plotting can be plotted automatically and easily on the common commercial program for EBSD data analysis. Some examples of crystallographic and morphological analyses will be given for illustration and discussion.

When the austenite orientation and orientation relationship between martensite and austenite are known, various crystallographic and morphological analyses will be available from EBSD data. The automatic index of martensite variant is based on modification of the output data in TSL OIM “.ang” file format. The procedure for automatic indexing martensite variants can be described as follows:

- Selection of a martensite area, which is inherited from one austenite orientation with the assistance of $(001)_\alpha$ pole figure (this step is similar to the first step of manual indexing).
- Exporting the scan data of the selected area to a file with “.ang” format. This file contains EBSD scanning parameters, the sizes of selected area, and information of each scanning pixel. Each pixel is described by 10 parameters that are the orientation in format of three Euler angles, the two coordinates of the scan point, the image quality (IQ), the confident index (CI), the phase number and the detector intensity. Among those parameters, the CI value describes how confident the software is that it has correctly indexed the EBSD pattern. The CI value can be modified to any number, which will not affect either reading of output file or analyzing of the data.
- Fitting austenite orientation and OR by using the exported data of martensite orientations. After this step, the austenite orientation and OR will be calculated with the precision proportional to the fitting step.
- Automatic index of martensite variants. In this step, the fitted austenite orientation and OR will be used to calculate 24 martensite variants inherited from this austenite orientation. For each scan pixel, the minimum misorientation between measured orientation and one of calculated martensite variants will be found by the same algorithm as above description. If the misorientation is smaller than a chosen tolerance

angle, the measured orientation will be indexed by the variant number of the calculated one. The indexing will be made to the data by replacing the CI number of that scan point by the variant number. In case the minimum misorientation is larger than tolerance angle, the scan pixel will not be indexed and its CI value will remain untouched.

3.4.2. Visual plotting of morphological features

After indexing martensite variants for the selected austenite grain, the output “.ang” file is readily to be opened and analyzed by commercial program for EBSD data analysis. In this study, the OIM analysis 6.0 program was used. Using the indexed data, various visual plotting of martensite morphology of this grain such as packet map, block map, variant map, etc. can be done automatically. The method for automatic plotting of morphological maps is as follows:

- Opening the indexed data, where all of scan points are indexed by modifying their CI values.
- Plotting the CI map, in which different range of CI values is represented by different color. The color for each range of CI value is identified by the user. Since the modified CI value represents the martensite number, each martensite variant will be colored according to the color code defined by the user. By this way the morphological maps of martensite can be automatically plotted.
- The color code and the type of CI map defined by the user can be saved for future use as a template of the plotting map. Once the template is saved, next plotting of the same morphological map will not require definition of the color code. The map can be easily plotted by applying the existing template. By this way the martensite variants are indexed and the morphological maps of martensite can be automatically plotted.

The same method is used for plotting calculated pole figure in order to compare with the experimental one. The calculated pole figure can be plotted by creating a new “.ang” file from the file of scan data. That file will inherit the header lines with scanning parameter of the scan data. Twenty four calculated martensite variants are written in 24 rows with 10 parameters as required for the “.ang” file. While the three Euler angles represent the orientation of the martensite variant, the CI value indicates its variant number. Other necessary parameters are arbitrarily chosen. The new “.ang” file is readily opened in OIM for plotting the pole figure of any plane index. This pole figure represents the calculated 24 martensite variants, which can be used for comparison with the experimental one.

3.4.3. Misorientation map

It is clearly that the calculated (001) pole figure of martensite shows a pattern of separate points, while the experimental pole figure has a pattern of dense open rings and bars (Fig.3.1). The local variation of martensite orientations is the reason of this appearance of the pole figure. However, from the pole figure solely does not give any quantitative information about the local variation of martensite orientation. For this reason, we have introduced a new type of visual map, which called “misorientation map”. The map is plotted for the selected austenite grain, where each pixel is

represented by the misorientation between the measured martensite orientation and its corresponding calculated martensite variant (Fig.3.7c).

The misorientation map is plotted as follows:

- Using the calculated austenite orientation and OR for calculation of 24 martensite variants inherited from this austenite orientation.
- Finding the minimum misorientation between each measured orientation with one of calculated orientation and then replacing the CI index of this scan point by the value of minimum misorientation. By this way the misorientation of each scan point from the calculated orientation is recorded in the output file.
- The misorientation map is automatically plotted by the above described method.

The misorientation map is useful for visual expression of local variation of martensite within the austenite grain. The physical meaning of this map can be understood with an assumption of a constant OR. In previous section 3.3, it was confirmed that the variation of calculated ORs within an austenite grain is less than 0.5° . This variation is relatively small and the OR can be fixed as constant for the given steel. In that case, the variant misorientation of experimental martensite orientation has origin from the local rotation of austenite at this point from the average austenite grain orientation taken as the reference. According to Eq.(3.2), the misorientation matrix between k^{th} experimental point and its corresponding i^{th} calculated martensite orientation is:

$$\mathbf{M}_{i_{\text{standard}}}^{\text{bcc}} (\mathbf{M}_{k_{\text{experiment}}}^{\text{bcc}} \mathbf{C}_j)^{-1} \quad (3.7).$$

Following the Eq.(3.1), those martensite orientations can be expressed through the constant orientation relationship and the local austenite orientation as

$$\mathbf{M}_{i_{\text{standard}}}^{\text{bcc}} = (\mathbf{OR}_I^{\text{fcc-bcc}} \mathbf{C}_i) \mathbf{A}^{\text{fcc}}, \quad \mathbf{M}_{k_{\text{experiment}}}^{\text{bcc}} = (\mathbf{OR}_I^{\text{fcc-bcc}} \mathbf{C}_i) \mathbf{A}_k^{\text{fcc}} \quad (3.8)$$

where, $\mathbf{A}_k^{\text{fcc}}$ is the local orientation of austenite from which the k^{th} martensite orientation transformed. Replacing Eq.(3.8) into Eq.(3.7) we receive

$$\mathbf{M}_{i_{\text{standard}}}^{\text{bcc}} (\mathbf{M}_{k_{\text{experiment}}}^{\text{bcc}} \mathbf{C}_j)^{-1} = \mathbf{B} \left[\mathbf{A}^{\text{fcc}} (\mathbf{A}_k^{\text{fcc}} \mathbf{C}_j)^{-1} \right] \mathbf{B}^{-1} \quad (3.9)$$

where, $\mathbf{B} = (\mathbf{OR}_I^{\text{fcc-bcc}} \mathbf{C}_i)$.

From the Eq.(3.9), using the well-known property of the trace of matrix, that is

$\text{tr}(\mathbf{YXY}^{-1}) = \text{tr}(\mathbf{X})$ for any \mathbf{X}, \mathbf{Y} matrices, we receive

$$\text{tr}(\mathbf{M}_{i_{\text{standard}}}^{\text{bcc}} (\mathbf{M}_{k_{\text{experiment}}}^{\text{bcc}} \mathbf{C}_j)^{-1}) = \text{tr}\left\{\mathbf{B} \left[\mathbf{A}^{\text{fcc}} (\mathbf{A}_k^{\text{fcc}} \mathbf{C}_j)^{-1} \right] \mathbf{B}^{-1}\right\} = \text{tr}(\mathbf{A}^{\text{fcc}} (\mathbf{A}_k^{\text{fcc}} \mathbf{C}_j)^{-1})$$

or

$$\text{tr}(\mathbf{M}_{i_{\text{standard}}}^{\text{bcc}} (\mathbf{M}_{k_{\text{experiment}}}^{\text{bcc}} \mathbf{C}_j)^{-1}) = \text{tr}(\mathbf{A}^{\text{fcc}} (\mathbf{A}_k^{\text{fcc}} \mathbf{C}_j)^{-1}) \quad (3.10).$$

From Eq.(3.2) and Eq.(3.10) it is obviously that the misorientation angle between local martensite orientation and calculated one is equal to the misorientation angle between local austenite orientation of this point and the average grain orientation. By this way the local variation of austenite orientation in term of misorientation angle can be mapped. The application of this type of map will be shown in later example.

3.4.4 Example

Figure 3.7a shows the packet map of the part 4, which was cut from grain 1 as mentioned above. The martensite variants are classified and colored by red, yellow, green and blue by parallel relationship between $(011)_{\alpha'}$ and four variants of $(111)_{\gamma}$ close-packed plane (CP1 to CP4). Figure 3.7b represents sub-block (or variant) map of the same martensite region. The notation and orientation of 24 martensite variants from V1 to V24 were derived from Eq.3.1 using 24 conversion matrices \mathbf{C}_i given in Table 3.1.

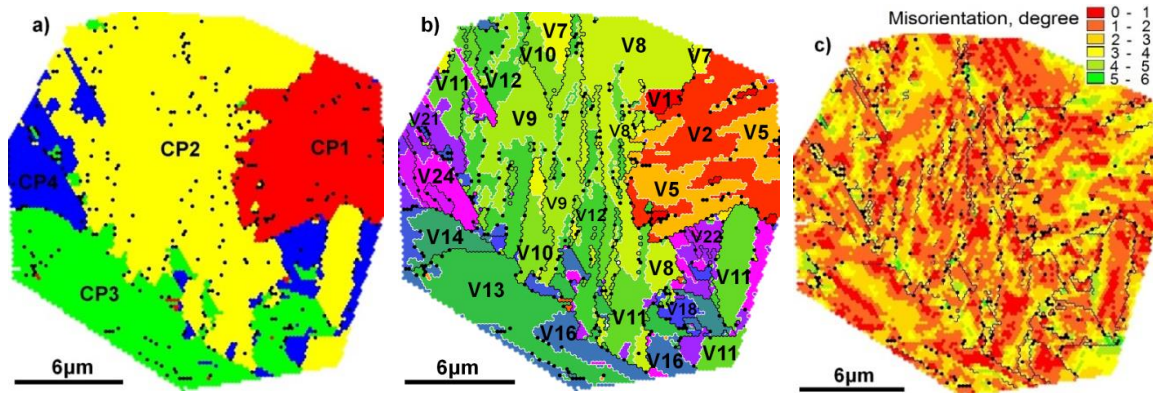


Figure 3.7. Visual plotting of morphological analyses for part 4 of grain 1: a – packet map showing packets of martensite colored by the same way as mentioned in Fig. 3; b – sub-block map showing 24 colored variants of martensite grouped into sub-blocks (the black and white lines showing boundaries with angle $\geq 15^\circ$ and $< 15^\circ$ respectively); c – misorientation map showing misorientation of experimental points from the closest calculated martensite variants.

The martensite variants are automatically indexed and highlighted by twenty four rainbow color codes from red to magenta. Low angle boundaries ($< 15^\circ$) between variants are shown in white color, while high angle boundaries ($\geq 15^\circ$) are in black color. The obtained sub-block map (Fig.3.7b) shows a typical morphology of low-carbon lath martensite [22,24], in which thin laths of the same martensite variant grouped together to form sub-blocks. Pairs of sub-blocks with low angle boundary such as V1-V4, V2-V5

and V3-V6, which belong to the same packet, gathered together to form three types of block. The high angle boundaries between blocks or packets are sharp and clear. The low angle boundaries between sub-blocks are often unclear, since orientation of martensite gradually changed during switching from one martensite variant to another across the sub-block boundaries.

The misorientation of experimental points from the closest calculated martensite variants is also plotted in Fig.3.7c. It shows that the misorientation distribution has a local characteristic. The points with misorientation smaller than 3° dominate with 0.84 fractions. The martensite areas with misorientation larger than 4° occupy only 0.04 fractions. These higher misorientation areas are often found near high angle boundaries (block or packet boundaries) as well as near inclusion particles [47]. The local high misorientation of scan points from calculated martensite variants might be caused by local deformation of austenite due to transformation strain.

3.5. Conclusion

An advanced fitting method has been developed for crystallographic and morphological analyses of lath martensite basing on EBSD data. The main results can be summarized as below:

1. The efficiency and precision of ordinary fitting method are improved by some advanced modifications of misorientation calculation and fitting procedure. The improved fitting method for EBSD data is capable for thorough crystallographic and morphological analyses of low-carbon lath martensite.

2. An advanced computational method for crystallographic and morphological analyses of martensite using EBSD data was developed. The method is designated for fast and precise calculation of austenite orientation and OR. This method also provides advantages for automatic variant indexing and visual plotting of martensite morphology.

3. Using coarse data with scanning step up to $1.6\mu\text{m}$ is an effective way to reduce calculation time without the risk of losing the precision. By this measure, a large number of prior austenite grains or a large grain can be effectively analyzed within reasonable time.

4. When a sufficient part of a prior austenite grain was used for analyzed the tolerance of obtained orientation relationship is within 0.2° , while tolerance for fitting austenite orientation is within 0.5° . The obtained orientation relationship is almost constant for the given steel regardless the location on the sample of EBSD data set. The fitted orientation relationship for C10Mn30 steel is close to G-T type with $(111)_\gamma$ deviated 1.72° from $(011)_\alpha$ and $[\bar{1}01]_\gamma$ deviated 2.63° from $[\bar{1}\bar{1}1]_\alpha$. Austenite orientation is found to be locally changed within a prior austenite grain due to transformation strain, whereas the orientation relationship is almost unchanged.

Reference

- 1) Zhou, Weilie; Wang, Zhong Lin (ed.): Springer (2007) pp.522.
- 2) A.J. Schwartz, M. Kumar, B.L. Adams, D. Field (ed.): Springer (2009) pp. 403.
- 3) B.L. Adams, S.I. Wright, K. Kunze: Metall. Trans.A **24** (1993) 819-831.

- 4) J. Alkorta: Ultramicroscopy **131** (2013) 33-38.
- 5) F. Barcelo, Y. Carlan, J.L. Béchade, B. Fournier: Phase Trans. **82** (2009) 808-820
- 6) Y. Chen, J. Hjelen, S.S. Gireesh, H.J. Roven: Microsc. **245**, No.2 (2012) 111-118.
- 7) D. Dingley : Microsc. **213** (2004) 214-224.
- 8) T. Furuhashi, H. Kawata, S. Morito, T. Maki: Mater. Sci. Eng.A **431** (2006) 228–236.
- 9) T. Furuhashi, K. Kikumoto, H. Saito, T. Sekine, T. Ogawa, S. Morito, T. Maki: ISIJ Int. **48** (2008) 1038–1045.
- 10) A.F. Gourgues, H.M. Flower, T.C. Lindley: Mater. Sci. Tech. **16** (2000) 26-40.
- 11) A. F. Gourgues-Lorenzon: Int. Mater. Rev. **52**, No.2 (2007), 65-128.
- 12) A. F. Gourgues-Lorenzon: Microsc. **233**, No.3 (2009) 460–473.
- 13) Z. Guo, C.S. Lee, J.W. Morris Jr.: Acta Mater.**52** (2004) 5511-5518.
- 14) P. Haušild, V. Davydov, J. Drahoš, M. Landa, P. Pilvin: Mater. Design **31**, No.4 (2010) 1821-1827.
- 15) J. Hjelen, R. Orsund, E. Hoel, P. Runde, T. Furu, E. Nes: Text. Microstr. **20** (1993) 29-40.
- 16) F.J Humphreys: Scripta Mater.**51**, No.8, (2004) 771-776.
- 17) M. Kamaya: Ultramicroscopy **111**, No.8 (2011) 1189-1199.
- 18) M. Karlsen, J. Hjelen, Grong, G. Rrvik, R. Chiron, U. Schubert, E. Nilsen: Mater. Sci. Tech. **24**, No.1 (2007) 64-72.
- 19) H. Kitahara, R. Ueji, M. Ueda, N. Tsuji, Y. Minamino: Mater. Charac. **54** (2005) 378– 386.
- 20) H. Kitahara, R. Ueji, N. Tsuji, Y. Minamino: Acta Mater.**54**, No.5 (2006) 1279-1288.
- 21) I. Lischewski, G. Gottstein: Acta Mater.**59**, No.4 (2011) 1530-1541.
- 22) S. Morito, H. Tanaka, R. Konishi, T. Furuhashi, T. Maki: Acta Mater.**51** (2003) 1789-1799.
- 23) S. Morito, H. Saito, T. Ogawa, T. Furuhashi, T. Maki: ISIJ Int.**45** (2005) 91-94.
- 24) S. Morito, H. Yoshida, T. Maki, X. Huang: Mater. Sci. Eng.A **438–440** (2006) 237-240.
- 25) S. Morito, X. Huang, T. Furuhashi, T. Maki, N. Hansen: Acta Mater.**54** (2006) 5323-5331.
- 26) S. Morito, Y. Adachi, T. Ohba: Mater. Trans. **50**, No.8 (2009) 1919-1923.

- 27) S. Morito, R. Igarashi, K. Kamiya, T. Ohba, T. Maki: Mater. Sci. Forum **638 - 642** (2010)1459-1463.
- 28) J.W. Morris: ISIJ Int.**51** (2011) 1569-1575.
- 29) J.W. Morris Jr, C. Kinney, K. Pytlewski, Y. Adachi: Sci. Technol. Adv. Mater.**14** No.1 (2013) 208-216.
- 30) N. Nakada, T. Tsuchiyama, S. Takaki, S. Hashizume: ISIJ Int.**47**, No.10 (2007) 1527-1532.
- 31) V. Randle: Mater. Sci. **44**, No.16 (2009) 4211-4218.
- 32) D.J. Rowenhorst, A. Gupta, C.R. Feng, G. Spanos: Scripta Mater. **55** (2006) 11-16.
- 33) A. Shibata, S. Morito, T. Furuha, T. Maki: Scripta Mater. **53** (2005) 597-602.
- 34) B. Sonderegger, S. Mitsche, H. Cerjak: Mater. Charac. **58** (2007) 874-882.
- 35) D.W. Suh, J.H. Kang, K.H. Oh, H.C. Lee: Scripta Mater. **46** (2002) 375-378.
- 36) S. Zaefferer, S.I. Wright, D. Raabe : Metall. Mater. Trans.A **39** (2008) 374-389.
- 37) A.B. Greninger, A.R. Troiano: Metals Trans.**185** (1949) 590-598.
- 38) G.V. Kurdjumov, G. Sachs: Z. Physik **64** (1930) 324-326.
- 39) Y. Meng, X.F. Gu, W.Z. Zhang: Acta Mater.**58** (2010) 2364-2375.
- 40) G. Miyamoto, N. Takayama, T. Furuha: Scripta Mater.**60** (2009) 1113-1116.
- 41) Z. Nishiyama: Sci. Rep. Tohoku Univ.**23** (1934) 637-664.
- 42) V. Ocelík, I. Furár, J.Th.M. De Hosson: Acta Mater.**58** (2010) 6763-6772.
- 43) G. Wassermann: Mitt K-W-I Eisenforsch **17** (1935) 149-158.
- 44) W.Z. Zhang, G.C. Weatherly: Scripta Mater. **37**, No.10 (1997) 1569-1574.
- 45) E. C. Bain:Trans. AIME **70** (1924) 25-46.
- 46) J. S. Bowles, C. M. Wayman: Metall. Trans. **3**, No.5 (1972) 1113-1121.
- 47) H.A. Pham, T. Ohba, S. Morito, T. Hayashi, T. Furuha, G. Miyamoto: Mater. Sci. Forum **738 – 739** (2013) 25-30.
- 48) P.M. Kelly, A. Jostsons and R.G. Blake: Acta Metall. Mater.**38** (1990) 1075-1081.

Chapter 4

The nature of prior-austenite microstructure formation

4.1. Introduction

The microstructure of prior-austenite is an important object to be controlled in order to archive high mechanical and functional properties of martensitic steels [1-15]. Prior-austenite (hereafter, austenite) grain boundary responses to inter-granular fracture or hydrogen embrittlement [4-5], while grain size responses to microstructure of finally transformed product, hence its tensile strength and toughness [1-3, 7-15]. An effective experimental technique for direct investigation of prior-austenite microstructure in steels is currently unavailable, since the austenite forms at relatively high temperature, and it degrades on subsequent cooling to room temperature. For a long time, the only method to evaluate prior-austenite grain size is grain boundary selective etching for observation under optical microscope [16-22].

Recently, the prior-austenite grain shape and/or prior-austenite orientation can be reconstructed from martensite orientations acquired by electron backscatter diffraction (EBSD) technique [23-28]. The detailed features of reported methods for reconstruction of austenite microstructure has been reviewed in chapter 1. However most of the researchers have focused only on the size of prior-austenite grain or local orientation within one austenite grain, rather than on the prior-austenite microstructure. The term “prior-austenite microstructure” was introduced by present author to indicate the reconstructed microstructure of austenite from a selected area of product phase, which comprises averaged austenite grain orientations, grain shape and grain boundary characteristics.

In our recent study, the microstructure of austenite can be precisely reconstructed from martensite by EBSD technique in combination with our new orientation fitting method. We have been successfully reconstructed prior-austenite microstructure from martensite of high carbon steels for an observation area of $100 \times 100 \mu\text{m}^2$. The microstructure revealed large portion of twin sub-boundaries $\Sigma 3$, from 0.4 to 0.6 length fractions, which have not been previously reported. The twin sub-boundaries effectively refine the grain size of austenite, since they show high resistance to grain growth. The twin-related austenite orientations are probably selected during reverse transformation to austenite or during subsequent stage of grain growth. However, the mechanism of twinning selection is not well understood. Under the present circumstances, it is important to study crystallographically the nature of microstructure formation of austenite during reverse transformation in order to effectively control the microstructure and properties of martensitic steels.

4.2. Experimental

For this study, three plain carbon steels C40, C60, C80 (Table 2.1), a newly prepared knife J90 (table 2.2) and a modern Japanese sword with unknown composition were used. Initial microstructure of C40 and C60 is ferrite (F) + pearlite (P), with the fraction of ferrite decrease as the carbon content increases. These steels were used for study the

formation of austenite microstructure from a mixture of F + P. C80 has a full pearlitic microstructure with fine cementite lamellae. The formation of austenite from full pearlitic microstructure will be studied for this steel. The J90 and the sword were also used for study on thermal mechanical effect of the traditional method for preparing Japanese sword on formation of austenite microstructure.

The 2mm thin specimens of plain carbon steels were heated in a salt bath, at 1073K for 0.6ks followed by a fast quench in water or iced brine. For C60 and C80 specimens, water quench was sufficient for fully martensitic transformation. For C40 with austenitizing at 1073K, a dual-phase mixture of M+F was formed after iced-brine quench. All the specimens were cut at cross section, and the obtained surface was polished by the typical procedure described in chapter 2. The SEM/EBSD measurement was performed with typical setting parameters given in 2.2.3. For the J90 and the sword, the observation areas were selected near the sharp edge. An area of $100 \times 100 \mu\text{m}^2$ was selected from scanned data of each specimen for reconstruction of prior-austenite microstructure.

4.3. Reconstruction method

4.3.1. Main steps of austenite reconstruction method

The reconstruction of prior-austenite orientation from martensite comprises of four main stages:

- a) Manual selection of martensite area inherited from one austenite orientation;
- b) Fitting austenite orientation from selected martensite orientations;
- c) Indexing the martensite by the fitted austenite orientations;
- d) Manual correcting the prior-austenite grain boundaries by using other information of martensite microstructure.

Each stage of reconstruction will be explained with more details.

a) Manual selection of martensite area inherited from one austenite orientation

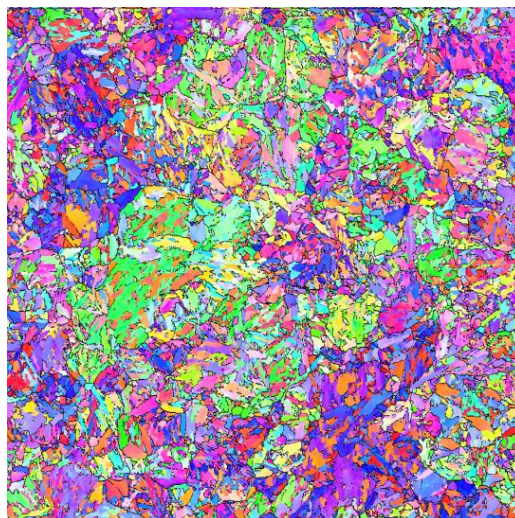


Figure 4.1. *The inverse pole figure (IP) map of EBSD data taken for martensite.*

This stage is the most time consuming in the present method for reconstruction of austenite orientation. The selection is assisted by using inverse pole figure (IP) map of martensite orientation (Fig.4.1). This IP map is automatically plotted in commercial OIM program by coloring each pixel according to the alignment of its crystal direction with the specified sample direction. In this map, the martensite area, which shows a similar pattern of martensite grain colors, is often related to one austenite orientation. Such martensite area is selected and cropped to create a new data list. Then a $(001)_\alpha'$ pole figure will be plotted for the selected data. By verifying the unique pattern of the pole figure, which is specific for martensite variants inherited from one austenite orientation (Fig.4.4), the spare martensite orientations will be deleted. By this way a selection of martensite variant inherited from one austenite orientation is refined. The selection can be done for most of large austenite grain in the observed area, while the remained small grains are difficult to be identified. Those grained will be selected in later steps.

b) Fitting austenite orientation

The selected martensite orientations are used for calculation of martensite orientation by using the fitting program described in chapter 3. The fine fitting procedure is applied for all of the data with fitting step of 0.2° . Initially, if the OR is unknown for the given steel, the ORs are also fitted for several selected grains. An average OR from those fitted ORs will be used for further fitting of other selected grains. After fitting all of possibly selected grains, a list of reconstructed austenite orientations for the observation area is obtained.

c) Indexing the martensite by the fitted austenite orientations

In this step, a program is used to index the martensite orientations by a list of calculated austenite orientations. The program will read in succession each austenite orientation in the list, which is obtained from the previous step. By using the average OR, all 24 possible martensite variants inherited from this austenite orientation will be calculated. Each experimental martensite orientation will be compared with the calculated martensite variants. If its deviation from one of calculated martensite variants smaller than a given small tolerance angle, the martensite orientation will be indexed according to the number of austenite orientation in the list and the deviation will be recorded. The method of indexing martensite orientations by modifying the EBSD data for re-opening in commercial OIM program has been described in chapter 3. The tolerance angle is chosen as 5° in this study. The indexing process will be repeated for all of austenite orientation in the list. When the deviation of a given martensite orientation from calculated martensite variants of a new austenite orientation is smaller than that of a preceding one, this martensite orientation will be re-indexed by the new austenite orientation, and the existing deviation value will be replaced by the new one. When the process is completed, all of experimental martensite orientations, which have OR with austenite orientations in the list will be indexed by the number of corresponding austenite orientation. Part of martensite orientations remained un-indexed, if they have OR with other austenite orientations which are not included in the list. The

indexed martensite orientations can be colored by the number of austenite orientations as shown in Fig.4.2. This highlighted map will be used to select the non-indexed austenite grain to calculate its orientation. The newly calculated austenite orientation will be added to the list for the next iterative indexing. The process is iterative until all of martensite orientations in observation area are indexed. There was such case that the remained non-indexed areas are too small with insufficient number of martensite variants required for precise calculation of austenite orientation. Those areas are considered to relate to the austenite orientations, which are unable to be found by present method (Fig.4.17).

d) Manual correcting the prior-austenite grain boundaries

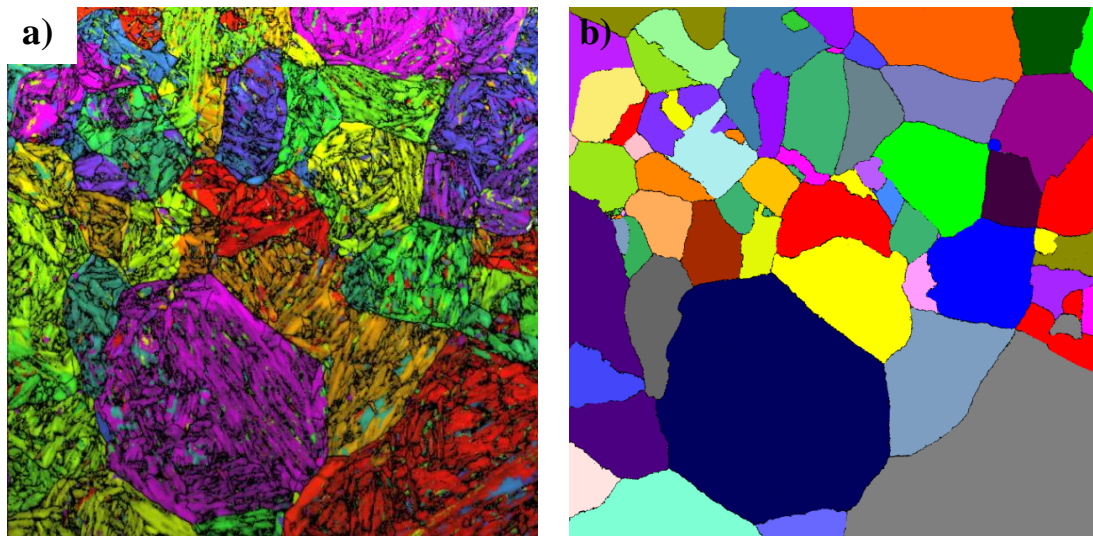


Figure 4.2. *The martensite orientations highlighted by austenite grain orientations (a), the grain map after manual correction (b).*

Figure 4.2a shows martensite orientations highlighted by 54 austenite orientations for a $100 \times 100 \mu\text{m}^2$ observation area of C80 steel. In the indexing step, the martensite orientation is indexed by the number of austenite orientation, from whom it bears a chosen OR with minimum deviation. Unfortunately, the martensite orientations within one austenite grain are often deviated from standard variants of the OR due to local rotation of the austenite and/or martensite crystals. Those deviations lead to a certain amount of “ambiguous” martensite regions, which are colored by other colors than the potential austenite grain containing those regions (Fig.4.2a). The assumption on the continuity of austenite grain and the clarity of grain boundaries are added in order to manually avoid the ambiguous regions. The continuity of austenite grain implies that the austenite grain on a reconstructed map is defined as a continued region of unique color. The later implies that the austenite grain is separated from its surrounding grains by clearly defined grain boundaries (Fig.4.2b). Those two assumptions were confirmed in identification of neighbor austenite grain with random boundaries. However, they do not work in some cases, when two neighbor austenite grains have a $\Sigma 3$ twin relationship. This problem is also described by Germain et. al [3] and the reason has been mentioned in chapter 1. For such case of twin boundary, the ambiguous martensite regions are the

common martensite variants of both twin-related orientations. For such cases, the twin boundaries are corrected by combining the grain indexed map with the IQ map of martensite orientation [3], which shows the information of martensite boundaries. The component of austenite twin boundary is taken from martensite boundaries in such “ambiguous” regions with concerning about the direction of twinning plane between two austenite grains.

e) Plotting austenite microstructure features

For characterization of the prior austenite microstructure, it is necessary to modify the EBSD data of martensite in order to represent the austenite orientation. The original EBSD data comprise only information of martensite orientation. However, this EBSD data can be modified to show the features of austenite microstructure. The modification procedure is similar to that for indexing martensite orientation described in chapter 3. Initially, the martensite orientation will be indexed by the ordinal number of the most representative austenite orientation, which is calculated by the above mentioned method. Subsequently, the martensite orientation will be replaced by the most representative austenite orientation. By this way, the modified EBSD data will contains crystallographic information of austenite grain orientation, while the other parameters of all scan points remain unchanged.

The modified EBSD data is compatible with commercial OIM program. Analyzing this data in the OIM program, several features of austenite microstructure are obtained such as austenite grain map (Fig.2b), austenite grain boundary characteristic (Fig.4.7b) and twin-related grain map (Fig4.9). To plot the grain map, the austenite orientations are colored either by a custom or by an automated color code according to their number in the list. For grain boundary characteristics map, the grain boundaries are classified into $\Sigma 1$ – low angle boundary with blue color, $\Sigma 3^n$ ($n=1-3$) - twin boundary with red color, other coincident site lattice (CSL) boundaries in green and lastly the randomly high angle boundary with black color. In this study we used Brandon criterion for determination of CSL boundaries [29-30]. This criterion implies that a grain boundary is considered to be a coincident site lattice type Σ if the deviation from the exact coincidence relationship θ (measured in degrees) sanctifies the following condition:

$$\theta < \frac{15^\circ}{\sqrt{\Sigma}}$$

A new measure for quantifying the austenite orientation was introduced in this study. That is the twin-related grain map. In this map, the neighbor austenite orientations with $\Sigma 3^n$ ($n=1-3$) twin relationship are painted by the same color (Fig.4.9).

4.3.2. Main features of the reconstruction method

a) Precise reconstruction of prior-austenite microstructure

When the austenite orientation and OR are precisely calculated, the austenite microstructure can also be precisely reconstructed. The below example demonstrates that several neighbor prior-austenite grains with close orientation can be clearly

identified by the present method. Fig.4.3a shows an area of martensite, which was colored in red color by using one austenite orientation with tolerance angle 10° . That austenite orientation was calculated by using a part of martensites from this highlighted area. Since the boundaries of this area are clear and sharp, it is likely that the area is transform from only one given austenite orientation. However the corresponding (001) pole figure (Fig.4.3b) has a strange appearance, which indicates that the martensite orientations are varied in a larger scale than in normal austenite grain. To visualize the variation of martensite orientation, the new misorientation map is plotted for the martensite area using the given austenite orientation (Chapter 3). The result is shown in Fig.4.4a, where each pixel is colored by its misorientation from calculated martensite variant with the inserted color key. The (001) pole figure is also colored by the same way, where its pole of martensite is painted by its color on the misorientation map (Fig.4.4b). Now, it is clear that there are at least three austenite orientations with small misorientation within the above highlighted martensite area. The two sub-areas of martensite which show large misorientation on the map are used for calculation of their austenite orientations. The mutual misorientations between three obtained austenite orientations are given in table 4.1, where the austenite orientations are noted as G1-G3. The martensite area is re-indexed by using three austenite orientations and the result is plotted in Fig.4.5, where each grain and its corresponding (001) pole figure was colored in red, yellow and green. The misorientation map plotted for the 3 austenite orientations showing a typically small variation of martensite orientation (Fig.4.5c). This example demonstrates the delicate way for precise reconstruction of austenite orientation even for the case, that neighbor austenite grains have small misorientation.

When the austenite orientation is reconstructed with high precision, it is expected that the other features of austenite microstructure like grain boundaries features and twin-related grain map can be also precisely reconstructed.

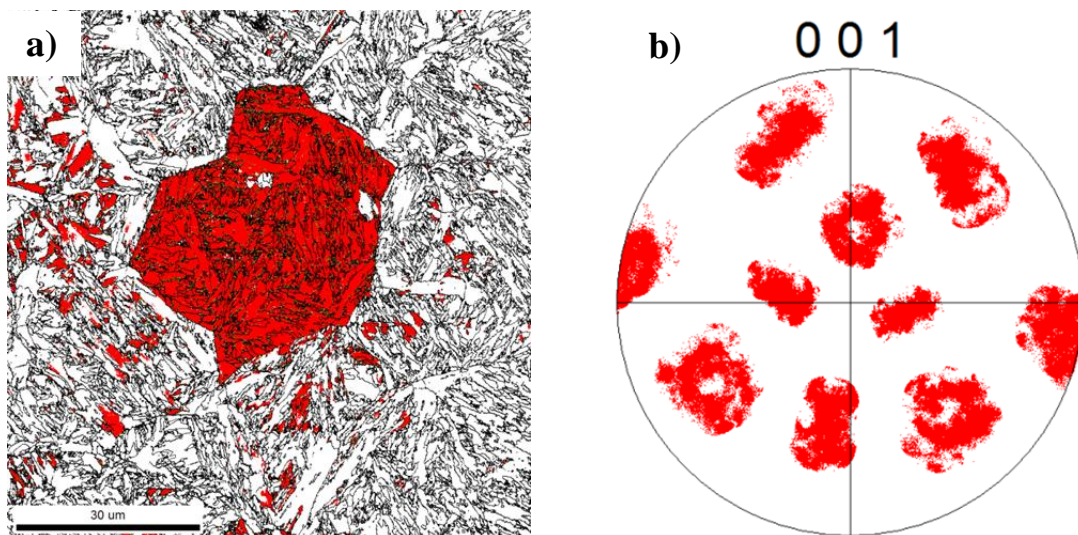


Figure 4.3. The martensite area highlighted in red color by using one austenite orientation (a) and its (001) pole figure (b).

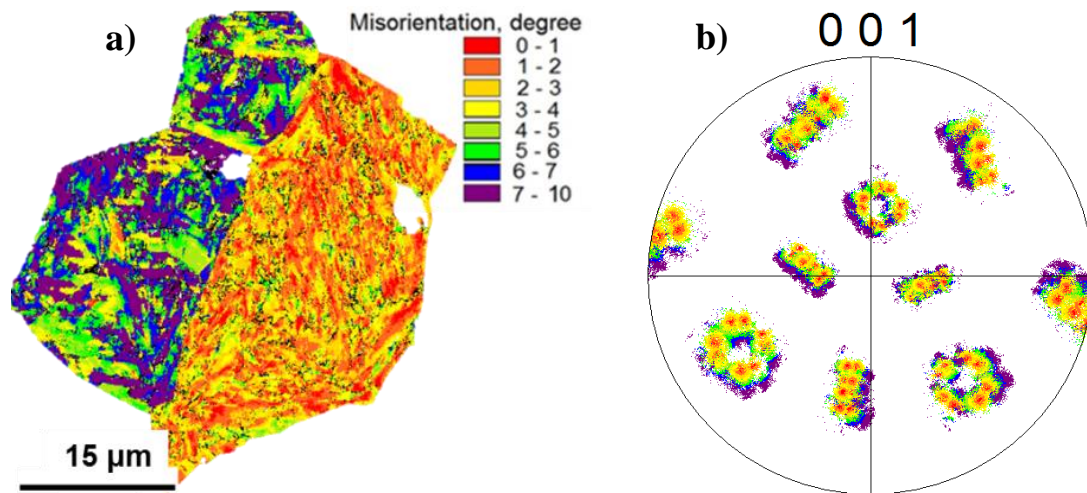


Figure 4.4. The misorientation map plot for the selected area in Fig.4.3 with inserted color key showing clearly three grain with close orientation (a), the (001) pole figure is highlighted by the same color code of the misorientation map (b).

Table 4.1. The mutual misorientation between the three austenite grains ρ

	G1	G2	G3
G1		6.68	6.46
G2	6.68		7.61
G3	6.46	7.61	

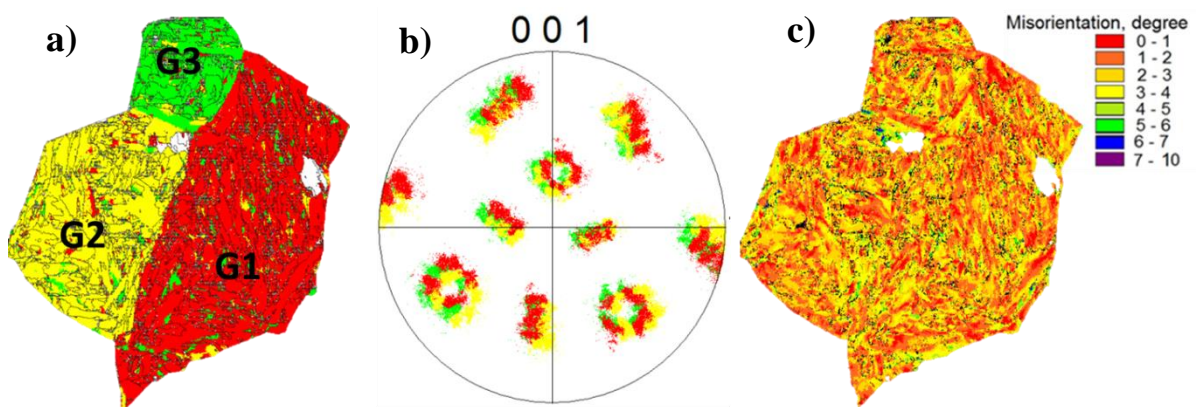


Figure 4.5. The same area in Fig.4.4 is colored by three austenite orientations (a), the corresponding (001) pole figure highlighted by the same way (b), the misorientation map is plotted for three austenite orientation (c).

b) Disadvantage and future improvement

While the method allows precise reconstruction of the microstructure, its main disadvantage is time consuming. It takes about 20 working hours for reconstruction of prior-austenite microstructure for an area of $100 \times 100 \mu\text{m}^2$, which contains about 60 austenite orientations. The most time consuming step is manual selection of martensite areas inherited from one austenite grain for calculation of their corresponding austenite orientations. There are several promising ways to make this process become more effective by reducing the amount of manual work. The future improvement of the present method is in progress.

4.4. Reconstruction result and discussion

4.4.1. Prior-austenite microstructure in high-carbon steels

The austenite (A) microstructure of three carbon steels C40, C60 and C80 were reconstructed from martensite. The initial microstructure of C40 and C60 is pearlite + ferrite (P+F), while that of C80 is full pearlitic with fine cementite lamellae (Fig.4.6). The reported studies on reversion of austenite from P+F mixture show that during heating, the austenite is firstly reversed from pearlite region, later the ferrite is dissolved into the austenite with the kinetics controlled by carbon diffusion [31-34]. When the heating rate is relatively high (20K/s), the reverse transformation of A from P happens in two steps. Firstly, the pearlitic ferrite (PF) within one pearlite nodule transforms into austenite, subsequently, the cementite lamellae will be dissolved into the newly transformed austenite. In previous studies on reverse transformation, there has not been any solid evidence of orientation relationship between pearlitic ferrite and reversed austenite reported [35-36]. However, the K-S or near K-S orientation relationship between the austenite and adjacent ferrites in case of P+F \rightarrow A transformation sometimes were observed [37-38]. Nevertheless, the formation of austenite microstructure from P or P+F so far has not been clearly understood. The main reason is absence of an effective method, which is necessary for quantitative characterization of austenite microstructure.

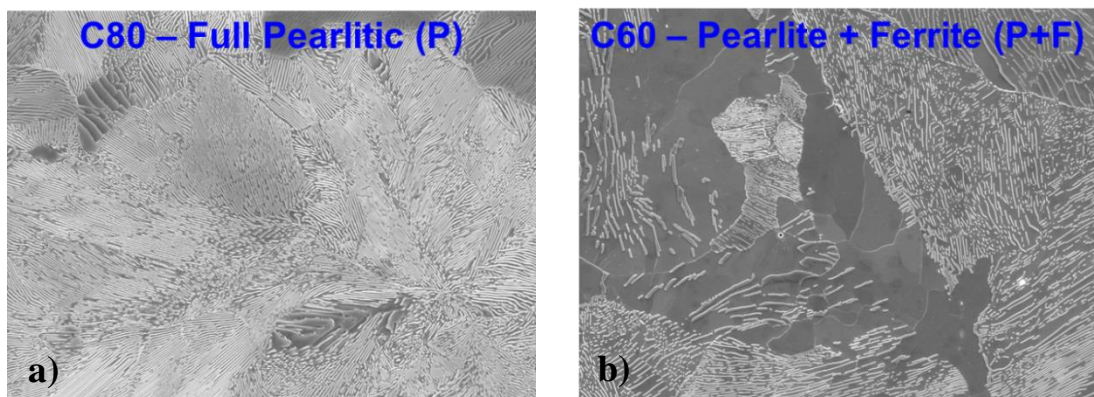


Figure 4.6. The SEM micrographs of initial microstructure of C60 (a) and C80 (b).

The first approach for study reversed austenite is interrupted austenitizing [37-38], which comprises of heating the sample to austenitizing temperature with relatively short holding time for partial reversion to austenite in form of isolated islands within P or P+F matrix. The following rapid quenching is applied to allow those austenite islands transform to martensite. The isolated martensite islands are used for calculation of austenite orientations. The ORs were checked for those obtained austenite orientations and their adjacent ferrite. Although this approach can reveal some aspect in kinetics of reverse transformation, it is insufficient for study the formation of austenite microstructure due to the incomplete reverse transformation.

The second approach includes in using high alloy steel, for which a certain amount of retained austenite exists in final microstructure after quenching to room temperature [35-36,39]. The crystallography of the retained austenite was analyzed by the same way used in the first approach. This approach is capable for direct analyses of austenite/ferrite orientation relationship. However the effect of high content of alloying elements on formation of austenite is of great concern. Both the existing approaches are not capable for obtaining information of full austenite microstructure.

Using the above described reconstruction method the full austenite microstructures of the three carbon steels were reconstructed. Each microstructure contains the average austenite grain orientation, grain shape and grain boundary characteristics. The orientation relationship between neighbor austenite grains is also analyzed. The obtained austenite microstructures in these steels are studied quantitatively in order to understand their nature of formation and evaluation during reverse transformation from P+F or P initial microstructures.

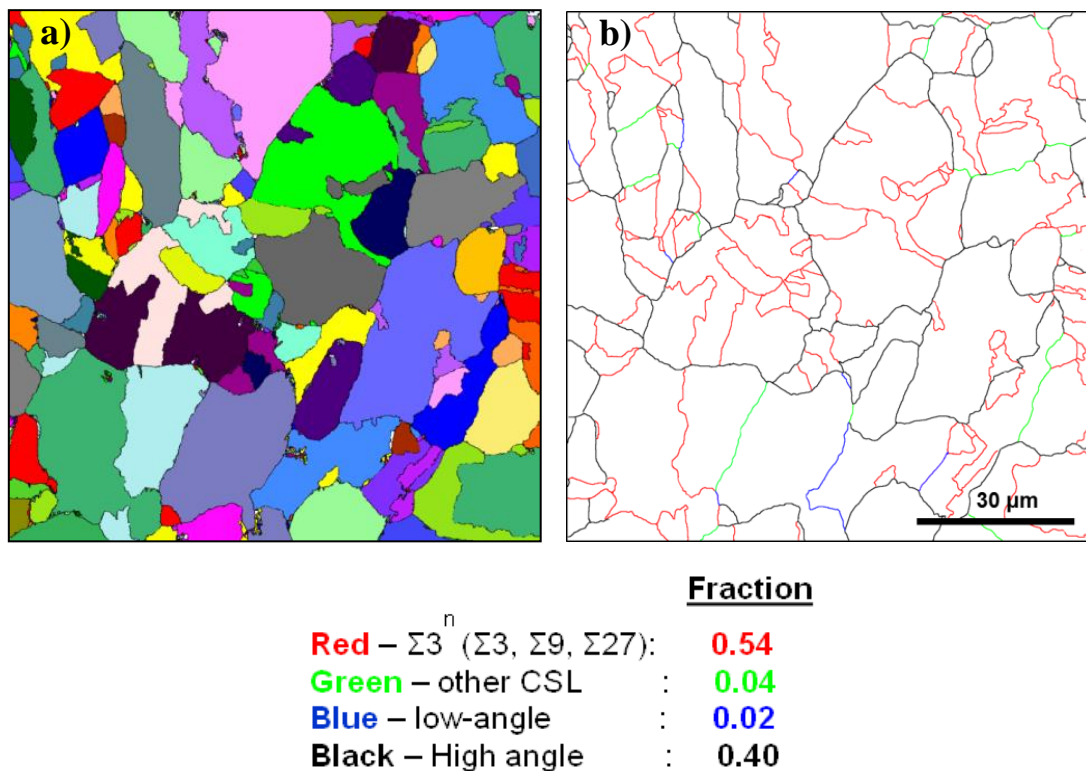


Figure 4.7. Reconstructed austenite grain map (a), grain boundary map (b) of C60.

Figure 4.7 represents the reconstructed austenite grain map for C60 steel. There are 165 (number) austenite orientations, which are highlighted by random colors in this map. The map solely shows an inhomogeneous microstructure of austenite with abnormal grain shape. However, the boundary map reveals details of boundary characteristics with high fraction of twin sub-boundaries up to 0.54, which are in red color (Fig.4.7b). This fraction of twinning boundary in C60 steel is abnormal, since it is significantly higher than the value, which is observed in nickel alloys or austenitic stainless with similar FCC lattice. For the later, the nominal fraction of twin boundary is around 0.45 [41-42,46]. The twin boundaries observed in nickel or austenitic steel are dominantly annealing twin with straight or ledge-like shape, although some bugling twin boundaries were observed while the nucleation of new grain takes place at a twin boundary [43-44].

The twin boundaries in C60 have irregular shapes that are close to bugling boundaries than to straight annealing twin boundaries. The error in determination of twin boundaries during reconstruction due to the ambiguous region between twin-related grains may be a reason of such appearance of reconstructed twin boundaries as discussed above. However, the difference in the nature of microstructure formation between austenitic steel and carbon steel should also be taken into account. For nickel or austenitic steel, there is not any phase transformation happens during their heating to high temperature or during cooling to ambient temperature. The evolution of austenite microstructure in these alloys is mainly controlled by recrystallization [41-42]. For carbon steel, the heating to high temperature always invokes phase transformation from P+F mixture to A before any recrystallization process takes place. The irregular shape of twin boundary in C60 steel may be the result of reverse transformation rather than annealing twin formation.

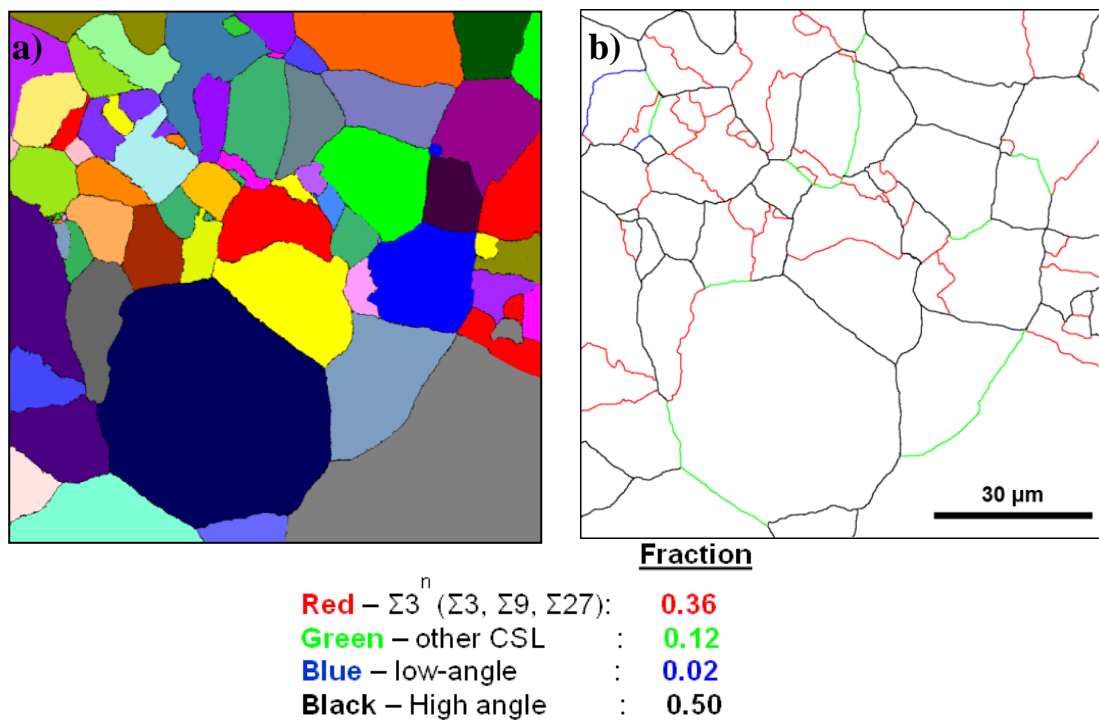


Figure 4.8. Reconstructed austenite grain map (a), grain boundary map (b) of C80.

Fig.4.9a and Fig.4.9b show the twin-related grain maps of C60 and C80 respectively. In this map, neighbor austenite grains with twin relationship (including $\Sigma 1$ low-angle misorientation) according to Brandon criterion are filled by the same color. The map revealed an interesting morphology of prior-austenite microstructure, in which a group of twin-related grains forms a coarser grain-like structure. This structure resembles the shape of pearlite nodule of these steels (Fig.4.12). While the number of austenite orientations in C60 steel is larger than that in C80 steel, the twin-related map reveals a coarser assemble of twin grains in C60. It is likely that a twinning selection rule or annealing twin formation dominates the reverse transformation, when a coarse pearlite nodule transforms into a group of twin-related austenite grains.

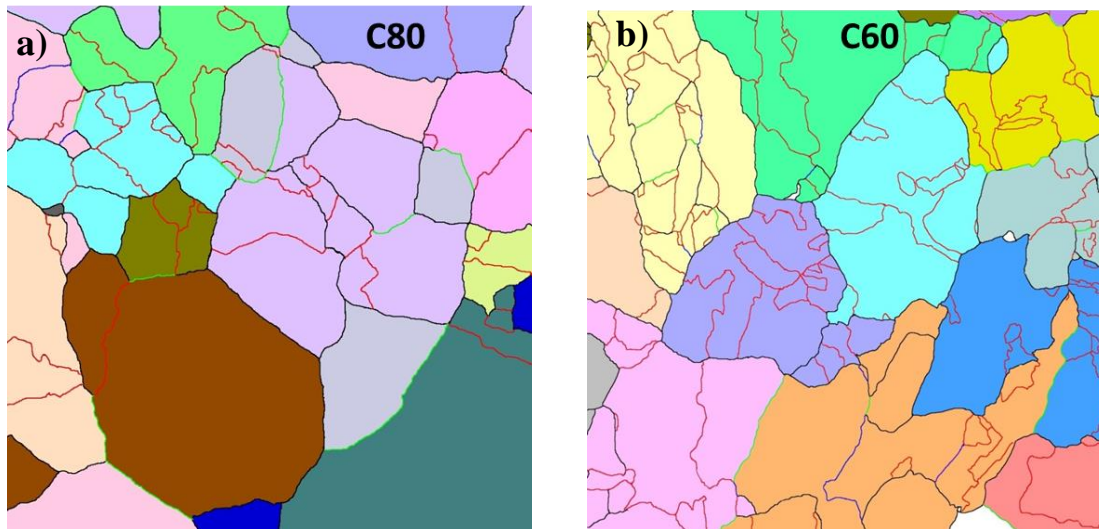


Figure 4.9. *Twin-related grain map showing grains with twin orientation relationship for reconstructed austenite microstructure of C60 (a) and C80 (b).*

A group of twin-related grains in the map was selected for analysis on twin relationship (Fig.4.10). In case of C60, the group comprises 9 austenite orientations (Fig.4.10a). The twin tree of this group reveals that the orientation 1 was decomposed into 9 twin-related orientations by multiple-twinning sequence. For C80, both multiple twinning and low-angle boundary divisions were observed (Fig.4.10b). The orientation 1 was also decomposed into 9 twin-related orientations, but the fraction of twin boundaries is remarkably smaller. The twin relationship is rather complicated. Grain 9 does not have connectivity with grain 4, with whom it has a twin relationship. The grain 9 is also isolated with other grain in the group by randomly high angle boundaries.

The deviation of each boundary in the twin related group, from correct twin type was calculated for both steels (Fig.4.11). It is well known that the annealing twin boundary in FCC alloys is often observed as clearly straight line with misorientation close to $60^\circ/[111]_\gamma$. If the small deviation is taken as the only criterion of annealing twin, the twin boundaries with deviation less than 1.0° can be referred to annealing twin, although they have irregular shape. In addition to irregular shape, some twin boundaries in C60 and many those boundaries in C80 have large deviation from exact twinning misorientation. Moreover, for FCC metals, a moderate level of strain is required to

evoke recrystallization for annealing twin formation [45-46]. The strain level of reverse transformation to austenite might be insufficient for the domination of annealing twin in austenite microstructure of both steels.

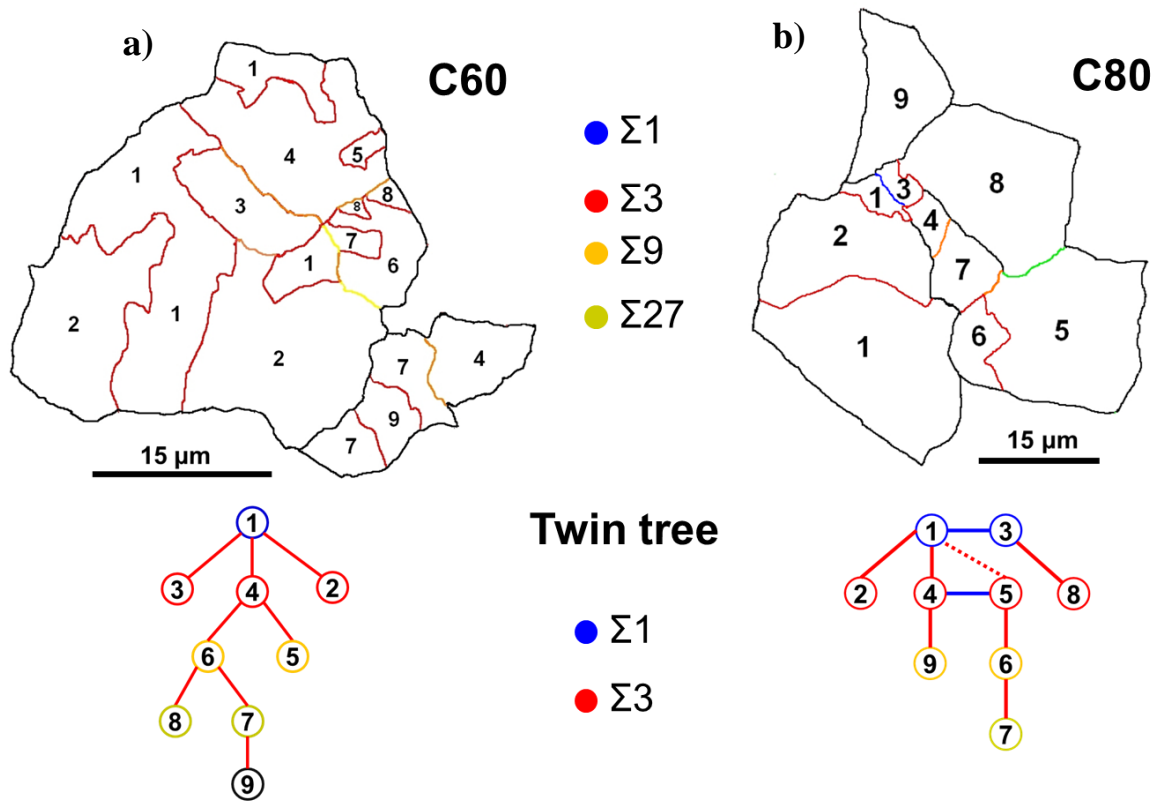


Figure. 4.10. A group of twin-related grains with twin tree showing the twin relationship.

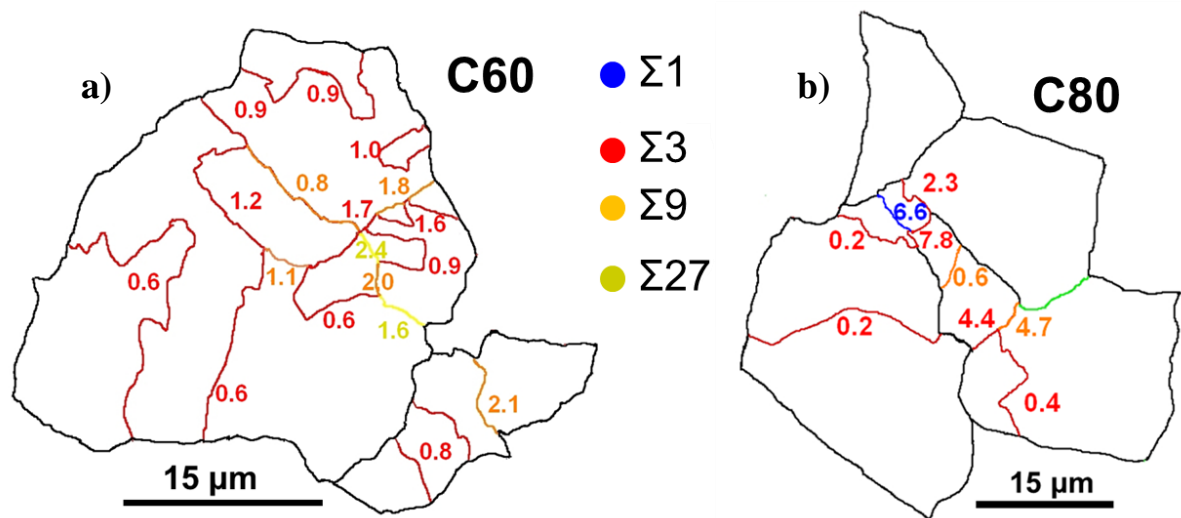


Figure 4.11. The deviation of each boundary from exact twin expressed in degree, the inserted color key showing different types of twin boundaries.

It is likely that a group of twin-related grains is formed due to some restrictions on austenite orientations during reversion from a single PF grain. For sake of clarity, we will discuss these restrictions separately for C80 and C60 steels. For C80 steel, the austenite is reversed from a fully pearlitic microstructure. It has been reported that the nucleation site of A from P is either cementite/ferrite boundary or triple junction of PF grains [35-38]. In C60 steel the reverse transformation of austenite from P with presence of F may happen in different manner. For this kind of transformation, although A is firstly reversed from PF, the nucleation of A at boundaries with F is observed [37]. On one hand, the presence of F provides more nucleation site for A nucleation. On the other hand, it may cause more restrictions on the choice of austenite orientation.

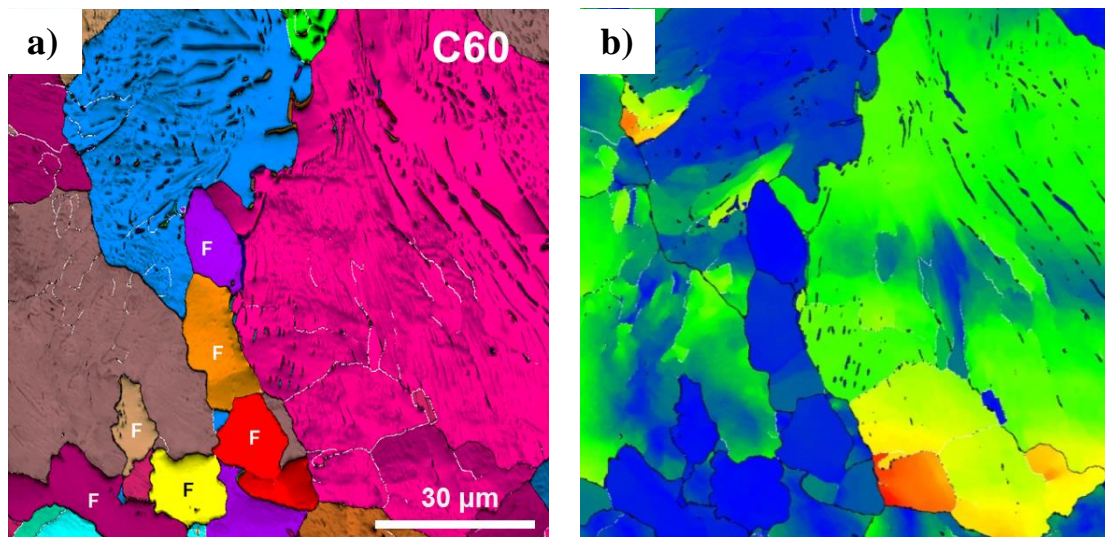


Figure 4.12. The PF grain map (a) and grain reference orientation deviation map (b) of C60 steel.

The EBSD measurement was accomplished for investigation of initial microstructure in both steels. Since the cementite lamellae are very thin, they were not able to be indexed in normal EBSD mode. Nevertheless, the PF orientations and F orientation in C60 were well indexed and the initial microstructure of two steels in term of PF grains can be characterized. Fig.4.12a and Fig.4.12b represent the grain map and grain reference orientation deviation map of C60 respectively. Fig.4.13a and 4.13b represent the same maps of C80. In grain map, the grains of PF and F, which were determined by single PF orientation with a tolerance of 5° , are highlighted by an automated color code. The ferrite grains in C60 are noted with symbol F. In grain reference orientation deviation map, each pixel within one grain is colored by its misorientation from the average orientation of this grain. In the SEM image (Fig.4.6a) the observed pearlite nodules are not very coarse in C60 steel, but the EBSD grain map shows a very coarse PF grains. The ferrite grains are finer and they appear in group with homogeneous grain orientation spread. The orientations are inhomogeneous within a PF grain. Some locations at triple junction show higher misorientation from average grain orientation, and some low-angle sub-grain boundaries (white lines in the grain map) exist.

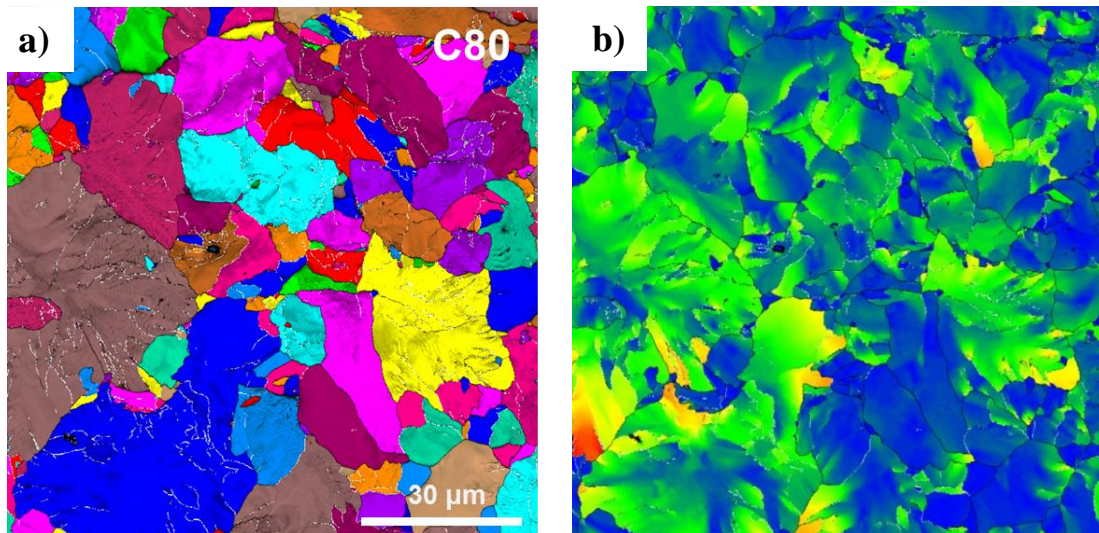


Figure 4.13. The PF grain map (a) and grain reference orientation deviation map (b) of C60 steel.

For C80 steel, the PF microstructure is very inhomogeneous with both fine and coarse grains observed (Fig.4.13). The orientation within coarse grain alters largely with division into sub-grain by low-angle boundaries. Similarly to C60, the location near triple junction between PF grains often shows large misorientation from average grain orientation.

As mentioned above, the twin-related grain map of reconstructed austenite looks similar to the PF grain map of initial microstructure for the two steels. While the annealing twin formation cannot be verified as the main mechanism of the formation of twin-related grains, a relation between the initial PF and reverse austenite microstructures is expected.

In case of reversion from P in C80 steel, there are two essential conditions for the formation of twin-related austenite grains from PF. That is:

- The A can nucleate at several different locations within the PF grain
- A twin selection rule, which implies that within a single PF grain, the nuclei of reserved austenite should choose either the orientation bearing an OR with PF or a twin of that orientation.

The first condition ensures that several austenite grains can be nucleated from one PF grain. According to previous observations [35-38] and the observed austenite microstructure in present study, the main nucleation sites of A from a PF grain are either triple junction with raising local misorientation or the boundary of earlier nucleated A. The second condition restricts the orientation of nucleated austenite. The austenite should chose an orientation bearing and OR with PF, from which it nucleated or a twin of that orientation.

To make clear the role of F on nucleation of austenite reversed from a mixture of P+F, a dual-phase microstructure of C40 steel was investigated. The C40 steel was chosen instead of C60, because it is easier to receive a dual phase microstructure for the

former steel due to its broader A+F region in the phase diagram. The initial microstructure of C40 was P+F. After heating to 1073K - slightly lower the Ac3 temperature of this steel and holding for 0.6ks, P is fully reverted to A, while the F partially remained. Subsequence iced brine quench causes martensitic transformation from austenite, but the ferrite remains untransformed. The EBSD image quality map of as-quenched C40 specimen shows a dual-phase mixture of M+F (Fig.4.14a). The M has typical lath morphology, while the F grains are coarser with more bright contrast. The martensite was selected for reconstruction of prior-austenite grain orientations. The reconstructed result in Fig.4.14b represents a dual-phase A+F microstructure, which formed at 1073K. In this microstructure, different austenite grain orientations were stained by separate colors. The austenite grain boundaries were also classified into low-angle, twin, other CSL and randomly high-angle types in the same manner used above. The F grain was colored following the A grain, with whom it bears an OR. Almost austenite grains have an OR with their neighbor F. The specific twin-related grain morphology of austenite microstructure is also found in this case (Fig.4.15).

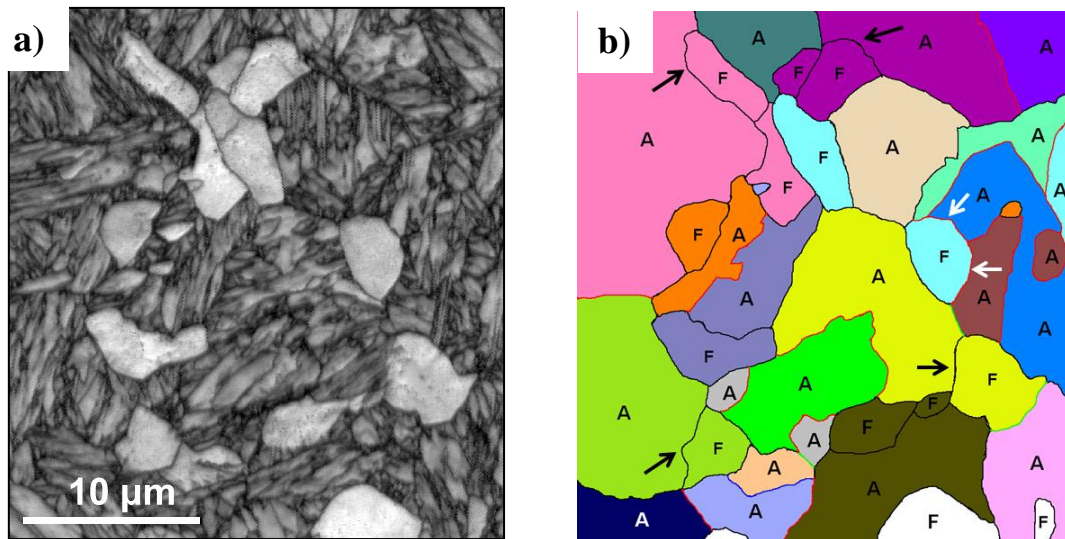


Figure 4.14. EBSD image quality map (a) and reconstructed dual phase microstructure A+F (b) of C40 (the possible nucleation sites at F boundary indicated by the arrows).

With presence of F, two additional nucleation modes of reversed A are observed, which are indicated by arrows in Fig.4.14b. Namely,

- 1 - The reversed A nucleates at F boundary with whom it bears an OR (black arrows in Fig. 4.14b);
- 2 - The A nucleated at F boundary which is in OR with a twin of that austenite orientation (white arrows in Fig. 4.14b).

The presence of F in P+F steels provides additional nucleation sites for A formation, while the twin selection rule is general for reversed austenite nuclei irrespective of their nucleation sites.

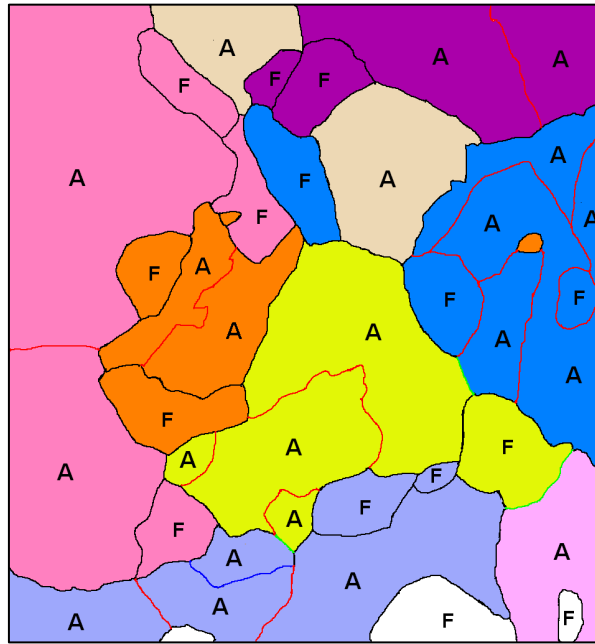


Figure 4.15. *The twin-related map of reconstructed A+F microstructure of C40.*

4.4.2. Prior-austenite microstructure in Japanese sword

In this section, the prior-austenite microstructures of J90 sample in form of a short knife and a Japanese sword were investigated. As description in 2.1, the J90 sample is made from high carbon steel by traditional method for preparing Japanese sword [47-49]. The initial carbon content of this steel is 0.98 mass%, while the final carbon content of J90 sample after preparation is 0.86 mass%. Fig represents the optical microstructure of initial 0.98mass% carbon steel, which contains white particles of cementite and dark pearlite matrix. The effect of traditional sword making method on the formation of austenite microstructure will be studied, while the austenite microstructure of C80 steel is taken as reference.

The modern Japanese sword is called Okimitsu. The chemical composition analysis was not done for this sword, but the carbon content was evaluated from the OR between austenite and martensite (Fig.5.4b). The carbon content is estimated from OR to be around 0.65mass% and the reliability of evaluation method will be discussed in the next chapter. For discussion on the effect of preparation method on austenite microstructure of the sword, the austenite microstructure of C60 steel will be taken as reference.

The EBSD measurement was performed at normal mode on cross section of J90 knife and the sword. The observed area is $100 \times 100 \mu\text{m}^2$, near the sharp edge. Both EBSD and optical microscopic observations reveal a lath martensite microstructure near the sharp edge of the two samples. The austenite microstructure is reconstructed from martensite by the above described method.

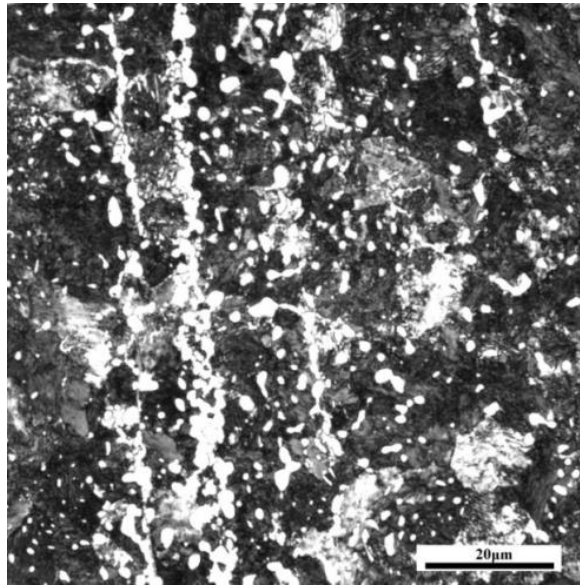
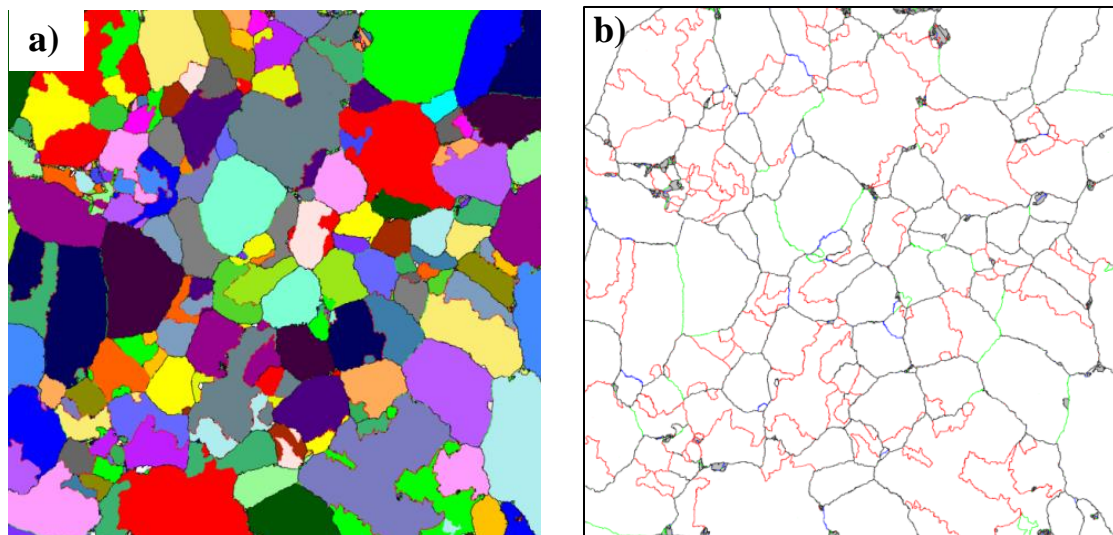


Figure 4.16. *Initial microstructure of high carbon steel used for making J90 sample*



	Fraction
Red – $\Sigma 3^n$ ($\Sigma 3$, $\Sigma 9$, $\Sigma 27$):	0.43
Green – other CSL :	0.07
Blue – low-angle :	0.02
Black – High angle :	0.48

Figure 4.17. *Reconstructed austenite grain map (a), grain boundary map (b) of J90.*

Fig.4.17a shows the reconstructed austenite grain map of J90 sample, which contains 131 austenite orientations. Although the carbon content of J90 steel is similar to that of C80 steel, the grain size is significantly finer in the former steel. The boundary map reveals details of boundary structures with 0.43 fractions of twin boundaries (Fig.4.17b).

The total fraction of twin boundaries with other CSL boundaries is 0.5. In the boundary map, there are some small areas in grey color, which are remained non-indexed due to scatter of martensite orientations. It is confirmed that the martensite within these areas are related to more than one austenite orientation, although their size is very small.

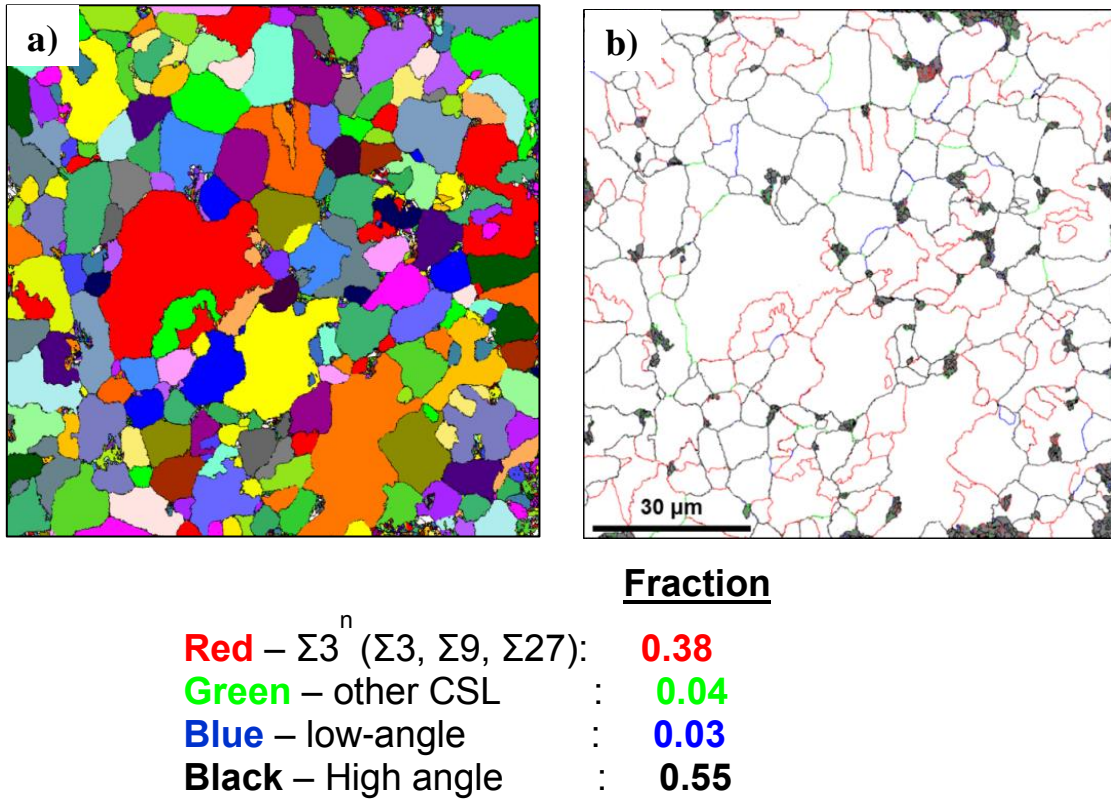


Figure 4.18. Reconstructed austenite grain map (a), grain boundary map (b) of the sword.

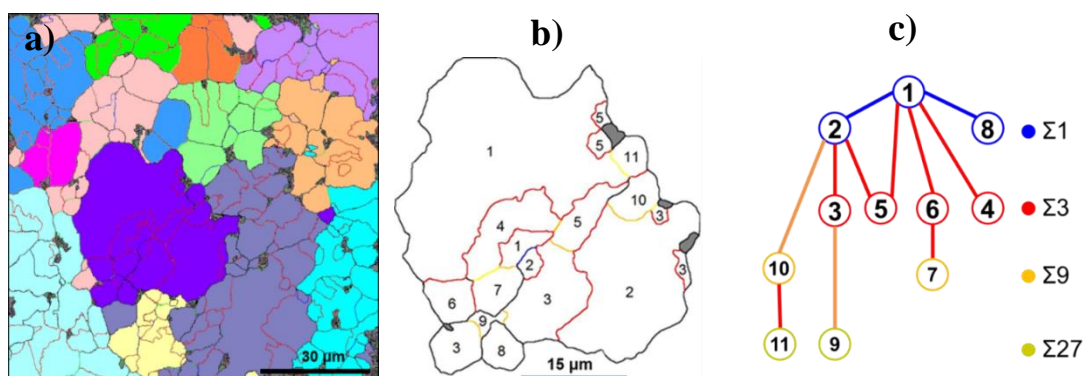


Figure 4.19. Twin-related grain map (a), a group of twin-related grain (b), twin tree describing the twin relationship (c) for the sword.

For the sword, reconstructed austenite grain map, which contains 189 austenite orientations, is represented in Fig.4.18a. The microstructure is very fragmented, where both fine and coarse grains are observed. The average grain size is $7.5\mu\text{m}$. The

boundary map reveals boundary characteristics with 0.38 fractions of twin boundary in red color (Fig.4.18b). In comparison with C60 steel, the microstructure of the sword is finer, but the fraction of twin boundaries is substantially smaller. In reconstructed microstructure of the sword, there are many small martensite areas which are related to more than one austenite orientations (areas with grey color in Fig.4.17b and Fig.4.18b). Those areas often contain more than one austenite orientations, which may be the twin of the neighbor larger austenite grains. Since the austenite orientations were not able to be found for these martensite areas, the boundary characteristics are also unknown. Thus, the fraction of twin boundaries in reconstructed microstructure of the sword is significantly smaller than that of C60 steel because the fraction of non-indexed martensite areas in the sword is remarkably larger.

The twin-related map of the sword is shown in Fig.4.19 with a grain-like structure. This map reminds the same map of C60 steel, where the size of twin-related grains is very coarse. On reconstructed microstructure of the sword, an area with twin-related grains was selected for analysis (Fig.19b). This area comprises 11 austenite orientations. The twin relationship, which is described by twin tree, shows that orientation 1 was decomposed into 11 orientations by twinning. Orientation 1 decomposed into numbers 2 and 8 with low-angle misorientations. Subsequently, the orientation 2 and 8 decomposed into other orientations by twinning or multiple twinning (Fig.4.19c).

Fig.4.20 shows the deviation of each boundary from correct twin type in degrees. The deviation values are from 1.0 to 7.7 degrees. These twin boundaries are far from annealing twin type because of large deviations and irregular shapes. It is likely that the twin-related orientations were decomposed from orientation 1 by the same mechanism observed for the ordinary carbon steels.

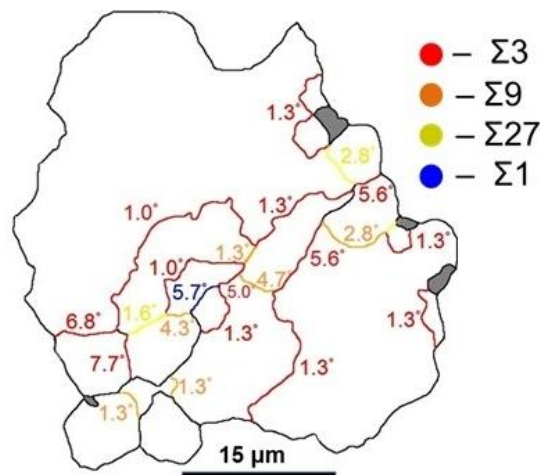


Figure 4.20. The deviation of each boundary from exact twin expressed in degree, the inserted color key showing different types of twin boundaries for the sword.

It is likely that the mechanism of austenite microstructure formation in the Japanese sword is similar to that of ordinary steel, which is controlled by the reverse transformation of austenite from P or P+F. The effects of traditional sword making method on austenite microstructure of carbon steel are visible as finer average grain size

and the presence of small non-indexed austenite orientations. Although the grain size is finer in the J90 sample, the fraction of twin boundary is not substantially higher than that of C80 steel. For the austenite microstructure reversed from P (C80 and J90) the fraction of twin boundaries is lower, but the fraction of other CSL boundaries is higher than the corresponding values of the austenite reversed from a mixture of P+F (C60 and the sword). The average austenite grain size of the sword is finer, but the microstructure is extremely inhomogeneous with several very coarse grains. The inhomogeneity of austenite grains is characteristic of all reconstructed microstructures. It is evident that the austenite microstructure formation in carbon steel is controlled by the reverse transformation, and the traditional fold-forging operations applied for the sword does not change that mechanism. The thermo-mechanical effect of the traditional method may only cause increase of nucleation sites for austenite reversion, which results a finer average grain size. The obtained knowledge may be important for control on austenite microstructure in order to obtain a fine and homogeneous distribution of austenite grains size.

To study the effect of twinning on martensite morphology, packet and block maps were plotted for the selected martensite area in Fig.4.21. The packets were represented by 04 colors, while the blocks by 12 colors according to the numbers of packet and block types. Previous studies pointed out that the packet and block sizes are responsible to mechanical properties of martensitic steel [9-11]. From Fig. 4.21, it is obviously that those values are proportional to the prior-austenite grain size. From this point of view, twin boundaries have refinement effect on the effective grain size of martensitic steel.

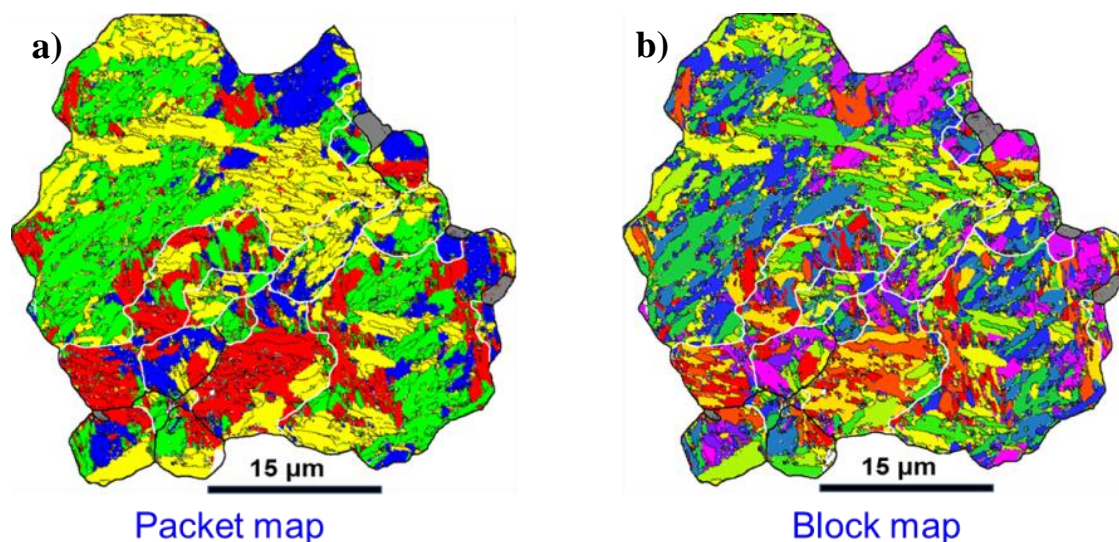


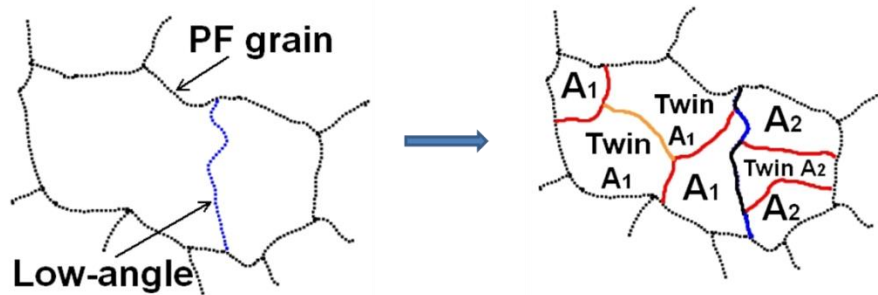
Figure 4.21. The packet and block map of selected martensite area in Fig.4.19, the white lines represent the prior austenite grain boundaries including twinning boundaries.

4.5. Conclusion

In this chapter, the concept of “prior-austenite microstructure” was proposed. A new method for precise reconstruction of austenite microstructure from EBSD data of martensite was developed. The method was applied successfully for reconstruction of austenite microstructure in several high carbon steels. A specific morphology of twin-related neighbor grains in prior-austenite microstructure of high C steels was firstly observed and described. Several conclusions on the formation of prior-austenite microstructure in high carbon steels are obtained as follows:

1) In case of reversion of austenite from full pearlitic microstructure, there are two essential conditions for the formation of twin-related austenite grains from pearlitic ferrite (PF). That is:

- The nucleation of austenite should occur at different locations within one PF grain. The favorable nucleation is triple junction between PF grains.
- A twin selection rule, which implies that within a single PF grain, the nuclei of reversed austenite should choose either the orientation bearing an OR with PF or a twin of that orientation.

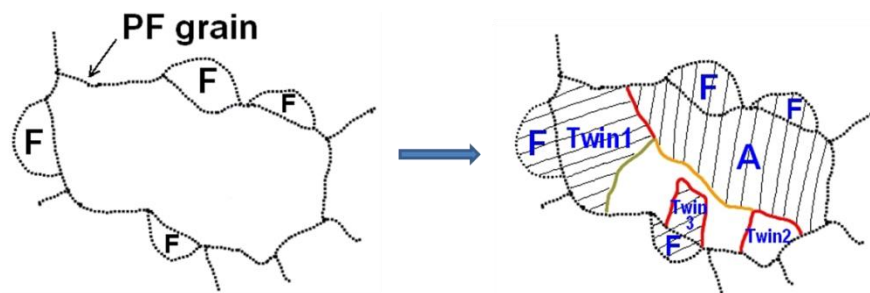


Schematic illustration of twin related austenite grains by reversion from full pearlitic microstructure

2) In case of reversion of austenite from a mixture of P+F. With presence of F, two additional nucleation modes of reversed A are observed:

- The reversed A nucleates at F boundary with whom it bears an OR.
- The A nucleated at F boundary which is in OR with a twin of that austenite orientation

The presence of F in P+F steels provides additional nucleation sites for A formation, while the twin selection rule is general for reversed austenite nuclei irrespective of their nucleation sites.



Schematic illustration of twin related austenite grains by reversion from a P+F microstructure

3) It is likely that the mechanism of austenite microstructure formation in the Japanese sword is similar to that of ordinary steel, which is controlled by the reverse transformation of austenite from P or P+F. The effects of traditional sword making method on austenite microstructure of carbon steel are visible as finer average grain size and the presence of small non-indexed austenite orientations.

Reference

- 1) R. A. Grange: Metall. Trans. **2** (1971) 65-78.
- 2) G. Krauss: Mater. Sci. Eng.A **273–275** (1999) 40–57.
- 3) H. J. Kim, Y. H. Kim and J. W. Morris, Jr.: ISIJ Int.**38** (1998) 1277-1285.
- 4) J. W. Morris, Jr., C. S. Lee and Z. Guo: ISIJ Int.**43** (2003) 410-419.
- 5) Z. Guo, C.S. Lee, J.W. Morris Jr.: Acta Mater.**52** (2004) 5511-5518.
- 6) S. Takaki, K. Fukunaga, J. Syarif, T. Tsuchiyama: Mater. Trans.**45**, No.7 (2004) 2245-2251.
- 7) S. Morito, H. Saito, T. Ogawa, T. Furuhashi, T. Maki: ISIJ Int.**45** (2005) 91-94.
- 8) H.K.D.H. Bhadeshia, R. Honeycombe: Elsevier (2006) pp. 360.
- 9) S. Morito, H. Yoshida, T. Maki, X. Huang: Mater. Sci. Eng.A **438–440** (2006) 237-240.
- 10) T. Furuhashi, K. Kikumoto, H. Saito, T. Sekine, T. Ogawa, S. Morito, T. Maki: ISIJ Int. **48** (2008) 1038–1045.
- 11) J.W. Morris, Jr.: ISIJ Int.**48**, No.8 (2008) 1063-1070.
- 12) X.F. Zhang, P. Han, H. Terasaki, M. Sato, Y. Komizo: Mater. Sci. Tech. **28**, No.3 (2012) 241-248.
- 13) A.J. Kaijalainen, P.P. Suikkanen, T.J. Linnell, L.P. Karjalainen, J.I. Kömi, D.A. Porter: Alloys Comp. **577**, Supp.1 (2013) 642-648

- 14) J.W. Morris Jr, C. Kinney, K. Pytlewski and Y. Adachi: *Sci. Technol. Adv. Mater.***14** No.1 (2013) 208-216.
- 15) P. Shanthraj, M.A. Zikry: *Mech. of Mater.* **58** (2013) 110-122.
- 16) A.W. Brewer, K.A. Erven, G. Krauss: *Mater. Charac.* **27**, No.1 (1991) 53-56.
- 17) L. Zhang, D.C. Guo: *Mater. Charac.***30**, No.4 (1993) 299-302.
- 18) C.G. Andrés, M.J. Bartolomé, C. Capdevila, D.S. Martín, F.G. Caballero, V. López: *Mater. Charac.***46** (2001) 389-398.
- 19) C.G. Andrés, F.G Caballero, C Capdevila, D San Martín: *Mater. Charac.* **49**, No.2 (2002)121-127.
- 20) K.S. Cho, H.S. Sim, J.H. Kim, J.H. Choi, K.B. Lee, H.R. Yang, H. Kwon: *Mater. Charac.***59**, No.6 (2008) 786-793.
- 21) K.S. Cho, H.S. Sim, J.H. Kim, J.H. Choi, K.B. Lee, H.R. Yang, H. Kwon: *Mater. Charac.***59**, No.6 (2008)786-793.
- 22) D.S. Martín, Y. Palizdar, R.C. Cochrane, R. Brydson, A.J. Scott: *Mater. Charac.***61**, No.5 (2010) 584-588.
- 23) M. Humbert, N. Gey: *Appl. Cryst.***35** (2002) 401-405.
- 24) C. Cayron, B. Artaud, L. Briottet: *Mater Charact.***57** (2006) 386-401.
- 25) P. Blaineau, L. Germain, M. Humbert, N. Gey: *Solid State Phen.***160** (2010) 203-210.
- 26) G. Miyamoto, N. Iwata, N. Takayama, T. Furuvara: *Acta Mater.***58** (2010) 6393–6403.
- 27) G. Miyamoto, N. Iwata, N. Takayama, T. Furuvara: *ISIJ Int.***51** (2011) 1174–1178.
- 28) L. Germain, N. Gey, R. Mercier, P. Blaineau, M. Humbert: *Acta Mater.***60**, No.11 (2012) 4551-4562.
- 29) D.G. Brandon: *Acta Metall.* **14** (1966) 1479-1484
- 30) V. Randle: *Mater. Charac.* **47** (2001) 411- 416.
- 31) A. Roósz, Z. Gácsi, E.G. Fuchs: *Acta Metall.* **31**, No.4 (1983) 509-517.
- 32) F.G. Caballero, C. Capdevila, C.G. Andres: *Metall. Mater. Trans. A* **32** (2001) 1283-1291.
- 33) G. Caballero, F. Capdevila, C.G. Andrés: *ISIJ Int.* **41**, No.10 (2001) 1093-1102.
- 34) E. Schmidt, Y. Wang, S. Sridhar: *Metall. Mater. Trans.A* **37**, No.6 (2006) 1799-1810.
- 35) S. Watanabe and T. Kunitake: *Tetsu-to-Hagané* **61** (1975) 96-106.

- 36) D.V. Shtansky, K. Nakai, Y. Ohmori: *Acta Mater.* **47**, No.9 (1999) 2619-2632.
- 37) Z.D. Li, G. Miyamoto, Z.G. Yang, T. Furuhashi: *Scripta Mater.* **60**, No.7 (2009) 485-488.
- 38) Z.D. Li, G. Miyamoto, Z.G. Yang, T. Furuhashi: *Metall. Mater. Trans.A* **42**, No.6 (2011) 1586-1596.
- 39) N. Nakada, T. Tsuchiyama, S. Takaki, S. Hashizume: *ISIJ Int.* **47**, No.10 (2007) 1527-1532.
- 40) I. Lischewski, G. Gottstein: *Acta Mater.* **59**, No.4 (2011) 1530-1541.
- 41) C.B. Thomson, V. Randle: *Scripta Mater.* **35**, No.3 (1996) 385-390.
- 42) C.B. Thomson, V. Randle: *Acta Mater.* **45**, No.2 (1997) 4909-4916.
- 43) V. Randle: *Acta Mater.* **52** (2004) 4067-4081.
- 44) V. Randle, Y. Hu: *Mater. Sci.* **40** (2005) 3243-3246.
- 45) W.D. Callister, D.G. Rethwisch: Wiley & Sons (2012) pp. 910.
- 46) V. Randle, P.R. Rios, Y. Hu: *Scripta Mater.* **58**, No.2 (2008) 130-133.
- 47) B. Dodd: *Mech. Working Tech.* **2** (1978) 75-84.
- 48) T. Inoue: *Acta Mech.* **214**, No.1-2 (2010) 17-30.
- 49) G. Takami, T. Ohba, S. Morito, A.K. Das: *Mater. Sci. Forum* **654-656** (2010) 134-137.

Chapter 5

The orientation relationship between austenite and lath martensite

5.1. Introduction

Martensitic transformation in steel is cooperative, since an OR is hold between the parent austenite and the martensite. The OR between lath martensite and austenite is so far reported to be varying from K-S, N-W or G-T types by different researchers working on different sample steels [1-12]. These OR are expressed by the parallel relationship between low-index planes and low-index directions of austenite and martensite (Table 5.1). However, all the reported orientation relationships are quite close to each other. For instant, the difference between K-S and N-W is only 5.26° . The misorientation between K-S and G-T is 2.40° , while misorientation between N-W and G-T is 2.86° . A general OR for lath martensite can be characterized by small deviation θ_1 between close-packed planes and θ_2 between close packed directions of the two phases. The well-known ORs are also expressed in term of θ_1 and θ_2 (Table 5.1).

Table 5.1. *Expression of various ORs reported for lath martensite.*

OR	Plane parallel	Direction parallel	θ_1 , degree	θ_2 , degree
K-S	$\{111\}_\gamma // \{011\}_{\alpha'}$	$\langle 111 \rangle_\gamma // \langle 011 \rangle_{\alpha'}$	0	0
N-W	$\{111\}_\gamma // \{011\}_{\alpha'}$	$\langle 001 \rangle_\gamma // \langle 011 \rangle_{\alpha'}$	0	5.26
G-T	-	-	1.0	2.5

The K-S type is probably the most popular OR used for lath martensite [13-20]. The reason of using K-S OR is that this OR indicates simply the parallelism between close-packed planes and close-packed directions of parent and product phases. The OR is the most useful for a comprehensive description of crystallography of martensite variants. Additionally, the morphology of lath martensite can be clearly classified by using K-S OR [13-14]. Unfortunately, the rational ORs like K-S or N-W are not verified either by phenomenological theory or by experiment. The phenomenological theory predicts an irrational orientation relationship, which indicates a certain deviation between the close-packed planes or directions of the two phases [6,25]. In other words, there is not mutual parallelism between low index planes or directions, so the OR should be irrational.

The ORs experimentally measured by TEM [4-5,11] or EBSD [8-10,12] also are irrational, which are closer to G-T than K-S type. Nevertheless, these irrational ORs are sometimes indicated as near K-S types. Although the crystallography of lath martensite including the OR has been studied by many researchers for more than a half of century, a general OR for lath martensite has not been confirmed for any authors. The ORs obtained by different authors have different values of θ_1 and θ_2 , although they are close to each other [1-12]. While some authors reported an irrational OR for lath martensite,

the other authors claimed that several rational ORs like K-S or N-W exist for different observation areas of one sample [8-9].

There are three reasons, which may cause the scatter of measurement result of ORs for lath martensite. The first reason is the difference in chemical composition of the steels used for experiments. The second reason is limitation of experimental technique or calculation method, which may cause rough approximation of the obtained OR. The last reason is the statistical reliability of the measure (the effect of the number of probe or measurement). Since the most common method for accurate measurement of OR is TEM, it is expected that only a small number of measurements or probes can be conducted. Recently, the EBSD also used for measurement of OR either directly [8-9,12] or indirectly [10]. Although the EBSD method allows substantially expansion of observation area, the measurement of OR is often completed only for several austenite grains [7-10,12]. Since the number of measurements is relatively small, it is impossible to quantify the statistical reliability of the method.

As described in chapter 3, the OR can be calculated from EBSD data of martensite with precision 0.2° , when the calculations were done for 3 austenite grains of a low alloy steel. In this section the OR will be calculated for various steels with the number of grains used for calculation up to 100 grains. The effect of chemical composition on OR and the statistical characteristics of the calculation method will be investigated.

In this study, the misorientation between martensite variant will be characterized experimentally. The effect of chemical composition on misorientation distribution between martensite variants will also be investigated.

5.2. Experimental

A series of carbon steels C10, C40, C60 and C80 was used for study on the effect of carbon on OR. The series of low alloy steels C10Mn15, C10Mn30, C10Ni15 and C10Ni30 was used for study on the effect of Mn and Ni. The series of Japanese sword steels J60, J90 and a modern sword with unknown composition were used for study on the effect of processing on the OR.

5.2.1. Calculation of orientation relationship

To study on the reliability of the method applied for calculation of OR, 100 austenite grains taken from EBSD data of the Japanese sword are used to calculate OR. The measured ORs are expressed for calculation convenience, through the orientation of the first variant (V1) of martensite in austenite frame, in form of 3x3 matrices. An average OR is defined as the orientation which has the minimum average misorientation from all of 100 calculated ORs. This average OR is numerically calculated by minimizing the average deviation. After the average OR is found, the misorientation of each measured ORs from average OR is calculated. The obtained misorientations are used for plot of cumulative distribution. The distribution of misorientation between calculated ORs and average OR is close to the standard normal distribution (Fig 5.1).

According to the standard normal distribution, the value of average misorientation $\bar{\theta}$ is 0.34° and standard deviation σ is 0.16° . It is likely that 80% of the fitted ORs has the misorientation from average OR smaller than $\bar{\theta} + \sigma = 0.5^\circ$. Thus the average OR can be

accepted at the true value of OR and the error of calculation of OR using the present method is 0.5° . For given steel, the ORs measured for different prior austenite grains as well as for different locations within one austenite grain are likely identical with the error of 0.5° . The obtained precision is comparable with that of TEM method.

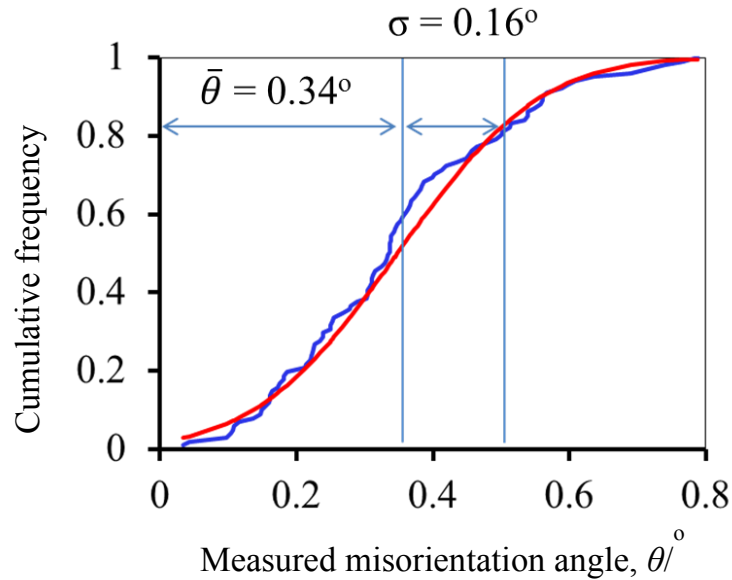


Figure 5.1. Cumulative distribution of misorientation of fitted OR from average value: experimental distribution – blue line, normal standard distribution – red line.

The carbon steels are J60 and J90 with original carbon content of 0.76 and 0.98 mass%, respectively. These steels were used for preparing two short knives by a traditional method, which has been used for making Japanese sword as described above. Both of steels were undergone about 12 successive fold-forging operations with formation of two short knives. Since the microstructure of lath martensite at the sharp edge is of interest, the duplex construction with insertion of low carbon steel core was not applied for those knives. After preparation, the knives have full lath martensite microstructure [5], and the carbon contents of J60 and were reduced to 0.62 and 0.86 mass% respectively (table 2.2).

5.2.2. Calculation of misorientation between martensite variants

The OR is also evaluated by the characteristics of misorientation between martensite variants [17,20]. Since the angle θ_1 , which expresses the deviation between $\{111\}_\gamma$ and $\{011\}_\alpha'$ is small, the misorientation between martensite variants which share the same plane orientation relationship can be expressed by rotation around $\langle 011 \rangle_{\alpha'}$ rotation axis.

In this study, the misorientations between martensite variants from V1 to V6, which share the same plane parallel relationship $\{111\}_\gamma // \{011\}_\alpha'$ are used for characterization of OR. After the average OR is calculated for each steel, the OR is used for calculation of orientation of six martensite variants V1:V6. The misorientation between those martensite variants is calculated and expressed through rotation around $[011]_{\alpha'}$. The misorientation between martensite variants are calculated for K-S, N-W and G-T ORs and average OR of C10, which are represented in Table 5.2.

It is interesting while the deviation between ORs is relatively small; the misorientations between martensite variants are clearly distinguishable (Table 5.2). It shows that the average OR of C10 steel is obviously close to G-T type than other rational ORs. For specific pair of martensite variants, the small plane parallel deviation θ_1 causes deviation of rotation axis from $[001]_{\alpha'}$, while the direction parallel deviation θ_2 cause significant deviation of rotation angle from that of K-S type. From this point of view, the small change in OR can be tracked by observation of the misorientations between specific pairs of martensite variants.

Table 5.2. *Misorientation between martensite variants sharing a close-packed plane orientation relationship (V1:V6).*

OR	Misorientation between variant pair, $[011]_{\alpha'}/\theta^\circ$			
	V1-V4, V3-V6, V5-V2	V1-V6, V3-V2, V5-V4	V1-V3, V3-V5, V5-V1, V2-V4, V4-V6, V6-V2	V1-V2, V3-V4, V5-V6
K-S	10.53	49.47	60.00	70.53
N-W	-	60.00	60.00	60.00
G-T	5.72	54.27	60.00	65.72
OR*	5.57	54.49	60.02	65.53

*The average OR of C10 was added for comparison

The misorientations are also calculated directly for experimental martensite variants from EBSD data.

The calculation method is as follows:

- For each scan point, the misorientation matrix between this point and its neighbor is calculated.
- From the misorientation matrix, the misorientation in term of $\langle 011 \rangle_{\alpha'}$ rotation axis / angle is calculated. The calculation involves symmetry operations in form of 24 conversion matrices C_i , $i=1-24$ (Table 3.1). For a given pair of scan points, the misorientation with rotation axis, which is the closest to $\langle 011 \rangle_{\alpha'}$ will be chosen.
- Since the orientation of martensite in real sample is locally rotated, the misorientation between adjacent scan points which belong to the same martensite variant can reach several degrees. For this reason, a threshold value of 4° is used to determine the minimum misorientation angle between two different martensite variants.

It is clearly that the misorientation angles calculated for a given pair of variants are dispersive. When a histogram of misorientation angles measured for EBSD data are plotted, the distribution of misorientation angle is received (Fig. 5.2). Hereafter, the only misorientation angle is used in description of misorientation between the martensite variants, since the $[011]_{\alpha'}$ rotation axis is common for all of martensite

variant pairs. In that figure, the 232,000 measured misorientation angles for C10 steel, which values are larger than 50° are used for plot histogram with discrete intervals (bin) of 0.1° . The distribution shows some local peaks of misorientation which positions are closed to the theoretical values of misorientation between martensite variants calculated from average OR (Table 5.2). It is important to investigate the distribution of misorientation angles around their peaks in order to accurately determine the average value of misorientation between martensite variants. Since the peaks are close, their distributions interfere with each other. The linear level is used to separate the interfered peaks as shown in Fig.5.2 for calculation of average misorientation.

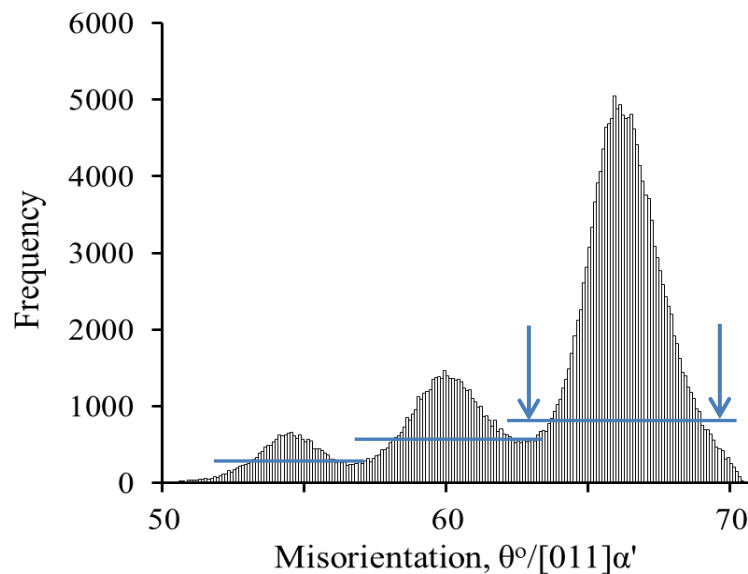


Figure 5.2. Histogram of measured misorientation angles in C10 steel martensite with interval 0.1° .

Using the linear section to separate the distribution peak near 66° , which is indicated by the arrows in Fig.5.2, all of measure misorientation values within an interval from 63.2 to 69.1° are selected. In this case, more than 156,000 measured misorientations are selected. The histogram of selected misorientations is plotted with interval of 0.01° as shown in Fig. 5.3a. The cumulative distribution of measured misorientation is shown as blue solid curve in Fig.5.3b, while the standard normal distribution is red dot curve.

It is obviously that the measurement of large population of misorientations has random characteristic, which is almost standard normal distribution. Hence, the average value of selected misorientations can be accepted as the true value of measured misorientation by the presence method with the error equal to standard deviation of measurement. In this example, the average misorientation of the selected peak is 66.18° and the error of measurement is 1.24° (Fig.5.3b).

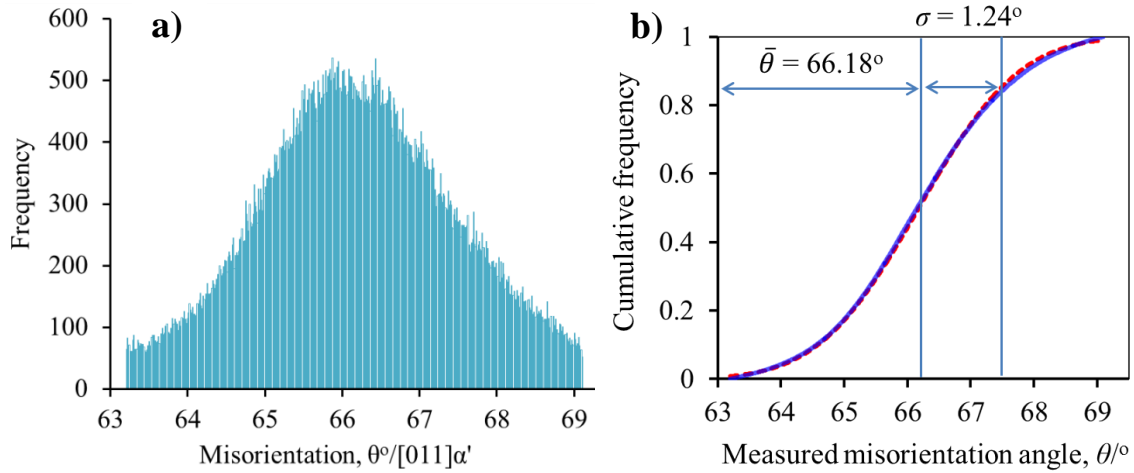


Figure 5.3. a) Histogram of measured misorientation angles around the 66° peak of 5.2; b) The cumulative distribution of misorientations represented in a: blue – measured distribution, red dot line – standard normal distribution.

By using the above described method, the misorientations between specific martensite variants are calculated for all of sample steels. The results will be analyzed to show the effect of chemical composition on OR.

5.3. Result and discussion

5.3.1. Effect of carbon

a) Effect of carbon on orientation relationship

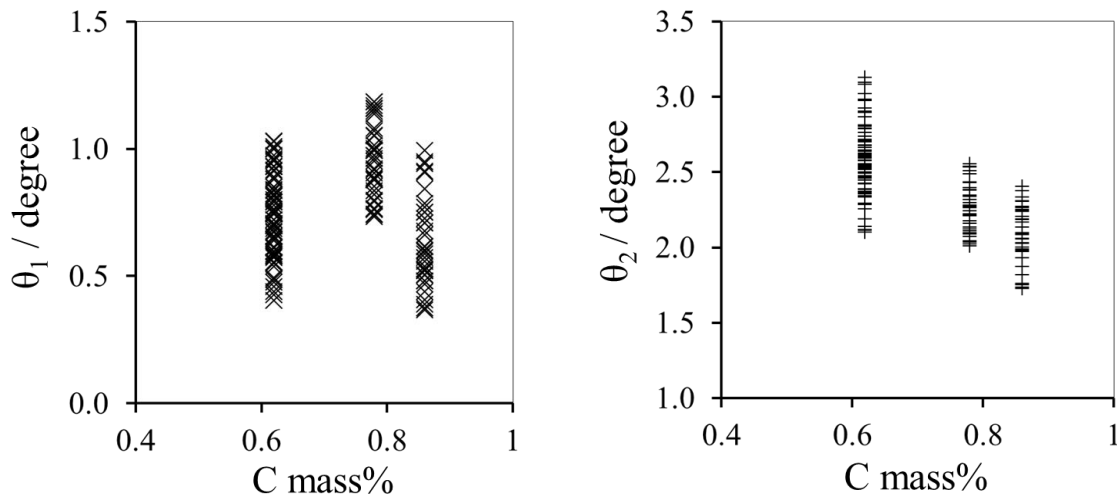


Figure 5.4. The variation of ORs represented through θ_1 and θ_2 with carbon content in case of numerous measurement.

The OR was calculated for various carbon steels with carbon content in range of 0.1-0.9mass% C. Fig.5.4 shows the variation of ORs represented through θ_1 and θ_2 with carbon content in case of numerous measurements for C60, C80 and J90 steels. For C80 steel the ORs were calculated for 50 grains, while for C60 and J90 the calculation was

conducted for more than 100 grains. In case of numerous measurements, the variations of θ_1 and θ_2 from average values can reach 0.5° . A linear decrease of θ_2 with increase of carbon content is observed for the given range of Carbon content (Fig.5.4b), while the dependence of θ_1 on carbon content is not clear.

In Fig.5.5, the θ_1 and θ_2 of average OR were plotted for all carbon steels whose carbon contents are well known. It shows a non-uniform effect of carbon on the OR. The increase of Carbon from 0.1 to 0.4 mass% causes sharp decrease of θ_1 , while the inverse effect on θ_2 is observed. On the other hand, when the carbon content raises from 0.4 to 0.86 mass%, θ_1 is almost unchanged, but θ_2 monotonically decreases. It is likely that the effect of carbon is switched to monotonic decrease of θ_2 , when the carbon content in steel reaches a critical value. From Fig.5.5b it is obviously that this critical content of carbon is lower than 0.4 mass%. The similar effect of carbon on morphology of martensite in carbon steel is also expected, since the change in OR may cause corresponding change in martensite morphology.

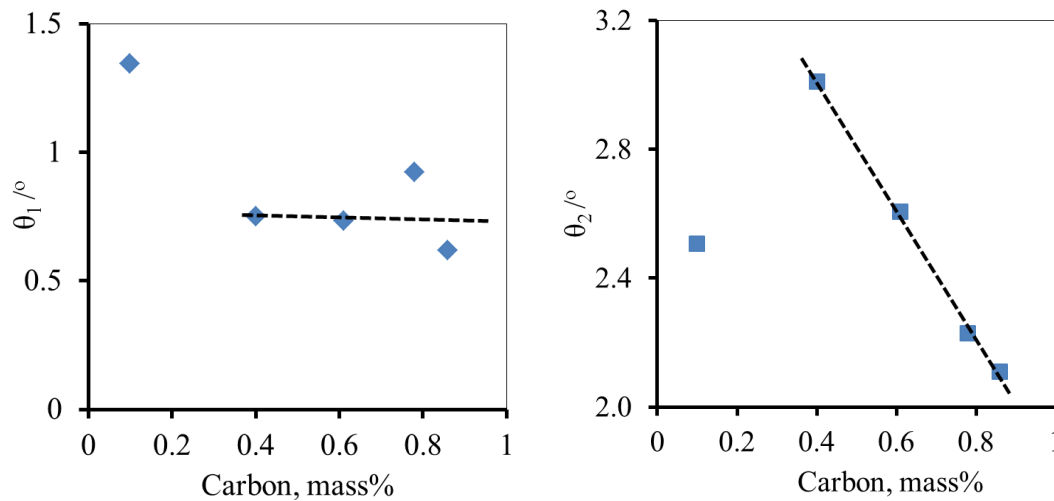


Figure 5.5. Variation of θ_1 and θ_2 of average OR as a function of carbon content.

Because the high carbon steel samples are dominant, in this study we will focus the discussion on these steels with carbon content from 0.38 to 0.86 mass%. From Fig.5.5, it is likely that the increase of carbon content does not cause change in plane parallel relationship between martensite and austenite (θ_1), while it causes linear decrease in deviation between close-packed directions (θ_2). For this range of carbon content, the dependence of θ_2 (in degree) on carbon content (in mass%) can be expressed through Eq. (5.1).

$$\theta_2 = 3.81 - 1.99\rho \quad (5.1).$$

where ρ is the carbon content in mass%.

The presence of carbon as interstitial impurity in martensite lattice is the reason of its tetragonality, which is characterized by the c/a ratio of body centered tetragonal (bct) lattice. A linear dependence of tetragonality on carbon content has been well known as following equation [21]:

$$c/a = 1 + 0.046 \rho \quad (5.2).$$

The distribution of carbon atom at octahedral interstitial sites of martensite causes a tetragonal distortion of its lattice. Hence, the OR which is the correspondence between austenite and martensite lattices, should be also dependent upon the carbon content. It is likely that linear increase of tetragonality of martensite lattice cause linear decrease of deviation between the close-packed directions of austenite and martensite. However, the reason why the effect of carbon on θ_1 is less significant than on θ_2 , or the reason why θ_2 linearly decrease with carbon content are not clarified in this study. A further investigation is needed in order to understand this phenomenon.

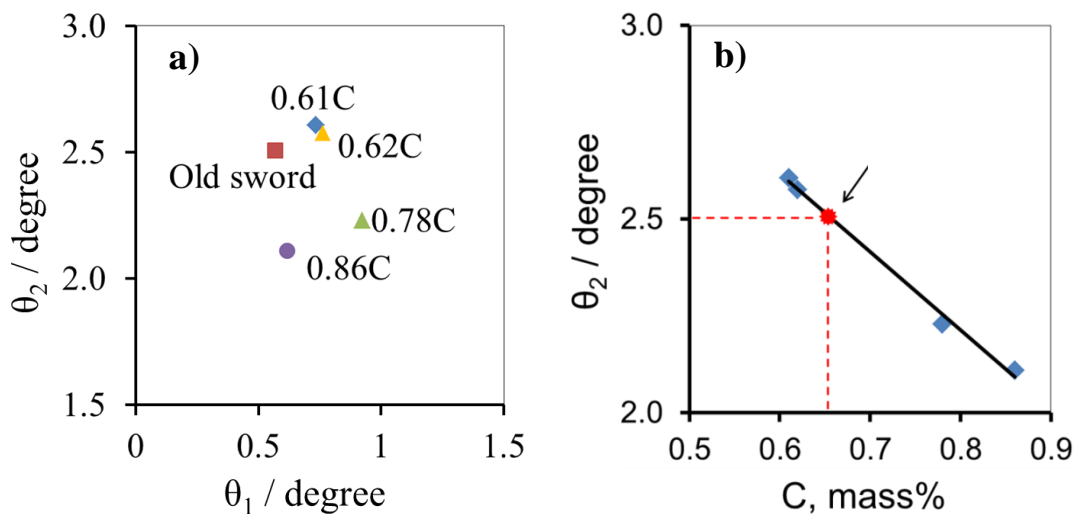


Figure 5.4. Average OR of high carbon steels in term of θ_1 and θ_2 (a), calculation of carbon content for the Japanese sword from the value of θ_2 (b).

Nevertheless, the obtained result can be utilized in estimation of carbon content. Fig.5.4a shows the average OR represented by the values of θ_1 and θ_2 of different carbon steels and a Japanese sword. The numbers next to each point express the carbon content in mass% of corresponding carbon steel, while the carbon content of the sword is unknown. While the ORs are represented by both θ_1 and θ_2 the dependence is not clear (Fig.5.4a). From that figure, it is found that the OR of the sword is close to that of C60 and J60 steels. The carbon content of the sword is expected to be around 0.6 mass%, but the concrete value cannot be obtained from this graph. Use of Eq.5.1 is a better way for estimation of carbon content in the sword. From this equation and its graphic representation in Fig. 5.4b, the carbon content of the sword is approximately 0.65 mass%. This estimated carbon content of the sword is in agreement with the reported 0.6-0.7 mass% of carbon content of other Japanese swords which were produced during the same period [26-30].

It should also be noted that the application of Eq.5.1 is limited for the range of carbon steels used in this study, which is from 0.4 to 0.9 mass%. Although the steel with higher carbon content has not been checked, the upper limit of ρ in Eq. 5.1 should be less than 2.0 mass%. If value of ρ is taken higher than 2.0 mass%, the Eq.5.1 will

return negative value of θ_2 . Therefore, an abrupt change in OR is expected for the steel with higher carbon content than the upper limit for that linear equation. Actually, the change of OR from near K-S to N-W type is experimentally observed for the steel with carbon content > 1.4 mass% [22], when the morphology of martensite becomes lenticular type.

b) Effect of carbon on distribution of misorientations between martensite variants

As mentioned above, the misorientations between martensite variants are sensitive to the change in OR. When a large enough number of measurements is carried out, the distribution of measured misorientation is almost standard normal distribution as pointed out in section 5.2.1.

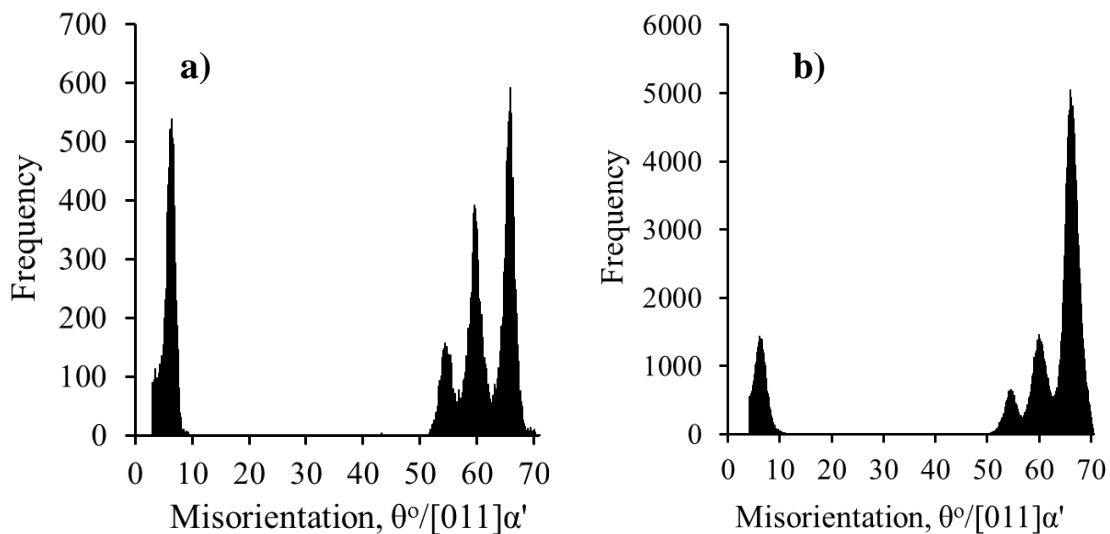


Figure 5.5. Histogram of measured misorientation angles in C10 steel martensite with interval 0.01° .

Fig. 5.5 shows the effect of measurement scale on the distribution of misorientations. In Fig.5.5a, the measurement result is represented for one specific austenite grain. The dominance of small misorientation 5.6° and near twin misorientation 66.2° which correspond respectively to V1-V4 and V1-V2 variant pairs, are observed. The small misorientation between V1-V4 pair is the evidence of interleaved block structure, which is combination of two sub-blocks with small misorientation as mentioned in chapter 1.

In fig.5.5b which represents measurement result for a $100 \times 100 \mu\text{m}^2$ area, a different portion of misorientation peaks is observed. The near twin peak remains dominance, while the small misorientation peak becomes remarkably small. While the values of average misorientations are almost identical for the both measurements, the portion between misorientation peaks clearly depend upon the scale of measurement. Since the large scale measurement has more statistical reliability, the measurement of misorientation is conducted in large area of martensite (approximately $100 \times 100 \mu\text{m}^2$ area) for all of steels studied.

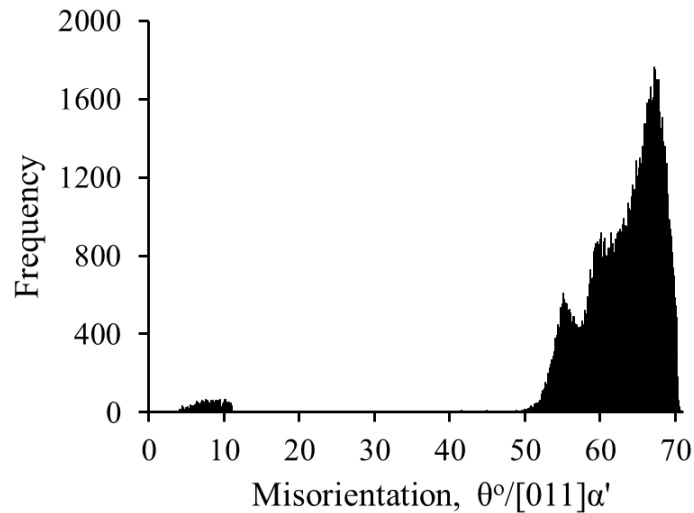


Figure 5.6. Histogram of measured misorientation angles in C40 steel martensite with interval 0.01° .

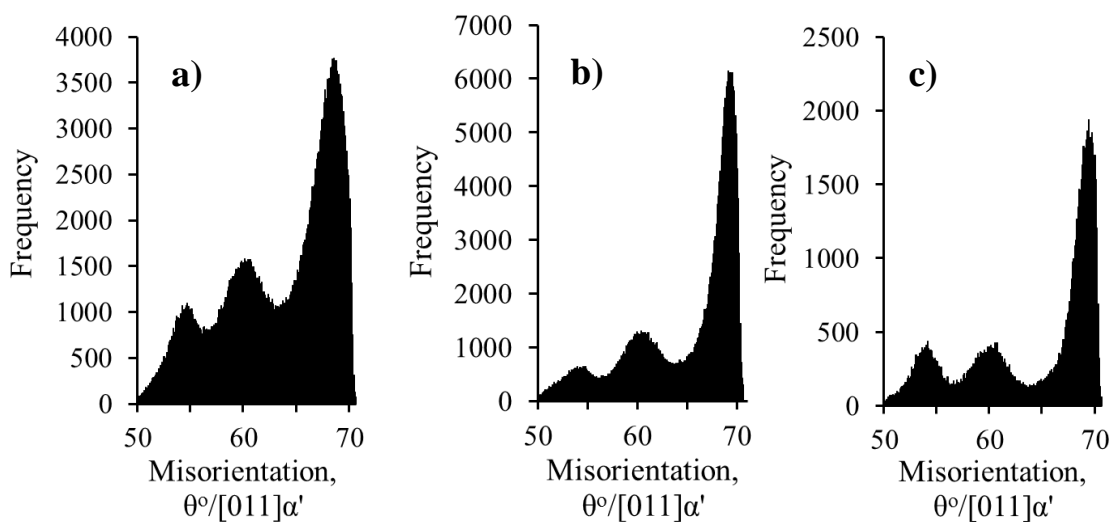


Figure 5.7. Histograms of measured misorientation angles with interval 0.01° : a – C60, b – C80, c – J90.

Fig.5.6. represents the misorientation distribution of C40 steel, whose pattern is completely changes. In difference from C10 steel, the small-angle misorientation peak almost disappears, while the high-angle misorientation peaks are much superimposed. The missing of small-misorientation peak is evidence of morphology change in C40 compared with that of C10 steel. The block morphology is switched from interleaved type in C10 steel to single type, which contains only one martensite variant. As discussed above, due to the abrupt increase of θ_2 when carbon content raises from 0.1 to 0.4 mass%, the high-angle misorientation peaks become close to each other. As a result, these peaks in the histogram of C40 steel compared with that of C10 are much superimposed. The change in OR due to carbon content, causes the change in block morphology and misorientation between specific pair of martensite variants. The

missing of low-angle misorientation peak is also a characteristic of other steel with carbon content higher than 0.4 mass%. Therefore, for those steels, the histograms are only plotted for misorientation angles larger than 50° .

Fig.5.7. shows the histograms of C60, C80 and J90 steels, which are plotted for high-angle misorientations. For all of the steels, the near twin misorientations are dominant. The increase of carbon content causes slight change of the portion between two other peaks. The average value is calculated for each misorientation peak using the above described method. The dependence of average misorientation between martensite variants on the carbon content is shown in Fig.5.8. The black circles represent misorientation values calculated directly from OR and the red squares are average values of measured misorientations.

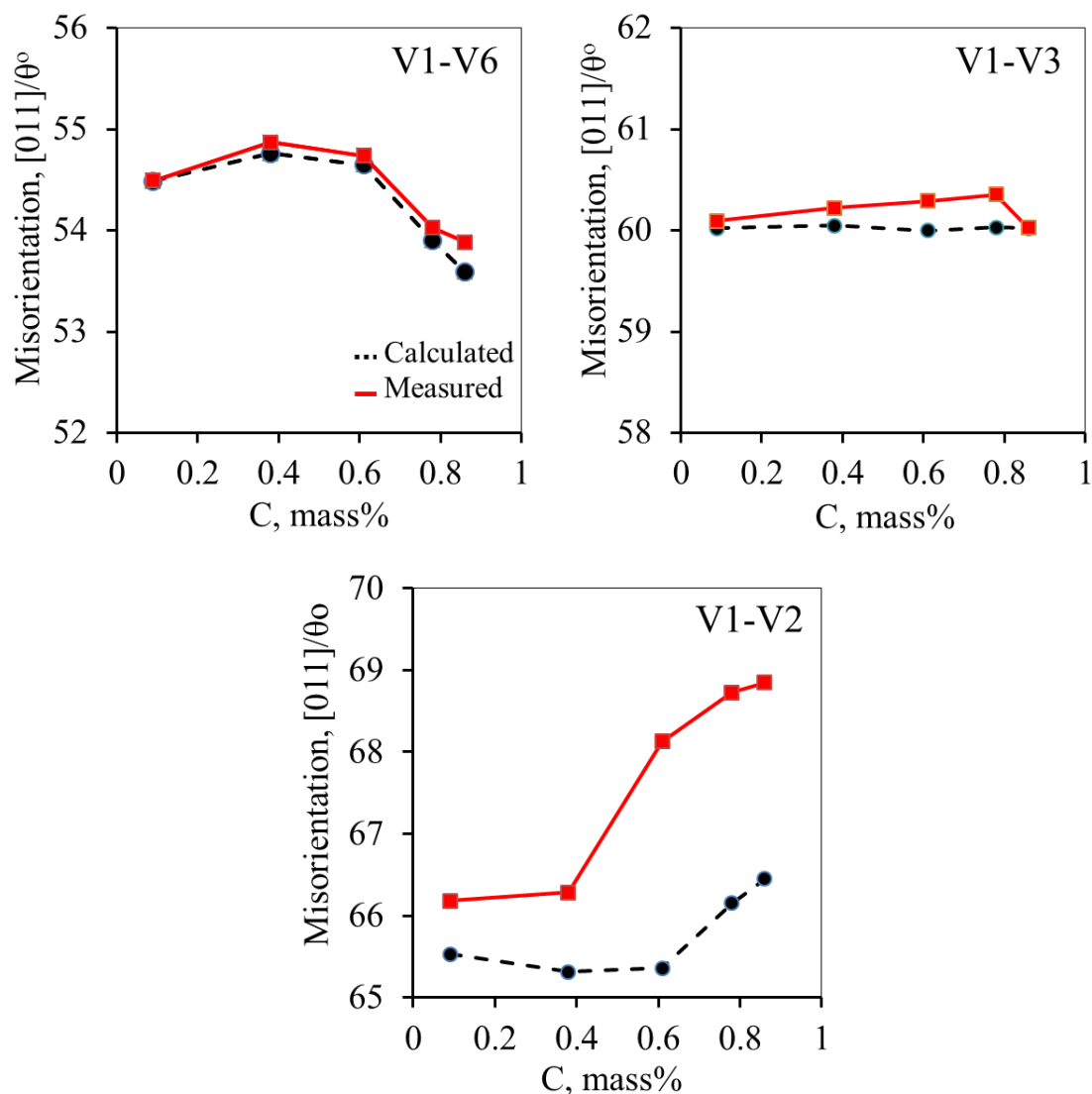


Figure 5.8. *The effect of carbon content on the misorientations between martensite variants.*

From this figure, several conclusions are received. Firstly, it shows that the variation of measured misorientation with carbon content is in well agreement with the calculated

value for all pairs of martensite variants. This fact indirectly validates the accuracy of present method for calculation of ORs. Secondly, it shows that the carbon has different effects on the misorientations. While the misorientation of V1-V3 pair is almost independent on carbon content, the misorientations of V1-V6 and V1-V2 shows contrary behaviors with carbon content. The misorientation of V1-V6 pair decreases when the carbon content increases from 0.4 to 0.86 mass%. In an opposite manner, the misorientation of V1-V2 pair increases with carbon content. It should also be noted that the measured misorientations are slightly higher than calculated values for V1-V3 and V1-V6 pairs, but measured misorientation of V1-V2 pair is remarkably higher than calculated value. Moreover, the gap between measured and calculated misorientations is also increase with carbon content.

The reason why the measured misorientation is always higher than calculated value is not clear, but there are two possible explanations for this phenomenon. One of the reasons may be the existence of film-like retained austenite at martensite boundary, which was observed for high carbon steels [23]. This film of retained austenite is very thin, about 20nm. The film of austenite may cause increase of misorientation between martensite variants measured across the boundary.

For this reason, the misorientation is also calculated for the EBSD data, from which all of scan points next to the boundaries were deleted. Since the size of scan point is 100 nm, which is larger than the size of possible austenite film, the effect of this film on measurement of misorientation may be eliminated by this way. The measurement result of misorientation between V1-V2, which was conducted for the data without boundary points, is plotted as blue rhombs in Fig. 5.9.

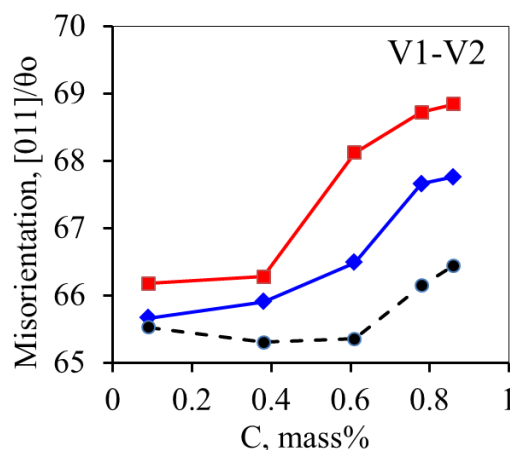


Figure 5.9. The effect of carbon content on the misorientations between V1-V2.

The misorientation measured without boundary points is lower than with boundary points but it still significantly higher than the calculated value. On the other hand, the film of retained austenite is only partially observed at some location in the observation field [23]. It is likely that the presence of thin film of retained austenite is not the main reason of the above mention phenomenon.

Another possible reason is the change of martensite orientation at the near twin boundary. As shown in the histogram of misorientations, the near twin misorientation of V1-V2 pair is dominant for all of studied steels. The change of martensite block morphology from interleaved type to single variant type is also observed from these histograms. It is also reported that the block size of carbon steel decrease with increase of carbon content. In other words, the blocks as “grain” of single martensite variant become finer with carbon content. In formation of such fine grained microstructure, obviously the role of boundary energy becomes more significant.

From all of these facts, it is likely that for V1-V2 pair of martensite variants, the boundary structure is adjusted toward the twin relationship in order to reduce boundary energy. With increasing of carbon content from 0.4 to 0.86 mass%, the measure misorientation of this pair of variants approaches the exact misorientation of the twin relationship as shown in Fig. 5.9. The quantitative assessment of change in boundary energy by misorientation adjustment will be discussed in the next chapter.

5.3.2. Effect of other alloying elements

a) Effect of Mn and Ni on orientation relationship

Fig.5.10 shows the averaged ORs of Mn and Ni added steels. It is likely that the addition of Mn or Ni up to 3.0 mass% does not affect θ_2 , but increase of θ_1 is clearly observed. The dependence of θ_1 upon alloying content is plotted in Fig.5.11. Similarly to Eq.(5.1), the dependence of θ_1 upon Mn or Ni content can be expressed through Eq.(5.3) and Eq.(5.4) respectively:

$$\theta_1(\text{Mn}) = 0.887 + 0.248\rho_{\text{Mn}} \quad (5.3)$$

$$\theta_1(\text{Ni}) = 0.899 + 0.182\rho_{\text{Ni}} \quad (5.4)$$

where ρ_{Mn} or ρ_{Ni} are the content of Mn or Ni in mass%.

It is interesting to note the different effects of C as interstitial impurity and Mn or Ni as substitutional impurity on the ORs. As discussed above, while the interstitial carbon distorts tetragonally the lattice of ferrite, it causes decrease of deviation between close-packed directions θ_2 . On the other hand, the substitutional elements such as Mn or Ni, which cause expansion of ferrite lattice [24], are responsible for increase of deviation between close-packed planes θ_1 . According to the study of Sutton et. al. [24] on lattice spacings of solid solution of several substitutional elements in ferrite, the formation of solid solution results in an expansion of ferrite lattice, and for equal atomic percentages, Mn causes abnormally larger expansion than Ni. The similar behaviors of Mn and Ni are observed, when Mn cause larger increase of θ_1 than Ni for the same atomic percentages of solute (Fig. 5.11).

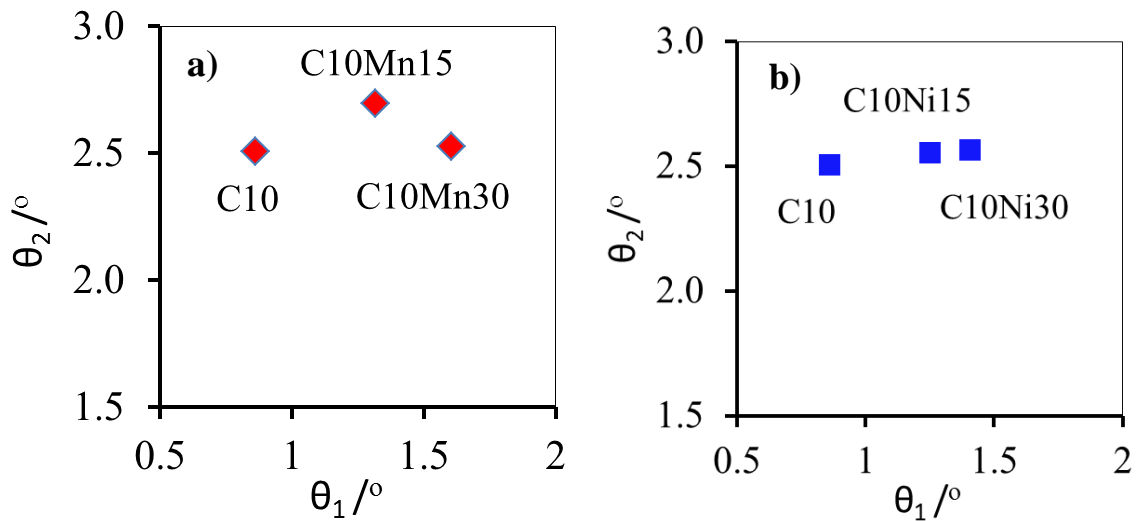


Figure 5.10. Average OR of Mn steels (a) and Ni steels (b) in term of θ_1 and θ_2 .

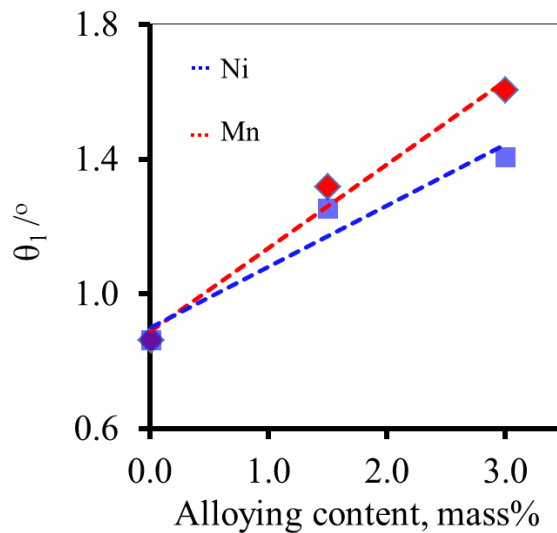


Figure 5.11. Variation of θ_1 with content of alloying element: Mn – blue rhomb, Ni – red square.

It is likely that the expansion of ferrite lattice by substitutional impurity causes the increase of deviation between close-packed planes of austenite and martensite. There more expansion of martensite lattice the substitutional element causes, the more deviation between close-packed planes of the two phases happens. However, the present result should not be extended for a wide range of alloying contents or for more complex alloying systems, since the interactive between alloying elements may cause unexpected effects on the OR.

b) Effect of Mn and Ni on distribution of misorientations between martensite variants

The distributions of misorientation between martensite variants are also plotted for Mn added steels in Fig.5.12. and Ni added steels in Fig. 5.13. The addition of Mn up to 3 mass% causes decline of the small-angle peak compared with C10 carbon steel.

The similar change in morphology of block with additional of Mn was also reported in [14,16]. The blocks changes from interleaved type in C10 to single variant type with finer size when Mn is added.

However, the effect of Mn on block morphology is weaker than that of C, since the small-angle misorientation peak clearly remains in the steel with 3 mass% of Mn. Both single variant blocks and interleaved blocks exist for the given Mn content. The near twin misorientation peak is still dominant, though the other high angle misorientation peaks become more significant than in C10 carbon steel. When the Mn content increase from 1.5 to 3.0 mass%, the high angle misorientation peaks become interred (Fig 5.12b).

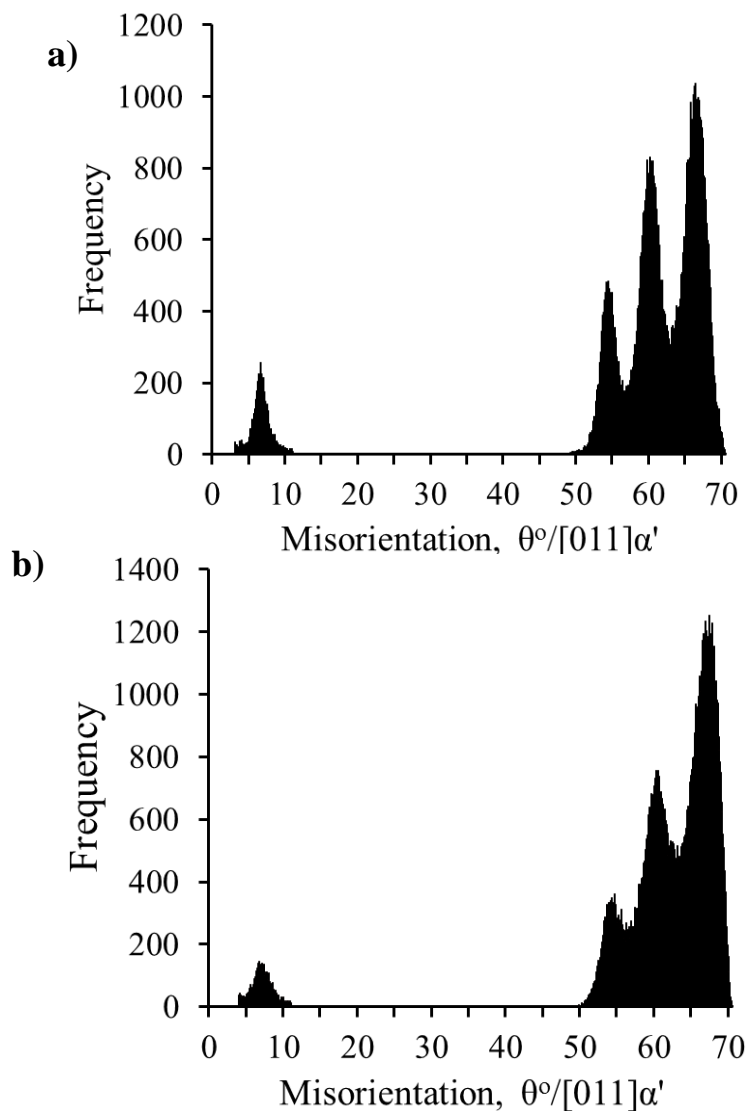


Figure 5.12. Histograms of measured misorientation angles of Mn added steels with interval 0.01° : a – C10Mn15, b – C10Mn30.

Addition of Ni content from 1.5 to 3.0 mass% shows an opposite effect on the appearance of low-angle misorientation peak (Fig.5.13). The steel with 1.5 mass% of Ni shows a significant decline of this peak compared with Mn added steel. However, the distribution of misorientations could not represent quantitative change of misorientation peaks. This kind of assessment is made by plotting the average misorientation between martensite variant versus the alloying content as shown in Fig.5.14.

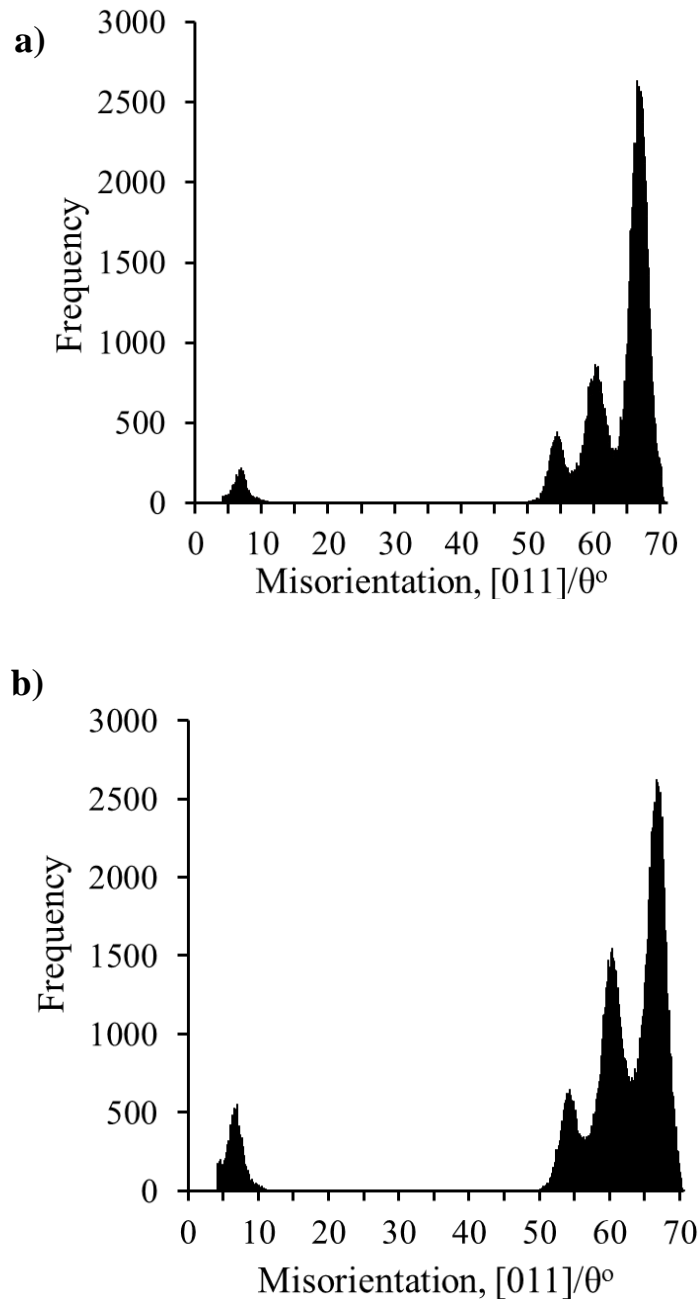


Figure 5.13. Histograms of measured misorientation angles of Ni added steels with interval 0.01° : a – C10Ni15, b – C10Ni30.

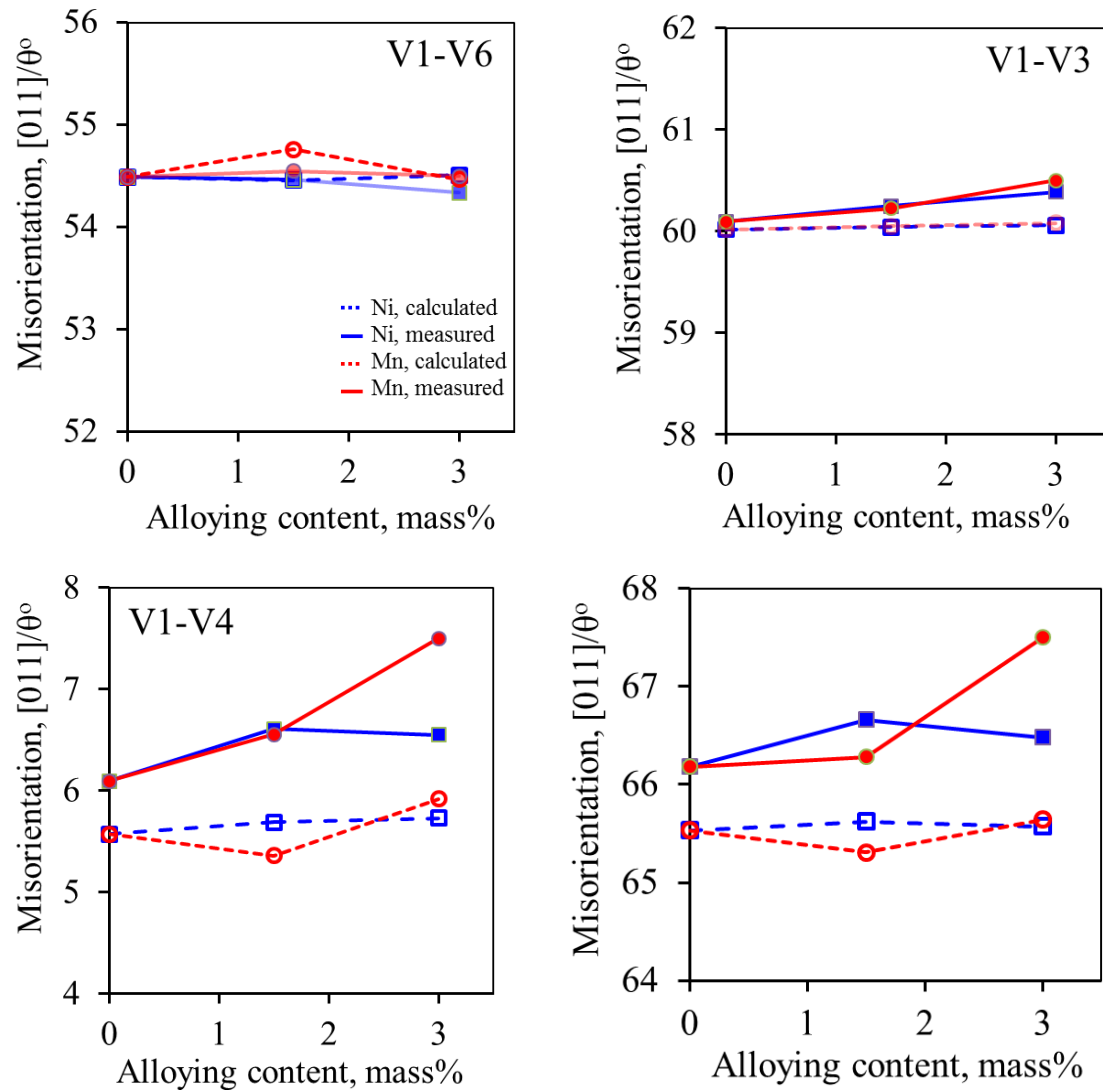


Figure 5.14. The effect of alloying content on the misorientations between martensite variants.

Similarly to the case of carbon steels, the additional of Mn or Ni does not show a significant effect on misorientation of V1-V3 pair of martensite variants. The measured misorientations, which increase gradually with alloying content, are slightly higher than calculated values (Fig.5.14b). Both Mn and Ni also do not affect the high-angle misorientation of V1-V6 pair. In that case, the measured values are slightly lower than calculated ones (Fig.5.14a).

The effect of Mn or Ni is clearly observed for the cases of low-angle misorientation of V1-V4 pair and near twin misorientation of V1-V2 pair (Fig.5.14a and b). For both alloying elements, the measured values of misorientation are larger than calculated values, although the tendency of variation of those values is in good agreement. It is likely that misorientation between those pairs of variants are adjusted at their boundary in order to reduce the boundary energy as discussed above for carbon steel. While addition of Mn from 1.5 to 3.0 mass% causes increase of those misorientations, the addition of Ni with equal contents shows an opposite effect. That abnormal effect of Ni is not clearly understood in the frame of this study.

5.4. Conclusion

In this chapter the following conclusions on OR between austenite and martensite are received:

1) The statistical reliability of the method for calculation of OR was assessed by repeating the calculation for relatively large number of austenite grains (more than 100 grains). The error of the calculation is assessed to be 0.5° and the average OR, which have minimum average deviation from all of measured ORs can be used to represent the true OR of studied steels.

2) Increase of C as interstitial impurity in martensite lattice from 0.1 to 0.86mass% causes mainly decrease of the deviation between closed-packed directions θ_2 . The reason may be the presence of tetragonality of martensite lattice when C is added. The change of OR also causes change of block morphology, which is switched from interleaved type in C10 steel to single variant type in steels with carbon content larger than 0.4 mass%.

3) The deduction of θ_2 with increase of C in range of 0.4-0.86 mass% is linear. Using this relation, the carbon content of a Japanese sword with unknown composition can be estimated to be 0.65 mass%, which is in reported range of the other studied swords.

4) The misorientations between specific martensite variants, which share the same plane parallel relationship with austenite, are also sensitive to the change of steel composition. The misorientation distribution calculated for large number of scan points is very close to standard normal distribution. Hence the average misorientation can be calculated for each pair of martensite variants with the error of 1.24° .

5) Additional of C from 0.1 to 0.86mass% causes disappearance of low-angle misorientation peaks, which is the evident of change in block morphology. The increase of C content also causes increase of near-twin misorientation of V1-V2 pair toward exact twin relationship. Moreover, the measured misorientations are significantly larger than calculated values. It is likely that the boundary structure between those martensite variant is adjusted toward exact twin boundary in order to reduce the boundary energy. The fine single block morphology of high carbon steels also supports this assumption.

6) The substitutional elements such as Mn or Ni, which cause expansion of martensite lattice, are responsible for increase of deviation between close-packed planes θ_1 , and Mn shows a slightly stronger effect than Ni for the same content of solute.

7) The addition of Mn or Ni up to 3 mass% causes decline of the small-angle peak compared with C10 carbon steel. However, the effect of those elements on block morphology is weaker than that of C, since the small-angle misorientation peak clearly remains in the steels with 3 mass% of Mn or Ni.

The obtained results are important for deeper understanding the crystallography of martensite, since a direct link between martensite morphology, orientation relationship and chemical composition is revealed. A new viewpoint on OR is confirmed, that is the variation of martensite orientation which can reach several degrees was caused mainly by local rotation of austenite, while the OR is maintained constant for the steel with a given chemical composition.

Reference

- 1) G.V. Kurdjumov and G. Sachs: *Z. Physik* **64** (1930) 324-326.
- 2) Z. Nishiyama: *Sci. Rep. Tohoku Univ.* **23** (1934) 637-664.
- 3) G. Wassermann: *Mitt K-W-I Eisenforsch* **17** (1935) 149-158.
- 4) A.B. Greninger, A.R. Troiano: *Metals Trans.* **185** (1949) 590-598.
- 5) P.M. Kelly, A. Jostsons and R.G. Blake: *Acta Metall. Mater.* **38** (1990) 1075-1081.
- 6) W.Z. Zhang, G.C. Weatherly: *Scripta Mater.* **37**, No.10 (1997) 1569-1574.
- 7) D.W. Suh, J.H. Kang, K.H. Oh, H.C. Lee: *Scripta Mater.* **46** (2002) 375-378.
- 8) Y. He, S. Godet, J. J. Jonas: *Appl. Cryst.* **39** (2006) 72-81.
- 9) F. Barcelo, Y. Carlan, J.L. Béchade, B. Fournier: *Phase Trans.* **82** (2009) 808-820
- 10) G. Miyamoto, N. Takayama and T. Furuhashi: *Scripta Mater.* **60** (2009) 1113-1116.
- 11) Y. Meng, X.F. Gu, W.Z. Zhang: *Acta Mater.* **58** (2010) 2364-2375.
- 12) V. Ocelík, I. Furár and J.Th.M. De Hosson: *Acta Mater.* **58** (2010) 6763-6772.
- 13) S. Morito, H. Tanaka, R. Konishi, T. Furuhashi, T. Maki: *Acta Mater.* **51** (2003) 1789-1799.
- 14) S. Morito, H. Saito, T. Ogawa, T. Furuhashi, T. Maki: *ISIJ Int.* **45** (2005) 91-94.
- 15) H. Kitahara, R. Ueji, N. Tsuji and Y. Minamino: *Acta Mater.* **54**, No.5 (2006) 1279-1288.
- 16) S. Morito, H. Yoshida, T. Maki, X. Huang: *Mater. Sci. Eng.A* **438-440** (2006) 237-240.
- 17) S. Morito, X. Huang, T. Furuhashi, T. Maki, N. Hansen: *Acta Mater.* **54** (2006) 5323-5331.
- 18) S. Morito, Y. Adachi, T. Ohba: *Mater. Trans.* **50**, No.8 (2009) 1919-1923.
- 19) S. Morito, R. Igarashi, K. Kamiya, T. Ohba, T. Maki: *Mater. Sci. Forum* **638 - 642** (2010) 1459-1463.
- 20) C. Cayron, B. Artaud, L. Briottet: *Mater Charact.* **57** (2006) 386-401.
- 21) G.V. Kurdjumov: *Metall. Trans.A* **7** (1976) 999-1011.
- 22) H.K.D.H. Bhadeshia, R. Honeycombe: Elsevier (2006) pp. 360.
- 23) S. Morito, T. Ohba, T. Maki: *Mater. Sci. Forum* **558-559** (2007) 933-938.
- 24) A.L. Sutton, W. Hume-Rothery, *Phil. Mag. Lett.* **46**, No.383 (1955) 1295-1309.
- 25) P.M.Kelly: *Mater. Trans.* **33**, No.3 (1992) 235-242.
- 26) T. Inoue: *Acta Mech.* **214**, No.1-2 (2010) 17-30.
- 27) B. Dodd: *Mech. Working Tech.* **2** (1978) 75-84.
- 28) N. Sasaki, T. Momono: *Tetsu-to-Hagané* **93** (2007) 792-798.
- 29) G. Takami, T. Ohba, S. Morito, A.K. Das: *Mater. Sci. Forum* **654-656** (2010) 134-137.
- 30) A.K. Das, T. Ohba, S. Morito, M. Yaso: *Mater. Sci. Forum* **654-656** (2010) 138-141.

Chapter 6

Molecular dynamics calculation of boundary energy in lath martensite

In this chapter we have evaluated the energetic stability of boundaries between Kurdjumov-Sachs (K-S) variants to explain the morphology of sub-block and block in lath martensite. Boundary energy of different variant pairs was calculated by using molecular dynamics simulation. Three dimensional models of tilt and twist boundary with a method evaluating boundary energy were developed. The results showed energetic stability of twist boundary with small misorientation from 0 to $5.5^\circ/[011]_\alpha$ in consistence with previous transmission electron microscope observation. For other boundary with larger misorientation, the twin-related variants had the smallest boundary energy.

6.1. Introduction

As shown in previous chapter, the distribution of misorientation between martensite variants does not follow the random contribution of martensite variants with equal fraction, but a dominance of near twin misorientation is observed. Furthermore, under the effect of alloying elements, when the single variant blocks are superior to the interleaved blocks, the misorientation of near twin pair of martensite variants tends to approach the value of exact twin misorientation. To explain this phenomenon the boundary energy between martensite variants is taken in consideration, since the refinement of block size leads to abrupt increase of boundary fraction. In other word, the role of boundary energy becomes much more significant when the block size is finer.

In this chapter, we have focused on the energy of boundaries between specific martensite variants which share the same close-packed plane relationship with austenite as described in the previous chapter. Molecular dynamics (MD) simulation was used as a new approach to calculate the boundary energies between martensite variants. In general understanding, MD simulation is a computer simulation technique, where the time evolution of an ensemble of atoms (a set of interacting atoms) is followed by integrating their equations of motion [1]. The realism of MD simulation depends on the ability of the MD model and the potential chosen to reproduce the behavior of material under simulation conditions [2-3]. Hence the most essentials for a successful simulation are a validated MD model and an appropriate potential for the material.

A commercial program called SCIGRESS (Fujitsu, SCIGRESS, version 2.2.0) is used for MD simulation in this study. Originally, this program is designated for organic macromolecular system with relatively small number of atoms, while the number of atoms in MD model required for the present purpose should be as larger as possible, in order to reproduce closely the boundary between submicron-sized martensite variants. For this reason, the MD model for simulation is simplified from the real boundary in order to be compatible with the calculation program. Firstly, the model is made from pure Fe atoms without interstitial C atoms, because the proper potential for interaction

between Fe and C is not available in the present version of SCIGRESS. Secondly, the number of Fe atom for a model is limited under 60,000 atoms due to the computational capability of the program. The flow chart of a simulation procedure is represented in Fig.6.1. The details description of simulation is given in the next section.

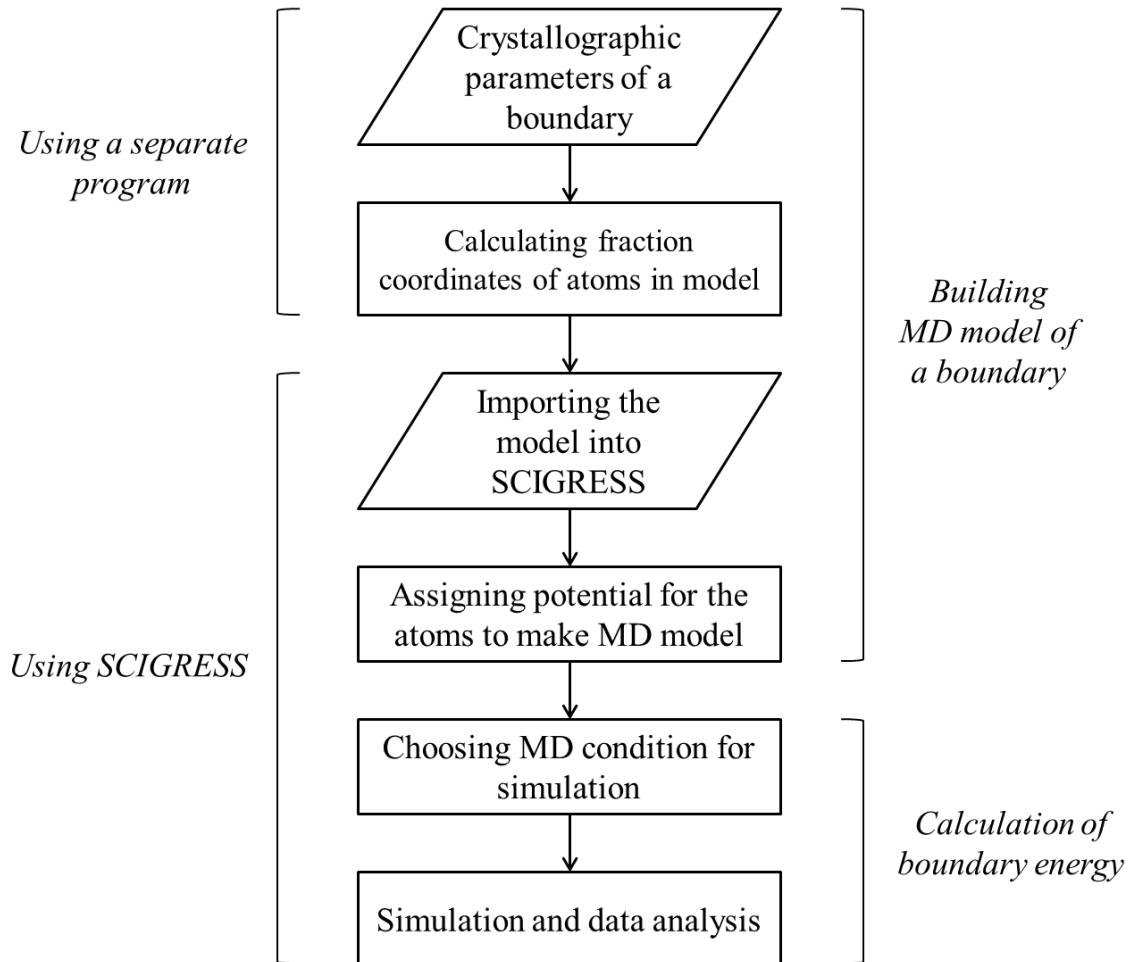


Figure 6.1. Flow chart of a MD simulation procedure in the present study.

6.2. Simulation method

6.2.1 Model construction

According to previous TEM observation [4-5], the martensite laths of the same variant are grouped together with small alternatively changing misorientation across their twist boundaries. The boundary between different martensite variants are characterized as both tilt and twist types or even a mixed type [4-5]. In this simulation, we considered the lath boundary as pure twist boundary with the misorientation varying in an extended range from 0 to $12^\circ/[011]_\alpha$. The boundary between specific martensite variants from V1 to V6 are simulated for case of tilt boundaries as well as twist boundaries. Because these martensite variants share the same plane relationship with austenite, the rotation axis between them is close to $[011]_\alpha$.

As mentioned above, the model is built for pure α Fe with bcc lattice. For

construction of the boundary between two bcc Fe crystals, the misorientation between them in form of rotation axis/ angle should be specified. From previous chapter, it is clearly that the misorientation between martensite variants depends upon the OR between austenite and martensite. Since the martensite microstructure of pure iron is not available for experimental calculation of OR by our present method, it is reasonable to use a rational orientation relationship like K-S [12] for martensite of pure iron. Using K-S OR, the rotation axis between martensite variants is exactly $[011]_{\alpha'}$. This rational rotation axis will help to simplify the algorithm for construction of both twist and tilt boundary models. Because the rotation axis is fixed as $[011]_{\alpha'}$, hereafter the misorientation between martensite variants will be expressed only by misorientation angle.

In order to calculate the boundary energy directly, we intend to not employ the periodic boundary condition for simulation, which requires the model with two symmetrical boundaries. Alternatively, we develop the model with a single boundary, which allows calculation of absolute boundary energy, as below described.

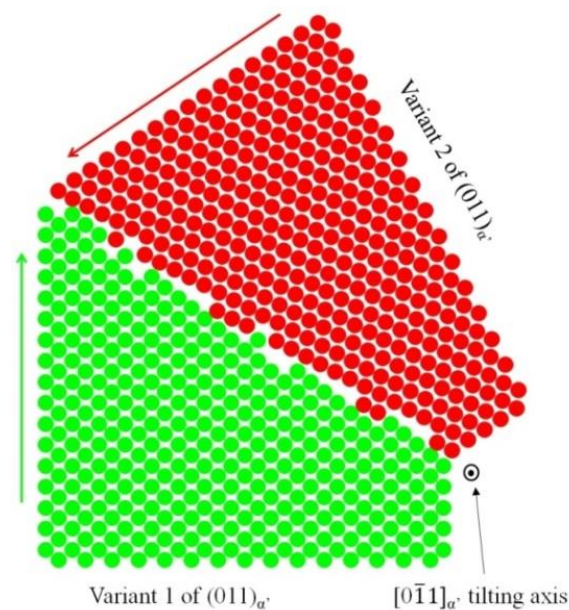


Figure 6.2. *Two dimensional model of tilt boundary between two variants of $(011)_{\alpha'}$ plane with misorientation of $[011]_{\alpha'}/60^\circ$ (the arrows indicate growing directions of these variants).*

For tilt boundary model, at first, a two dimensional (2D) tilt boundary between two $(011)_{\alpha'}$ planes was created by tilting these planes to a specified misorientation and then allow them to grow until they meet each other. The tilting axis was choose to be $[0\bar{1}1]_{\alpha'}$, which is perpendicular to the drawing field of Fig.6.2. This 2D boundary was built by a criterion of maximum atom density at the boundary. A 3D boundary is created by stacking these 2D tilt boundaries with the spacing equal to the lattice parameter of bcc Fe, so that boundary lines are aligned to form a boundary plane. A 3D box is cut out

from the 3D boundary in such a way that the boundary plane becomes a symmetry plane of the box. By this way, the 3D model of tilt boundary is built (Fig. 6.3).

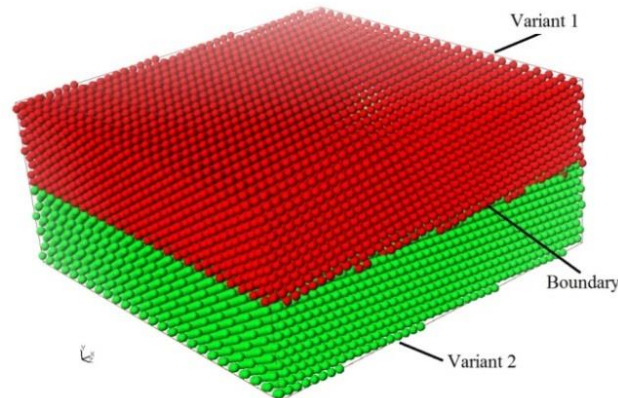


Figure 6.3. *Three dimensional model of tilt boundary between two variants of $(011)_{\alpha'}$ plane with misorientation of $[011]_{\alpha'}/60^{\circ}$.*

The model of twist boundary is created with an assumption that there is at least one common $[011]_{\alpha'}$ row of atoms between two set of $(011)_{\alpha'}$ planes exists, when placing them one on another. We then used this common row of atoms as a rotation axis to twist the upper part relatively to the lower part until the misorientation reaches the specified value (Fig.6.4a). Similarly to the case of tilt boundary, a 3D box will be cut out so that the common $[011]_{\alpha'}$ row becomes symmetrical axis and the boundary plane becomes symmetrical plane of the box as shown in Fig.6.4b.

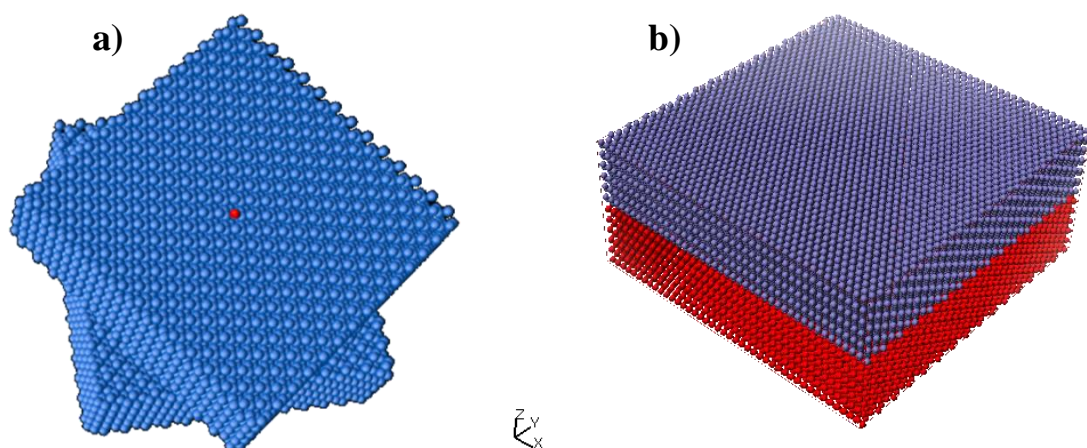


Figure 6.4. *Twist boundary of two martensite variants with misorientation $[011]_{\alpha'}/60^{\circ}$: a – The upper part is twisted around the rotation axis coincident with the common $[011]_{\alpha'}$ row of atoms is in red color; b – The 3D box with twist boundary.*

Using the above described algorithms we have been successful to encode a Fortran90 program which is able to calculate fractional coordinates of each atom in the 3D model of tilt or twist boundaries from any input value of misorientation. The

advantage of our program compared with other commercial programs for building the 3D crystallographic structure like Crystal Studio or SCIGRESS is that our program is capable for construction of both twist or till boundaries from any input misorientation and with unlimited number of atoms included. The output file, which is made compatible with SCIGRESS program, contains data of fractional coordinates of all atoms, the sizes of 3D box and crystallographic information of bcc Fe.

6.2.2. Calculation of boundary energy

a) Model size

Fig.6.3 shows a 3D model of tilt boundary between two martensite variants V1-V3 with misorientation 60° , which is represented in SCIGRESS program after importing the calculated fraction coordinates of Fe atoms. The model is in form of a $10 \times 10 \times 5 \text{ nm}^3$ box with the boundary plane in the middle of the box. The two martensite variants are represented in red and green colors. This model contains 43,000 atoms of Fe in total. The size of model is limited due to capacity of the working program and simulation time. The test on size of model on a normal Windows PC equipped with an Intel® Core™ i5 - 3.33GHz processor and 4GB of memory shows that the simulation program is interrupted while the number of atoms exceeds 140,000 atoms. With a model containing 86,000 atoms, the simulation process is extremely slow. The reasonable size of model is limited to 40,000 – 60,000 atoms, which requires 3.5 to 5h of calculation time.

b) Choice of MD potential and condition

For MD simulation of Fe system, several potentials are available in library of SCIGRESS. Those potentials are Johnson potential [6], Yang-Johnson potential [7], Finnis-Zou potential [8] and Finnis-Sinclair potential [9]. The Johnson potential is “pair” potential, which describes the interaction between a pair of interacting atoms without accounting the interaction with other neighbor atoms [3,6]. The other potentials are embedded atom method (EAM) potentials, which are developed for metallic systems with multi-atom interactions [3,10].

Table 6.1. *Simulation result using different potentials.*

Potential			Model	Simulation	
Name	Type	Ref.	Number of atoms	Time, h	Total energy, $\times 10^{15} \text{ J}$
Johnson	Pair potential	[6]	8,175	0.4	-1.73
Finnis-Zou	EAM potential	[8]	8,175	23.2	-2.90
Yang-Johnson	EAM potential	[7]	8,326	12	-5.44
Finnis-Sinclair	EAM potential	[9]	8,175	0.4	-5.24

The simulation results using different potentials for the same model of boundary are represented in table 6.1. The effectiveness of potential used is evaluated by the value of total energy of the system and the running time required for a simulation procedure. Among the available potentials, the Finnis-Sinclair (F-S) potential and Yang-Johnson (Y-J) potential give very close value of total energy. However, the running time using F-S potential is much shorter than that of Y-J potential. Hence, the F-S potential is chosen as the best candidate in the present work.

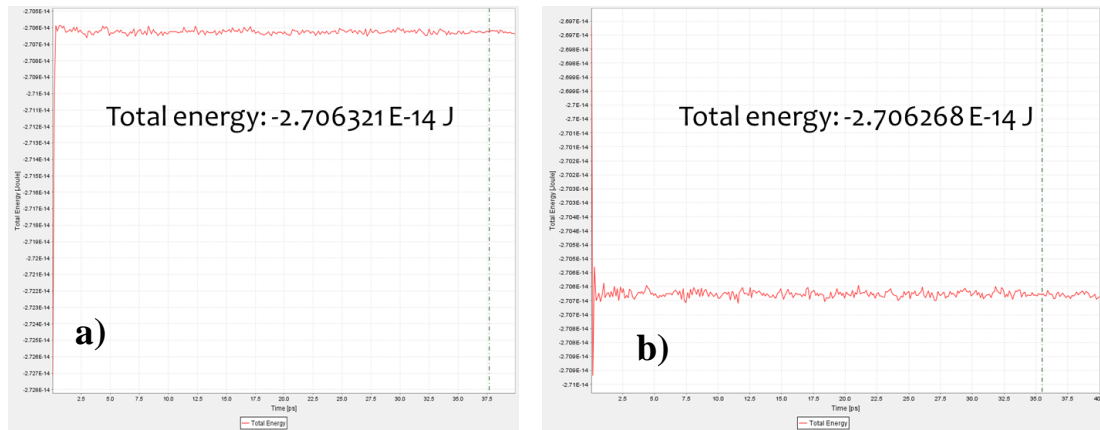


Figure 6.5. Evaluation of total energy of MD system with simulation time. The simulation time is fixed as 40ps, while the time step is changed from 1.0fs (a) to 4.0fs (b). The scales for energy are different in the two graphs.

The simulation condition is chosen as NTV ensemble, i.e. the number of atoms (N), temperature (T) and volume of model (V) were kept constant. The temperature is set as room temperature (300K). Test on simulation time and time step shows that the time step up to 4.0 fs will not change the distribution of total energy of the MD system as represented in Fig.6.5. For this reason, the time step is chosen as 4fs and the simulation with 15,000 time steps, which results 60ps of simulation time.

c) Method for calculation of boundary energy

After conducting simulation with above mentioned MD conditions, the total energy of MD model can be plotted vs. simulation time (Fig.6.5). The averaged total energy was used for calculation of boundary energy. For this purpose, the total energy of model with a single boundary between variant 1 (V1) and variant 2 (V2) which is represented in Fig.6.6, is considered to be decomposed into 3 components

$$E_{V1-V2} = 0.5(E_{V1} + E_{V2}) + E_i \quad (6.1).$$

where E_{V1-V2} is the total energy of model with a boundary between two variants V1 and V2; E_{V1} or E_{V2} is the total energy of a model with the same sizes but contains only one variant (V1 or V2) without boundary; and E_i is the total boundary energy between V1 and V2 (Fig.6.6).

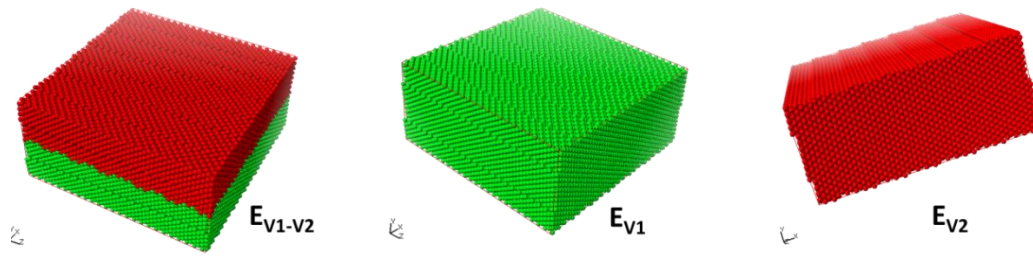


Figure 6.6. The three models used for evaluation of boundary energy.

For each calculation of boundary energy we did three simulations with three respective models of V1-V2, V1 and V2 as shown in Fig.6.6 to calculate their total energies. With the chosen size of MD model and the MD condition described above, it takes 3.5 hours of calculation time for a single model. The total boundary energy between V1 and V2 is then extracted by using Eq.(6.2).

$$E_i = E_{V1-V2} - 0.5(E_{V1} + E_{V2}) \quad (6.2).$$

And the quantitative value used for analysis is energy per area

$$e_i = E_i/S_i \quad (6.3).$$

where, e_i is the density of boundary energy and S_i is area of the boundary plane.

6.3. Result and Discussion

The calculated boundary energies between two different martensite variants were plotted versus misorientation angle, for both tilt and twist types in Fig.6.7. The result shows that the twin related martensite variant pair (V1-V2) with a misorientation angle 70.5° has the smallest boundary energy in both tilt and twist models. Only in this case, boundary energy of tilt boundary is slightly smaller than that of twist boundary. For other misorientation angles, the twist boundaries have significantly smaller energy than tilt boundaries. It is interesting that the V1-V4 pair with low-misorientation 10.5° does not show significantly advantage in boundary energy compared with other high-angle misorientation pairs in case of twist boundaries. The boundary of V1-V4 variant pair with low-angle misorientation 10.5° does have smaller energy than other boundaries with misorientation angles of 49.5° (V1-V6) or 60° (V1-V3), but its boundary energy is still 2 times higher than that of twin-related variant pair (V1-V2).

The calculation results can be used to explain the observed dominance of near-twin misorientation in the boundary between martensite variants, which have been discussed in previous chapter. According to this result, it is obvious that to minimize boundary energy the boundary between two different martensite variants should be a twin boundary of tilt or twist types. If the boundary is formed between other variant pairs, it should be a twist boundary to have smaller boundary energy.

In Fig.6.7, energy of twist boundaries with small misorientation varied from 0° to 12° was plotted. When the misorientation is changed from 10.5° to 6.0° the boundary energy is decreased. Reduction of boundary energy in this range of misorientation is not monotonous, and there are two plateaus of energies. One is $582 \text{ [mJ/m}^2\text{]}$ around 9° and another is $468 \text{ [mJ/m}^2\text{]}$ around 7° . The last plateau of misorientation is in agreement with the calculated misorientation between V1-V4 pair, which is obtained in previous chapter. For small angle twist boundary, the boundary energy becomes smaller when the misorientation angle reduces. On the other hand, the deviation of misorientation angle from the angle characterized by the OR in order to reduce boundary energy should be in compensation with the simultaneous rise in strain energy due to crystallographic mismatching between austenite and martensite. Therefore, there is a limitation of deviation which was observed in previous chapter. Nevertheless, for a further study, we hope to understand the nature of the two calculated plateaus of interfacial energies around 7° and 9° by revealing atomic configuration at the boundary of the models.

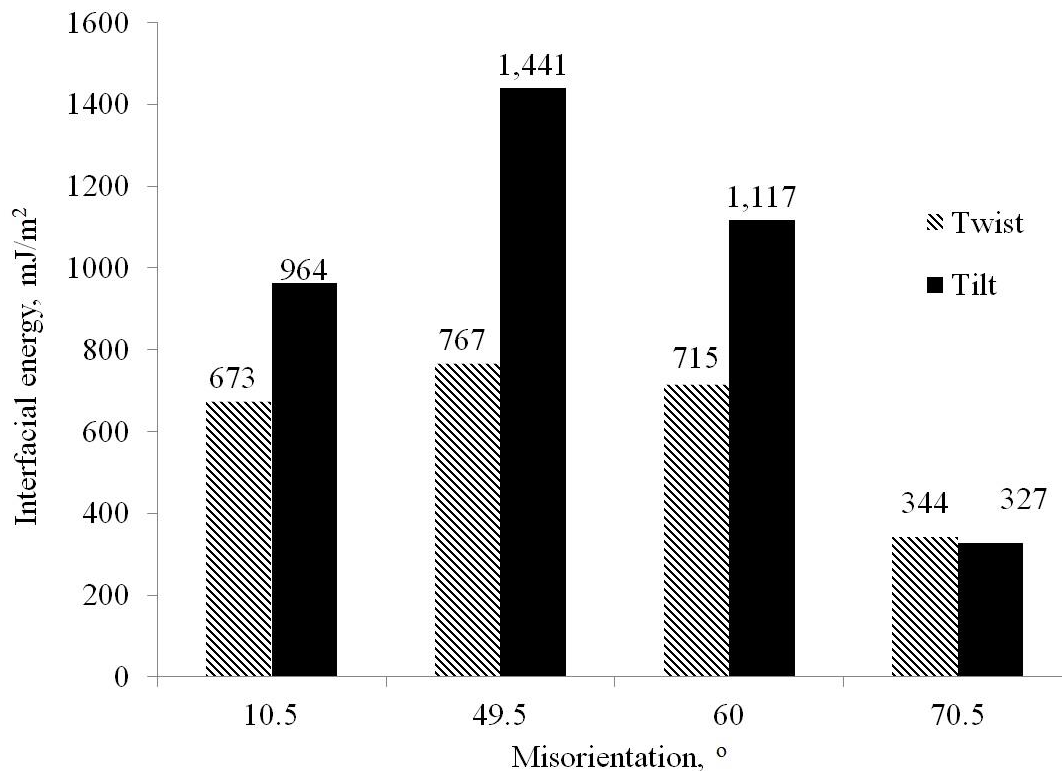


Figure 6.7. Boundary energies of boundaries between two different K-S variants.

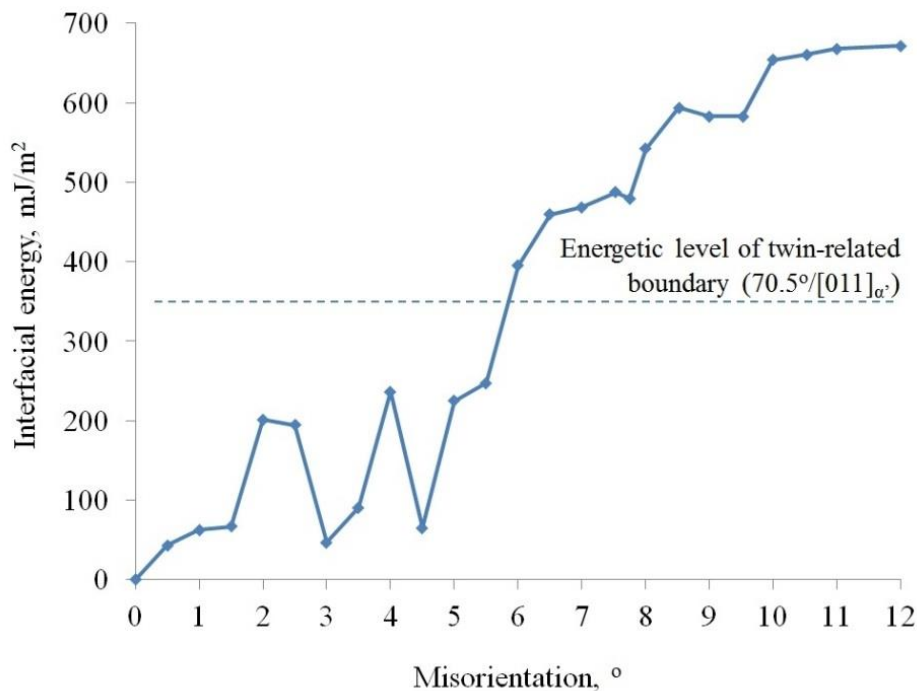


Figure 6.8. *Boundary energies of twist boundaries with small misorientation.*

The simulation result supports the measurement result of misorientation from EBSD data and they indicate that OR between martensite laths and prior austenite is close to, but not exact K-S relationship. Although deviation from OR will significantly reduce boundary energies, the boundary with misorientation of 7° still have much higher energy than boundary between twin-related variant pair. Therefore, while the block size becomes finer with additional of carbon, the block morphology is switched from interleaved type with small misorientation into single variant type with dominance of near-twin misorientation.

In case of lath boundaries (Fig.6.7), the calculated energies of twist boundary with misorientation angles varying from 0° to $5.5^\circ/[011]_{\alpha'}$ are smaller than energies of any other boundaries between two different martensite variants. Boundary energy increases gradually when misorientation is changing from 0° to $1.5^\circ/[011]_{\alpha'}$. Further changing of misorientation from $1.5^\circ/[011]_{\alpha'}$ to $5.5^\circ/[011]_{\alpha'}$ leads to an oscillation of energy with two local minima at $3^\circ/[011]_{\alpha'}$ and $4.5^\circ/[011]_{\alpha'}$. These local minima of boundary energy are probably related to small degree of local accommodations at the boundary, though further studies are required to validate this assumption. Nevertheless of the small oscillations, the calculation result is in agreement with previous TEM analysis [4-5]. When laths of a single variant group together with small alternatively changing misorientation up to $5.5^\circ/[011]_{\alpha'}$, to form a sub-block, the total boundary energy will decrease. The results also support the fact that boundary energy should play an important role in formation of lath structure included in a single sub-block.

Conclusion

Molecular dynamics simulation was employed to evaluate energetic stability of boundary between martensite laths of a single K-S variant, as well as boundary between different K-S variant pairs. The following results were obtained.

- 1) When martensite laths of the same K-S variant group together with small misorientation up to $5.5^\circ/[011]_{\alpha'}$, to form a sub-block, the obtained sub-microstructure will have smaller boundary energy than any other combination of different K-S variants. From our calculation results the morphology of sub-block can be explained by minimization of boundary energy.
- 2) In case of other boundary, which is formed between different K-S variants, the twin-related K-S variant pairs have the smallest boundary energy. This result is in good agreement with the obtained result in previous chapter, which shows that the near-twin misorientation is dominant in formation of lath martensite microstructure.
- 3) The low-angle boundary formed between two different K-S variants, such as V1-V4, V2-V5 and V3-V6, will have smaller boundary energy when the misorientation changes from $10.5^\circ/[011]_{\alpha'}$ to $6.5^\circ/[011]_{\alpha'}$. As a result, deviation from K-S orientation relationship will reduce boundary energy in this case.

Reference

- 1) D. Frenkel, B. Smit: Acad. Press. New York (2001) pp. 664.
- 2) J. M. Haile: J. Wiley, New York (1997) pp. 512.
- 3) D. C. Rapaport: Cambridge UP, Cambridge (2004) pp. 564.
- 4) S. Morito, H. Tanaka, R. Konishi, T. Furuhashi, T. Maki: Acta Mater. **51** (2003) 1789-1799.
- 5) S. Morito, X. Huang, T. Furuhashi, T. Maki, N. Hansen: Acta Mater. **54** (2006) 5323-5331.
- 6) R.A. Johnson: Phys. Rev. **145**, No.2 (1966) 423-433.
- 7) Z. Yang, R.A. Johnson: Modelling Simul. Mater. Sci. Eng. **5**, No.1 (1993) 707-716.
- 8) X.W. Zhou, H.N.G. Wadley: Comp. Mater. Sci. **39**, No.2 (2007) 340-348.
- 9) M.W. Finnis and Sinclair: Phil. Mag. A **50** (1984) 45-55.
- 10) A.P. Sutton and J.Chen: Phil. Mag. Lett. **61**, No.3 (1990) 139-146.
- 11) M. Caul, J. Fiedler, V. Randle: Scripta Mater. **35**, No.7 (1996) 831-836.
- 12) G.V. Kurdjumov and G. Sachs: Z. Physik **64** (1930) 324-326.

Chapter 7

Effect of TiC inclusions on fine morphology of lath martensite

The effect of titanium carbide (TiC) on morphology of low-carbon steel martensite was studied by means of electron backscatter diffraction (EBSD). The nucleation and growth of new morphology subunits such as packet, block and sub-block are observed in the area surrounding of micron-sized TiC particles. The local misorientation of austenite near TiC particle from grain orientation is larger than the average value with a localized characteristic. The position of new morphology subunits has a well correspondence with the area in vicinity of TiC particle, where austenite has large misorientation. The presence of micron-sized TiC particle in austenite during martensitic transformation causes local raise of strain which suppresses growth of one martensite variant while stimulates nucleation and growth of another one.

7.1. Introduction

As mentioned in chapter 1, by employing double shear version of phenomenological theory some researchers have pointed out that, the transformation strain can be well accommodated by activation of all six martensite variants within a packet [1-4]. The condition required for such case of self-accommodation is the equal fractions of all six martensite variants. However, many attempts on quantitative calculation of martensite variants' fraction have not confirmed such condition. The fractions of martensite variants are varied with the deformation state of austenite as well as the transformation conditions or chemical composition [5-22]. Thus the presence of all six martensite variants may partially accommodate transformation strain, but the unequal fractions of those variants imply that the transformation strain should exhibit a local characteristic.

In thermal induced transformation of austenite into lath martensite, the first nucleation happens near the prior austenite boundary and grows into the grain [23-26]. The transformation strain due to the nucleation of martensite is large [2-3, 27-29] and it could not be fully compensated by self-accommodation as discussed above. The remained strain will transfer into the untransformed region of austenite causing a local rise of strain in that area. In principle, the high local strain field in untransformed austenite regions can suppress growth of the growing toward martensite variant and stimulate the nucleation and growth of another variant which is more favorable for self-accommodation. A direct evidence of this phenomenon has not been reported elsewhere.

In this study, we have an idea of using the micron-sized inclusions particles in austenite matrix for study this phenomenon. The presence of non-metallic inclusions like oxides or carbides which have superior hardness compared with austenite matrix will impede the strain accommodation in their surrounding austenite. Hence it is expected that the local strain in such austenite regions will raise up to a high level, so the effect of local strain on nucleation and grow of fine martensite variant may be possibly observed. The titanium carbide (TiC) is chosen for the particular purpose, because this carbide has sufficient solubility in austenite at moderate temperature (1400-1600K) which allows control on the size of inclusions particle by heat treatment. The

calculation of steel's composition and heat treatment will be described in more details in the next section.

In chapter 3, we have introduced a new kind of austenite misorientation map, which is received from analysis of EBSD data of martensite inherited from one austenite grain by our present method. This map corresponds to the misorientation of local austenite orientation from average grain orientation. It should be noted that the total transformation strain could not be mapped by this way, but only the strain which was accommodated in austenite. Since the strain transferred to austenite cause misorientation from average grain orientation, the austenite misorientation map will be used for characterization of local strain caused by martensitic transformation in austenite grain.

This study includes preparing of TiC included steel and choosing of heat treatment route for precipitation of micron-sized TiC in austenite matrix. The high resolution EBSD measurement of martensite orientation will be performed for final microstructure of the material. The local strain of austenite with TiC inclusions will be characterized by austenite misorientation map. Our method will be used for analysis of EBSD data, characterization of martensite morphology and austenite misorientation map.

7.2. Experimental

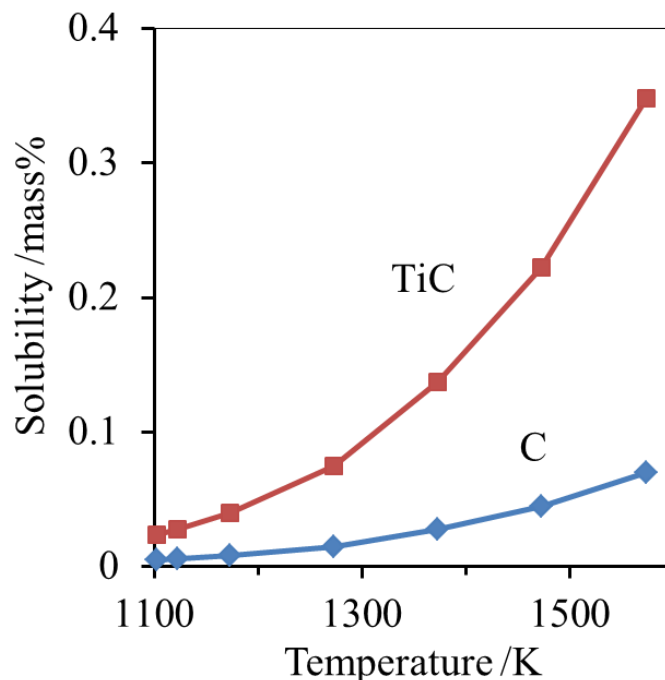


Figure 7.1. Solubility in austenite of TiC (square) and C (rhomb).

TiC included steel named Ti10 with chemical composition of Fe-0.23 mass%C-2.92 mass%Mn-1.0 mass%Ti was prepared for present investigation. The Ti10 steel has a near stoichiometric composition of TiC ($Ti/C = 3.986$) with slightly excessive amount of Ti. The amount of dissolved TiC and of solution carbon (in mass%) in austenite of

the Ti10 steel in equilibrium condition at temperature range 1103K-1623K was calculated by Thermo-Calc software with TCFE5 database. The analyzed result expressing the dependent of solubility of TiC and C in austenite upon heating temperature is shown in Fig.7.1. Based on this graph, the corresponding solubility (in mass%) can be approximately expressed through the temperature T (in Kelvin) by the following equations:

$$\ln(\rho_{\text{TiC}}) = 7.471 \ln(T) - 56.031 \quad (7.1).$$

$$\ln(\rho_{\text{C}}) = 7.471 \ln(T) - 57.637 \quad (7.2).$$

where ρ_{TiC} and ρ_{C} are the solubility of TiC and C in austenite respectively.

For the chosen austenitizing temperature of 1573K, the amount of TiC and Carbon dissolved in austenite of Ti10 steel calculated from Eq.(7.1) and Eq.(7.2) are 0.348 and 0.070 (mass%), respectively. Therefore, the steel C10 without TiC was chosen as a reference with C concentration which is closed to the equilibrium concentration of C in the Ti10 steel at 1573K.

Since the C10 steel is a pure low carbon steel, it was impossible to receive full lath martensite microstructure of this steel through conventional heat treatment route. For this reason, a rapid quenching treatment was applied for this steel in order to receive full lath martensite microstructure. The heat treatment of C10 steel is as follows. The steel in form of a cold-rolled 1.5mm thin strip was heated with the rate of 10K/s to 1373K with holding for 150s and followed by a rapid quenching under high pressure water-jet. By this heat treatment it was successful to obtain a microstructure of full lath martensite with fine prior austenite grain size.

The Ti10 steel in form of a hot rolled bar was homogenized at 1573K for 86ks in tube vacuum furnace. The heating temperature was chosen as the highest allowable temperature of the furnace in order to maximize the solubility of TiC in the austenite. The steel was then slowly cooled down to 973K in Ar gas flow, kept at this temperature for 7.2ks. The slow cool and holding at low temperature was applied to allow fine precipitation of TiC inclusions in austenite due to reduction of its solubility. The steel is finally cooled in water for completion of martensitic transformation. After this heat treatment, the microstructure of Ti10 steel is full lath martensite with high density of micron-sized TiC particle distributed in prior austenite grain and at grain boundaries (Fig.7.2).

The samples were cut from the steels, mechanically polished and etched with 3% Nital for optical microscopic observation. The average size of prior austenite grains was measured using linear interception method. EBSD samples of C10 were prepared by the same mechanical polishing procedure as for optical microscopic samples. Only the samples of Ti10 steel with high density of micron-sized TiC particles, two steps of ion polishing using Ar gas were added to obtain better flatness of the surface. The detailed description of ion polishing was given in chapter 2.

The EBSD experiments were carried out on JEOL JSM7001FA field emission gun scanning electron microscope equipped with TSL EBSD data collection system. The scans for samples of C10 steel were conducted at accelerating voltage of 25kV with scan step of 200nm at x1000 magnification. To observe the change of morphology in fine scale, high resolution scans were performed at 15kV of accelerating voltage with step of 40nm for samples from TiC steel at a magnification of x10,000.

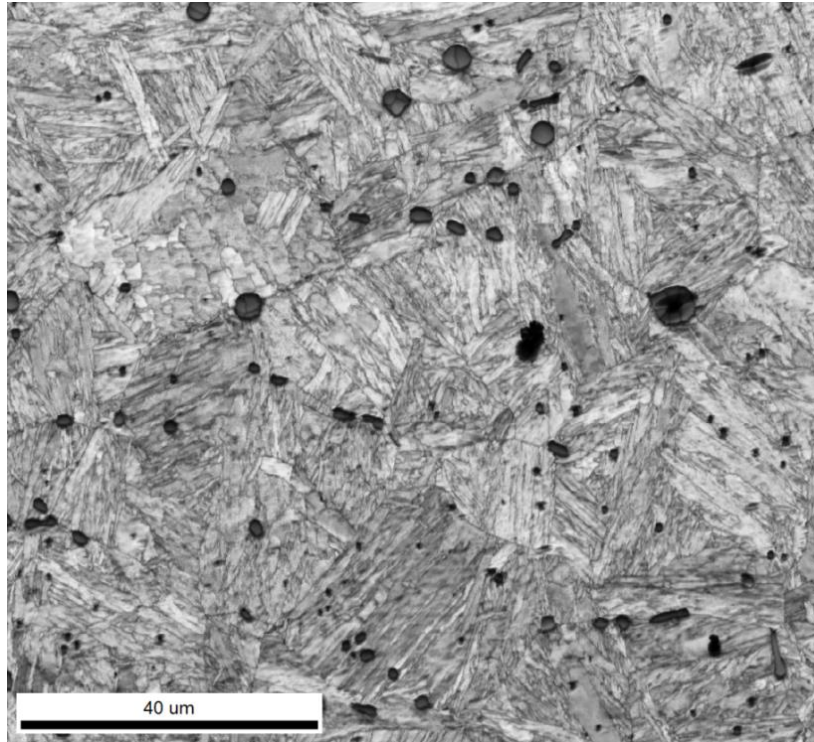


Figure 7.2. *The microstructure of Ti10 steel after heat treatment - the micron-sized TiC particles with low contrast are in dark color.*

The EBSD data were analyzed by using our present computational method. For EBSD data of each sample, the analytical procedure includes: fitting the austenite orientation and OR, plotting the austenite misorientation map, close-packed plane (CP) and martensite variant maps.

7.3. Result and discussion

C10 steel has a relatively homogeneous microstructure of lath martensite with average prior austenite grain size of 86 μm . Although Ti10 steel was annealed at high temperature for relatively long time, the average size of prior austenite grains is 46 μm . Its microstructure is inhomogeneous with high density of micron-sized TiC particles, which locate at prior austenite grain boundaries and inside martensite packets.

Figure 7.3a shows the distribution of austenite misorientation for one prior austenite grain of C10 steel. This austenite misorientation map represents the misorientation of local austenite orientation from average value of the grain. As mentioned in chapter 3, if we assume a constant OR over the prior austenite grain, the austenite misorientation is equal to the misorientation of experimental martensite orientation from the

corresponding orientation calculated from the OR. For C10 steel the fitted OR can be expressed as $(111)_\gamma : 1.26^\circ$ from $(011)_{\alpha'}$ and $[\bar{1}01]_\gamma : 2.62^\circ$ from $[\bar{1}\bar{1}1]_{\alpha'}$. The mean misorientation of austenite local orientations from average grain orientation is 1.57° . The misorientation distribution has a localized characteristic with some local areas which have misorientation significantly higher than the mean value.

The (001) pole figures of experimental data and fitted OR (open red circles) were superimposed in Fig.7.3b showing a good match between them. It shows that most of the experimental points (76%) have misorientation from calculated orientations smaller than 2° . If we assume that the austenite local misorientation was caused by the deformation of austenite due to transformation strain, the distribution of misorientation in Fig.7.3a implies that the transformation strain in C10 steel was well accommodated in the whole prior austenite grain.

The close-packed plane map, which represents 4 types of martensite packets as group of martensite variants sharing the same close-packed plane relationship with austenite, is plotted in Fig.7.4a. The areas with misorientation larger than 4° in Fig.7.3a, are mainly found at packet boundaries in Fig.7.4a. When the martensite variants of the same close-packed plane relationship with austenite form together (Fig.7.4b), the transformation strain is well accommodated. Because of this reason, the CP map of C10 low carbon steel shows coarse packet morphology (Fig.7.4).

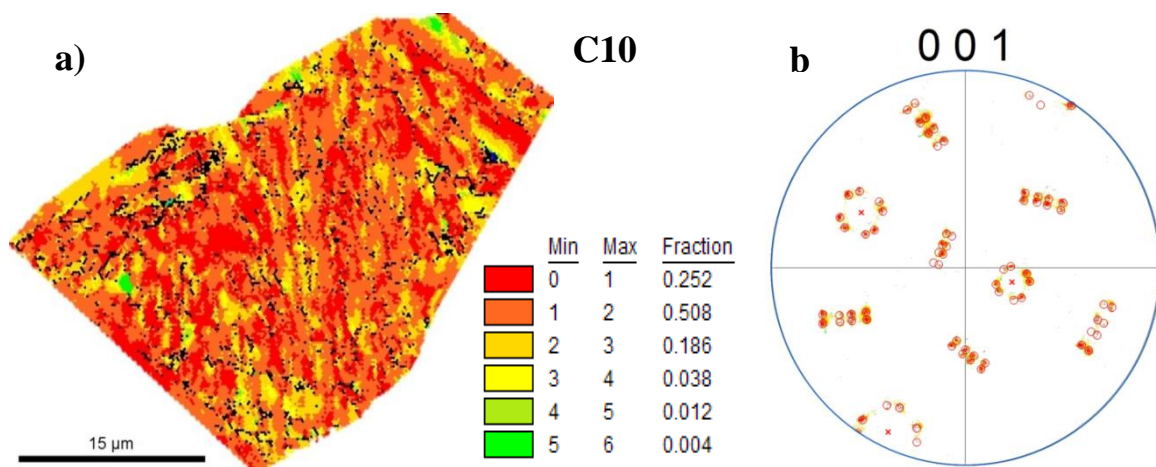


Figure 7.3. *a* – Distribution of austenite misorientation with intervals of 1° (scanned points with confidence index (CI) < 0.1 were colored in black); *b* – The (001) pole figure of experimental points colored by the same color codes in (a), the open circles express fitted OR and the red saltire marks are {001} poles of austenite fitted orientation.

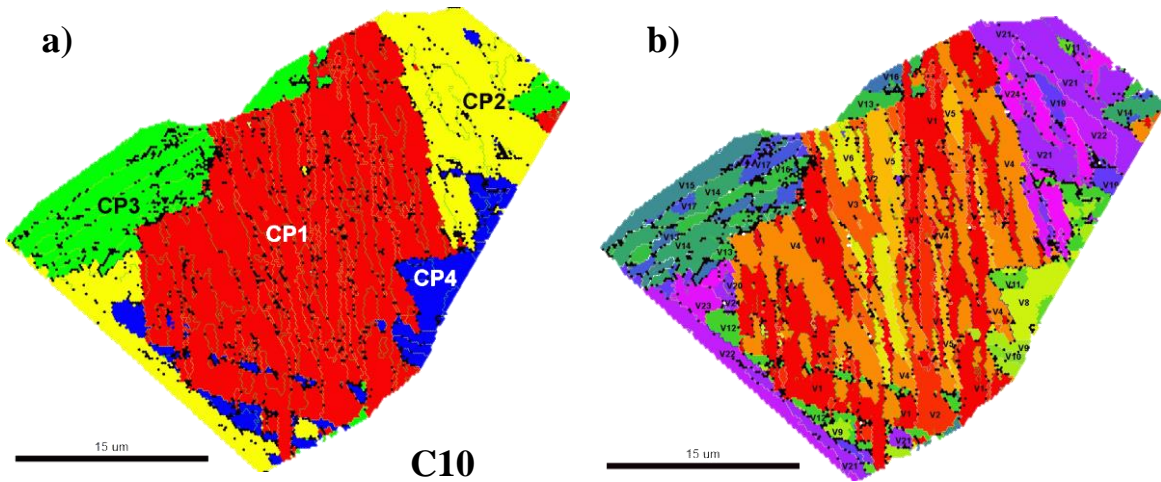


Figure 7.4. *a* – CP map showing 4 types of CP variants which were colored in red, yellow and blue; *b* – Variant map showing 24 variants of martensite with rainbow color code including magenta.

For Ti10 steel, the same distribution of misorientation and pole figures were plotted in Fig.7.5. The fitted OR of Ti10 steel is $(111)_{\gamma} : 1.30^{\circ}$ from $(011)_{\alpha}$, and $[\bar{1}01]_{\gamma} : 2.71^{\circ}$ from $[\bar{1}\bar{1}1]_{\alpha}$. This OR is very close to the OR obtained from C10 steel. However, the mean misorientation of austenite local orientations from average grain orientation in Ti10 steel is 2.33° , which is significantly higher than that of C10 steel. Moreover, the areas with large misorientation ($>4^{\circ}$) are located near TiC particles which are labeled by capital letters from A to I (see Fig.7.5a). It is interesting that the austenite misorientation map also gives information about the nucleation and growth of a particular martensite variant. On one side, the variant V6 indicated by black arrows in Fig.7.6b, judging by the distribution of misorientation (Fig.7.5a) and its shape (Fig.7.6b), was nucleated at prior austenite grain boundary between TiC particles (A) and (B), grew into the grain, became a sharp tip when passing the particle (H) and continued growing until reaching the particle (I). The local misorientation at the tip of V6 gradually increased before its growth was suppressed by the particle (I).

On another side, the variant V17 of CP3 indicated by white arrows (in Fig.7.5a and Fig.7.6b) was nucleated at the particle (I) and grew into variant V19 of CP4 with misorientation higher than misorientation of its surrounding. The same situations are observed when variant 10 of CP2 appeared at particle (D) as well as between particles (F) and (G). Variant 16 of CP3 was found at the particle (F) while variant 17 and 18 of the same CP3 were seen at the edge of particle (G). Those variants are small in size with large misorientation from average grain orientation.

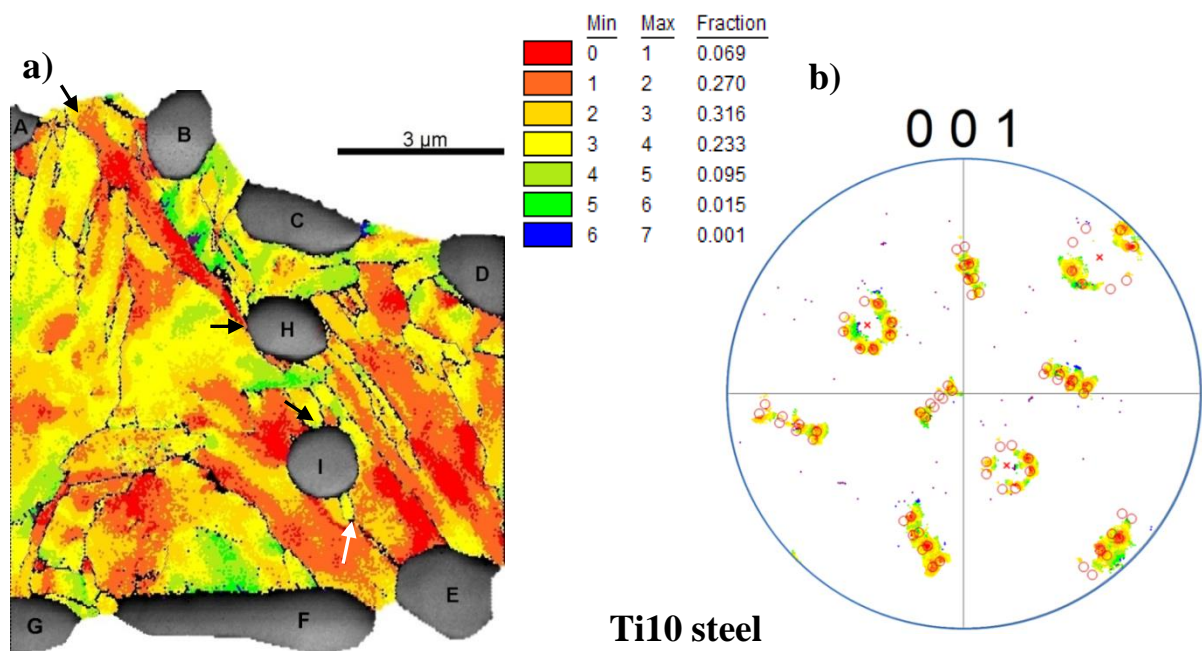


Figure 7.5. *a* – Distribution of austenite misorientation with intervals of 1° (scanned points with $CI < 0.1$ were colored in black); *b* – The (001) pole figure of experimental points colored by the same color codes in *(a)*, the open circles express fitted OR and the red saltire marks are $\{001\}$ poles of austenite fitted orientation.

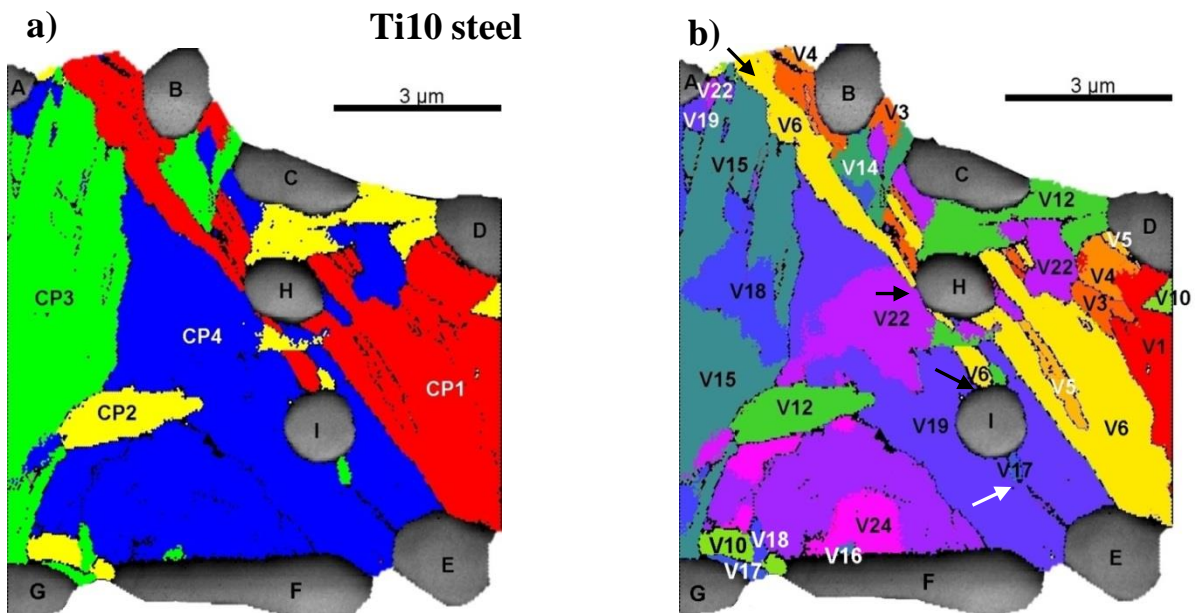


Figure 7.6. *a* – CP map showing 4 types of CP variants which were colored in red, yellow, green and blue; *b* – Variant map showing 24 variants of martensite with rainbow color code from red to magenta.

The size of martensite variants which are nucleated near or at the TiC particle is comparable with the particle size. It shows that during transformation the austenite areas near TiC particle which has a superior hardness than hardness of austenite are difficult to accommodate the transformation strain. As a result the local strain of austenite near TiC increases to a high level, which can retard the growth of growing variants causing large misorientation from average value. Presence of high local strain in austenite surrounding the TiC particle can also stimulate nucleation of a new martensite variant of other CP variants in order to accommodate the local strain.

7.4. Conclusion

In this chapter a new approach for study the effect of austenite local strain on formation of martensite was proposed. The model steel with excessive amount of TiC inclusions was successfully used for this purpose. The newly developed method for EBSD analysis was used for characterization of austenite misorientation and morphology of martensite. The following results are obtained:

1. The transformation strain is well accommodated in C10 low carbon steel. The martensite variants of the same CP relationship have tendency to group together forming coarse packet morphology in this steel. Nevertheless, the austenite misorientation map has a local characteristic with local raise of misorientation near packet boundary.

2. There is a local increase of austenite misorientation observed near TiC particle which should have relationship with rising local strain in austenite due to the difficulty of strain accommodation in the austenite areas surrounding the TiC particle during martensitic transformation.

3. Micron-sized TiC particle presented in austenite can retard or completely suppress the growth of martensitic variant which is growing toward that particle. The high local strain field around TiC particle can also stimulate nucleation of a new martensite variant which can grow to a size comparable with the particle's size.

4. The high local strain in austenite can be partially accommodated by nucleation of new martensite variant of other CP relationship. To activate such nucleation of new martensite variant, it requires that local strain in austenite should be larger than a critical value.

Reference

- 1) Z. Guo, C.S. Lee, J.W. Morris Jr.: *Acta Mater.* **52** (2004) 5511-5518.
- 2) S. Morito, H. Tanaka, R. Konishi, T. Furuhashi, T. Maki: *Acta Mater.* **51** (2003) 1789-1799.
- 3) S. Morito, X. Huang, T. Furuhashi, T. Maki, N. Hansen: *Acta Mater.* **54** (2006) 5323-5331.
- 4) J. W. Morris, Jr., C. S. Lee and Z. Guo: *ISIJ Int.* **43** (2003) 410-419.
- 5) F. Barcelo, Y. Carlan, J.L. Béchade, B. Fournier: *Phase Trans.* **82** (2009) 808-820
- 6) A.K. Das, T. Ohba, S. Morito, M. Yaso: *Mater. Sci. Forum* **654-656** (2010) 138-141.
- 7) T. Furuhashi, K. Kikumoto, H. Saito, T. Sekine, T. Ogawa, S. Morito, T. Maki: *ISIJ Int.* **48** (2008) 1038–1045.
- 8) T. Furuhashi, H. Kawata, S. Morito, G. Miyamoto, T. Maki: *Metall. Mater. Trans. A* **39**, No.5 (2008) 1003-1013.
- 9) P. Haušild, V. Davydov, J. Drahokoupil, M. Landa, P. Pilvin: *Mater. Design* **31**, No.4 (2010) 1821-1827.
- 10) B. Hutchinson, J. Hagström, O. Karlsson, D. Lindell, M. Tornberg, F. Lindberg, M. Thuvander: *Acta Mater.* **59** (2011) 5845-5858.
- 11) H. Kitahara, R. Ueji, M. Ueda, N. Tsuji, Y. Minamino: *Mater. Charac.* **54** (2005) 378– 386.
- 12) G. Krauss, A. R. Marder: *Metall. Trans.* **2**, No.9 (1971) 2343-2357.
- 13) G. Krauss: *Mater. Sci. Eng. A* **273–275** (1999) 40–57.
- 14) C.P. Luo, J. Liu: *Mater. Sci. Eng. A* **438–440** (2006) 149-152.
- 15) T. Chiba, G. Miyamoto, T. Furuhashi: *ISIJ Int.* **53** (2013) 915-919.
- 16) S. Morito, H. Saito, T. Ogawa, T. Furuhashi, T. Maki: *ISIJ Int.* **45** (2005) 91-94.
- 17) S. Morito, Y. Adachi, T. Ohba: *Mater. Trans.* **50**, No.8 (2009) 1919-1923.
- 18) S. Morito, R. Igarashi, K. Kamiya, T. Ohba, T. Maki: *Mater. Sci. Forum* **638 - 642** (2010) 1459-1463.
- 19) V. Ocelík, I. Furár and J.Th.M. De Hosson: *Acta Mater.* **58** (2010) 6763-6772.
- 20) B. Sonderegger, S. Mitsche, H. Cerjak: *Mater. Charac.* **58** (2007) 874–882.
- 21) A. Stormvinter, G. Miyamoto, T. Furuhashi, P. Hedström, A. Borgenstam: *Acta Mater.* **60**, No.20 (2012) 7265-7274.
- 22) N. Takayama, G. Miyamoto, T. Furuhashi: *Acta Mater.* **60** (2012) 2387-2396.
- 23) A. Borgenstam: *Mater. Sci. Eng. A* **273–275** (1999) 425–429.

- 24) M. Cohen: Mater. Trans. **33**, No.3 (1992) 178-183.
- 25) S. Morito, Y. Edamatsu, K. Ichinotani, T. Ohba, T. Hayashi, Y. Adachi, T. Furuhashi, G. Miyamoto and N. Takayama: Alloys Compd. **577S** (2013) 587-592.
- 26) S. Zhang, S. Morito and Y. Komizo: ISIJ Int. **52** (2012) 510-515.
- 27) H.K.D.H. Bhadeshia, R. Honeycombe: Elsevier (2006) pp. 360.
- 28) P.M. Kelly: Mater. Sci. Eng.A **438-440** (2006) 43-47.
- 29) A. Yamanaka, T. Takaki, Y. Tomita: Mat. Sci. Eng.A **491**, No.1-2 (2008) 378-384.

Chapter 8

Conclusion

This study aimed to expand current knowledge of microstructure formation in martensitic steel with an extended view point from prior austenite microstructure to fine morphology of lath martensite. A new approach to understanding the microstructure formation in martensitic steel, which considers the relation between martensite morphology, orientation relationship and chemical composition is applied. The following results were obtained:

I. Development of advanced computational method for EBSD data analysis

(1) An advanced computational method for crystallographic and morphological analyses of martensite using EBSD data was developed. The method is designated for fast and precise calculation of austenite orientation and γ/α' orientation relationship (OR). This method provides advantages for automatic indexing of martensite variants, visual plotting of martensite morphology, reconstruction of prior-austenite local strain and prior-austenite microstructure. The method extends application of EBSD technique for sophisticated crystallographic study, not only on martensite but also on prior-austenite microstructure.

II. Formation of austenite microstructure

The concept of “prior-austenite microstructure” was proposed. A new method for precise reconstruction of austenite microstructure from EBSD data of martensite was developed. The method was applied successfully for reconstruction of austenite microstructure in several high carbon steels. A specific morphology of twin-related neighbor grains in prior-austenite microstructure of high carbon steels was firstly observed and characterized. Several conclusions on the formation of prior-austenite microstructure in high carbon steels are obtained as follows:

(2) In case of reversion of austenite (A) from full pearlitic microstructure, there are two essential conditions for the formation of twin-related austenite grains from pearlitic ferrite (PF). That is:

- The nucleation of austenite should be occurs at different locations within one PF grain. The favorable nucleation site is triple junction between PF grains.
- The existence of a twin selection rule, which implies that within a single PF grain, the nuclei of reserved austenite should choose either the orientation bearing an OR with PF or a twin of that orientation (Fig.8.1)

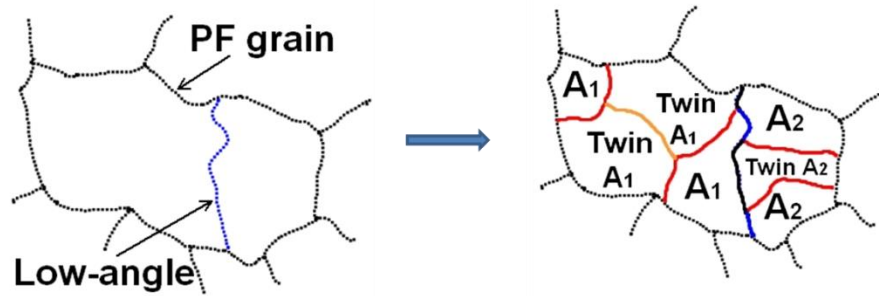


Figure 8.1. Schematic illustration of twin related austenite grains by reversion from full pearlitic microstructure.

(3) In case of reversion of austenite (A) from a mixture of P+F. With presence of F, two additional nucleation modes of reversed austenite are observed:

- The reversed A nucleates at F boundary with whom it bears an OR;
- The A nucleates at F boundary which is in OR with a twin of that austenite orientation.

The presence of F in P+F steels provides additional nucleation sites for A formation, while the twin selection rule is general for reversed austenite nuclei irrespective of their nucleation sites (Fig. 8.2)

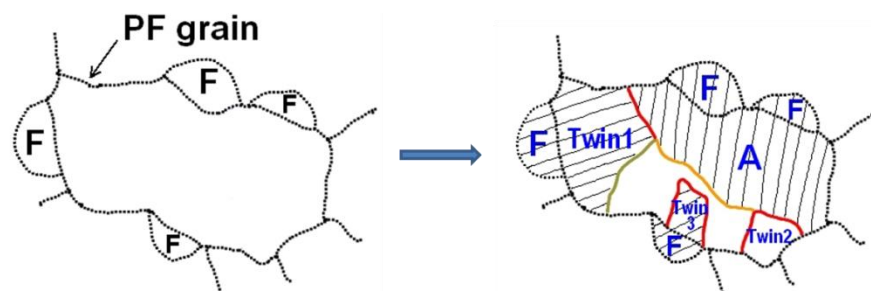


Figure 8.2. Schematic illustration of twin related austenite grains by reversion from a P+F microstructure.

(4) It is likely that the mechanism of austenite microstructure formation in the Japanese sword is similar to that of ordinary steel, which is controlled by the reverse transformation of austenite from P or P+F. The effects of traditional sword making method on austenite microstructure of carbon steel are visible as finer average grain size and the presence of small areas with non-indexed austenite orientations.

III. Formation of fine martensite morphology

A new approach for study the effect of austenite local strain on formation of fine martensite morphology was proposed. The model steel with excessive amount of micron-sized TiC inclusions was successfully used for this purpose. The newly developed method for EBSD analysis was used for characterization of austenite misorientation and morphology of martensite. The following results are obtained:

(5) The transformation strain is well accommodated in C10 low carbon steel. The martensite variants of the same close-packed plane relationship have tendency to group together forming coarse packet morphology in this steel. Nevertheless, the austenite misorientation map has a local characteristic with local raise of misorientation near packet boundaries.

(6) There is a local increase of austenite misorientation observed near TiC particle which should have relationship with rising local strain in austenite due to the difficulty of strain accommodation in the austenite areas surrounding the TiC particle during martensitic transformation.

(7) Micron-sized TiC particle presented in austenite can retard or completely suppress the growth of martensitic variant which is growing toward that particle. The high local strain field around TiC particle can also stimulate nucleation of a new martensite variant which can grow to a size comparable with the particle's size.

(8) The high local strain in austenite can be partially accommodated by nucleation of new martensite variant of other close-packed plane relationship. To activate such nucleation of new martensite variant, it requires that local strain in austenite should be larger than a critical value.

IV. Molecular dynamics calculation of boundary energy in lath martensite

Molecular dynamics simulation was employed for calculation of boundary energy between martensite laths of a single K-S variant, as well as boundary between different K-S variant pairs. The following results were obtained:

(9) When martensite laths of the same K-S variant group together with small misorientation up to $5.5^\circ/[011]_{\alpha'}$ to form a sub-block, the obtained sub-microstructure will have smaller boundary energy than any other combination of different K-S variants. From our calculation results the morphology of sub-block can be explained by minimization of boundary energy.

(10) In case of other boundary, which is formed between different K-S variants, the twin-related K-S variant pairs have the smallest boundary energy. This result is in good agreement with the obtained result in previous chapter, which shows that the near-twin misorientation is dominant in formation of lath martensite microstructure.

(11) The low-angle boundary formed between two different K-S variants, such as V1-V4, V2-V5 and V3-V6, will have smaller boundary energy when the misorientation changes from $10.5^\circ/[011]_{\alpha'}$ to $6.5^\circ/[011]_{\alpha'}$. As a result, deviation from K-S orientation relationship will reduce boundary energy in this case.

V. The effect of chemical composition on OR and morphology of martensite

The OR can be calculated from EBSD data of martensite with error 0.5° . The OR is characterized by small deviation θ_1 between close-packed planes and θ_2 between close packed directions of the two phases. The effect of chemical composition on OR

and morphology of martensite was investigated. The results are as follows:

(12) Increase of C as interstitial impurity in martensite lattice from 0.1 to 0.86 mass% causes mainly decrease of the deviation between closed-packed directions θ_2 . The reason may be the presence of tetragonality of martensite lattice when C is added. The change of OR also causes change of block morphology, which is switched from interleaved type in C10 steel to single variant type in steels with carbon content larger than 0.4 mass%.

(13) The deduction of θ_2 with increase of C in range of 0.4-0.86 mass% is linear. Using this relation, the carbon content of a Japanese sword with unknown composition can be estimated to be 0.65 mass%, which is in reported range of the other studied swords.

(14) The substitutional elements such as Mn or Ni, which cause expansion of martensite lattice, are responsible for increase of deviation between close-packed planes θ_1 , and Mn shows a slightly stronger effect than Ni for the same content of solute.

(15) The misorientations between specific martensite variants, which share the same plane parallel relationship with austenite, are also sensitive to the change of composition. Addition of C from 0.1 to 0.86mass% causes disappearance of low-angle misorientation peaks, which is the evident of change in block morphology. The increase of C content also causes increase of near-twin misorientation of V1-V2 pair toward exact twin relationship. Moreover, the measured misorientations are significantly larger than calculated values. It is likely that the boundary structure between those martensite variant is adjusted toward exact twin boundary in order to reduce the boundary energy. The molecular dynamics calculation of boundary energy also supports this observation. The addition of Mn or Ni up to 3 mass% causes decline of the small-angle peak compared with C10 carbon steel. However, the effect of those elements on block morphology is weaker than that of C, since the small-angle misorientation peak clearly remains in the steels with 3 mass% of Mn or Ni.

Acknowledgment

My first thoughts of gratitude go to my supervisor, Prof. T. Ohba, for his continuous supports, invaluable suggestions and fruitful discussions throughout my doctoral course. I also wish to express my sincere thanks to his wife, Mrs. Masako Ohba, who has become a great friend of my family. Without her endless helps and friendship, the stay of my family in Japan would not be such an enjoyable and memorable time.

I am indebted to Prof. S. Morito, who with great patience has taught me all the experimental techniques used in this study, for sharing his knowledge, fruitful discussions and for warm hospitality throughout my stay at Ohba-Morito laboratory.

I am grateful to Dr. T. Hayashi for many valuable suggestions and constructive comments.

I wish to express my sincere gratitude to Prof. T. Furuhashi and Prof. G. Miyamoto at IMR, Tohoku University for the Thermo-Calc calculation, useful discussions and for their warm hospitality during my EBSD serial sectioning experiment at their laboratory.

I would like to express many thanks to Prof. H. Terasaki at Osaka University for kindly sharing his calculation results and many open-minded discussions.

I am deeply obliged to Mr. R. Tamura and Mr. Y. Maegawa for their helps during the initial first year of my staying in Japan, for their friendship and their assistance.

I would like to thank Ms. C. Matsumoto for sharing the EBSD data of high carbon steels and Japanese swords, Mr. H. Taichi for sharing the EBSD data of low alloy steels.

Special thanks are due to Mr. Y. Shimabayashi for his assistance during serial sectioning experiment at Tohoku University and Mr. N. Moriguchi for a memorable trip to Hawaii during PRICM8.

I am grateful to Hitachi Metals (Yasugi work) for providing the Ti10 steel with phase diagram and Sumitomo Metal (currently Nippon steel & Sumitomo metal) for providing the series of low alloy steels.

I thankfully acknowledge the scholarship for my doctoral course from Ministry of Education, Culture, Sports, Science and Technology (MEXT). I also appreciate the support of Inter-University Cooperative Research Program of IMR, Tohoku University (Proposal No. 12K0063).

I am indebted to all the teachers of Japanese classes, who have kindly taught me many things about the language and Japanese culture. I would like specially mention the helps and supports from Vietnamese community at Shimane University, whose wonderful friendship is gratefully appreciated.

Last but not least, I am eternally grateful to my lovely family for all their love, support and understanding.